



Grant Agreement:	247223
Project Title:	Advanced Radio InTerface Technologies for 4G SysTems ARTIST4G
Document Type:	Deliverable

Document Identifier:	
Document Title:	<b>D6.3 - Laboratory and field trial results connected to the second set of innovations</b>
Source Activity:	WP6
Editors:	Michael Grieger and Johannes Koppenborg
Authors:	See table page 4
Status / Version:	final
Date Last changes:	27.06.2012
File Name:	D6p3_final.doc

Abstract:	This deliverable provides a final summary on field trial results in ARTIST4G that complement theoretical and simulation studies done in other work packages.
-----------	--

Keywords:	LTE, LTE advanced, CoMP, 2D and 3D Beamforming, channel estimation, double Alamouti, interference cancellation receivers, SIC, moving relays, intra-site CoMP, field trials, lab trials
-----------	---

## Table of Contents

<b>Table of Contents .....</b>	<b>1</b>
<b>Authors.....</b>	<b>4</b>
<b>1 Executive Summary .....</b>	<b>5</b>
<b>2 Introduction .....</b>	<b>6</b>
<b>3 Lab and Field Trial Results.....</b>	<b>7</b>
3.1 Advanced 3D-Beamforming.....	7
3.1.1 Introduction.....	7
3.1.2 3D Beamforming Trials.....	7
3.1.2.1 Description of Measurement Setup .....	7
3.1.2.2 Lab Trials with 3D Beamforming .....	8
3.1.2.3 Field Trials with 3D Beamforming.....	9
3.1.3 Conclusion.....	12
3.2 Field Trial Evaluation of UE Specific Antenna Downtilt in an LTE Downlink.....	12
3.2.1 Introduction.....	12
3.2.2 Field Trial Setup .....	13
3.2.3 Modeling the Impact of Antenna Downtilts.....	14
3.2.4 Results.....	14
3.3 Downlink CoMP without CSI Feedback.....	14
3.3.1 Introduction.....	14
3.3.2 Description of interference and cooperation scenarios.....	15
3.3.3 Testbed implementation on hardware platform.....	16
3.3.3.1 Step 1: test of 4x2 (double Alamouti) downlink receiver .....	17
3.3.3.1 Step 2: test of 2x2 downlink.....	17
3.3.3.2 Step 3: Test of virtual double Alamouti.....	18
3.3.4 Performance assessment – from simulation results to laboratory measurements	21
3.3.4.1 Simulation description.....	21
3.3.4.1 Methodology .....	22
3.3.4.1 Simulation results .....	22
3.3.4.1 Laboratory measurements.....	23
3.3.5 Possible System On Chip architecture evolution for next generation LTE-A.....	24
3.3.6 Conclusion.....	28
3.4 Uplink CoMP .....	29
3.4.1 LTE-Advanced Testbed.....	29
3.4.2 Base Station Signal Processing .....	31
3.4.3 Comparison of Intra and Inter Site CoMP .....	32
3.4.3.1 Introduction .....	32
3.4.3.2 Receive Signal Processing.....	32
3.4.3.3 Field Trial Results .....	32
3.4.4 Field Trial vs. Simulation .....	36
3.4.5 Uplink CoMP for Moving Relays .....	38
3.4.5.1 Measurement Setup .....	39
3.4.5.2 Receiver Signal Processing.....	40
3.4.5.3 Results .....	41
3.5 Advanced Relays .....	46
3.5.1 CoMP on the Fixed Feeder Link .....	46

3.5.2 Using Predictor Antennas for Moving Relays.....	46
3.5.2.1 Measurement Setup .....	46
3.6 Downlink CoMP .....	48
3.6.1 Validation of Tortoise Concept .....	48
3.7 Performance Assessment of MIMO Receivers in LTE Systems .....	52
3.7.1 Introduction.....	52
3.7.2 Review of the MIMO receivers .....	52
3.7.2.1 Simple Equalizers .....	52
3.7.2.2 IC Equalizers .....	53
3.7.2.3 Complexity .....	54
3.7.3 Simulation Results.....	55
3.7.4 Conclusions.....	60
<b>Conclusions.....</b>	<b>61</b>
<b>4 References.....</b>	<b>62</b>
<b>5 Appendix.....</b>	<b>64</b>
5.1 Testbed Information.....	64
<b>6 Abbreviation .....</b>	<b>67</b>

## Authors

Name	Beneficiary	E-mail address
Johannes Koppenborg	ALUD	johannes.koppenborg@alcatel-lucent.com
Cornelis Hoek	ALUD	cornelis.hoek@alcatel-lucent.com
Michael Grieger	TUD	michael.grieger@inf.et.tu-dresden.de
Fabian Diehm	TUD	fabian.diehm@ifn.et.tu-dresden.de
Vincent Kotsch	TUD	vincent.kotsch@ifn.et.tu-dresden.de
Denis Dutoit	CEA	denis.dutoit@cea.fr
Dimitri Kténas	CEA	dimitri.ktenas@cea.fr
Yang Liu	SEQ	yliu@sequans.com
Serdar Sezginer	SEQ	serdar@sequans.com
Mikael Sternad	UU/CTH	mikael.sternad@signal.uu.se
Tommy Svensson	CTH	tommy.svensson@chalmers.se
Wolfgang Zirwas	NSN	wolfgang.zirwas@nsn.com

## 1 Executive Summary

After having presented a first set of field trial and demonstrator results in D6.2, this deliverable summarizes the second set of field trial results of ARTIST4G. The trial and demo results span a wide range of topics that range from 3D beamforming, uplink/downlink CoMP, to channel prediction for moving relays and the implementation of interference cancellation receivers. The results in this deliverable complement the theoretical and simulation based studies in other work packages which verifies and demonstrates the innovative concepts of ARTIST4G.

## 2 Introduction

The project ARTIST4G has the objective to improve the ubiquitous user experience of cellular mobile radio communication systems by focusing on the following requirements: high spectral efficiency and user data rate across the whole coverage area, fairness between users, low cost per information bit, and low latency. At the end of the project lifetime, we have seen a series of high quality deliverables and papers that show innovative concepts and by benchmarking them with the state-of-the-art to fulfill the above requirements following one of the concepts: interference avoidance, Interference exploitation, and advanced relay techniques.

A primary feature of ARTIST4G is that theoretical and simulation studies of innovations are accompanied by lab and field trials, which give important input to fine tune and evaluate interesting concepts in realistic environments.

A first feedback on the implementation of all innovations in this first set was given in D6.1. The document also presents four different hardware platforms that are available within the ARTIST4G project. D6.1 shows that different aspects of hardware implementation and field trials can be addressed by using these platforms that range from complexity and power consumption studies of particular algorithms to field trial measurements in a representative test bed. A first set of field trial results were then presented in D6.2 which already showed the great bandwidth of the work done in the project.

The present deliverable presents results on a second set of innovations, including work that directly follows-up the studies presented in D6.2 and work on new topics that was triggered by the innovation process in WP1-3. Most of the results presented in this deliverable are linked to exposures of the same topic in another WP. Where this is the case, we will refer to these other sources that often give a more detailed view of algorithms together with simulation results which are complemented by the field trial results presented herein.

The trial and demo results span a wide range of topics. In particular:

- Measurements show gains of different 3D beamforming algorithms in particular lab and field trial scenarios (Section 3.1 and Section 3.2).
- An extensive implementation study of the downlink CoMP testbed implemented on MAGALI system on chip platforms (Section 3.3)
- The evaluation of uplink CoMP in practical environments was continued; including an investigation of potential techniques for the reduction of backhaul requirements such as compression algorithms and intra-site CoMP; a comparison of field trial measurements and simulations; the evaluation of joint detection on the moving relay feeder link (Section 3.4)
- Field trials on advanced relay concepts such as
  - CoMP on the fixed relay feeder link (Section 3.5.1).
  - Moving relays in the downlink using a predictor antenna concept in order to increase channel prediction performance which could boost downlink precoding and link adaptation (Section 3.5.2).
- Field trial verification of the Tortoise CoMP concept (Section 3.6.1).
- Simulation study on the performance of different linear and non-linear equalization concepts. In particular, performances of MMSE and ML are shown as benchmark to evaluate interference cancellation equalizers (Section 3.7).

## 3 Lab and Field Trial Results

### 3.1 Advanced 3D-Beamforming

#### 3.1.1 Introduction

Beamforming requires that multiple antennas are used to form the transmission or reception beam and to increase the signal-to-noise-ratio at the receiver. This technique can be used to improve coverage and to increase the system spectral efficiency. The increased signal-to-noise-ratio is not only due to a larger gain in the direction of the desired user, but also due to a better control of the spatial interference distribution in the cell. In WP1 techniques for advanced beamforming has been investigated and simulated for different scenarios [1].

Therefore the main target of the 3D Beamforming lab and field trials was to investigate possible improvements of the spectral efficiency and cell edge throughput for one and more terminals. Depending on the cell size and the height of the base station antenna above ground, the main lobe of the vertical pattern is directed towards the ground in the afar part of the cell.

As already published in [1] and [3] we have studied the influence of different antenna downtilts at a specific terminal location in a single cell scenario. For this we have used an antenna array with 4 antenna columns which can be tilted separately. It could be verified that small tilts shows improved receive signal strength at cell edge and high tilts at cell center. In a second step we enhanced the eNodeB emulator with an antenna array arrangement which allowed the emulation of vertical beam steering with adaptive algorithm. With this set up we made field trials in Stuttgart in a single cell scenario to verify the potential of 3D beamforming in a real propagation environment.

In the Dresden test bed, multi-site trials with variation of vertical downtilts are conducted to analyse the influence of neighbour cell interference to vertical beam steering. These are presented in Section 3.2.

#### 3.1.2 3D Beamforming Trials

##### 3.1.2.1 Description of Measurement Setup

A 3D beamforming prototype set up has been built with an eNodeB emulator, an active antenna array (AAA) and test UEs as shown in Figure 1. The AAA consists of 8 antenna elements with 8 cross-polarized dipoles in the vertical direction. This means the polarization of the beams is 45° as used in LTE networks, and the used frequency is 2.6 GHz with 10 or 20 MHz bandwidth. This provides a static sector pattern in horizontal direction, whereas in vertical direction a fully flexible beam pattern per resource block can be formed towards the UE location. Test signals with 8 data streams with dedicated pilots per antenna element are sent from the eNodeB emulator to the test UEs via the active antenna array with a CPRI Interface (Common Public Radio Interface) using vertical beam steering. The received signals at the test UEs are analysed and the optimum beamforming weights for each subcarrier are reported via a fixed link or a generic wireless link to the eNodeB and applied for the following time interval. This setup allows lab and field trials with quasi-real-time channel feedback in the uplink and is therefore suitable for proof-of-concept field trials covering different deployment scenarios and algorithms designed to feedback optimum beam pattern weights (see Ref [3]).

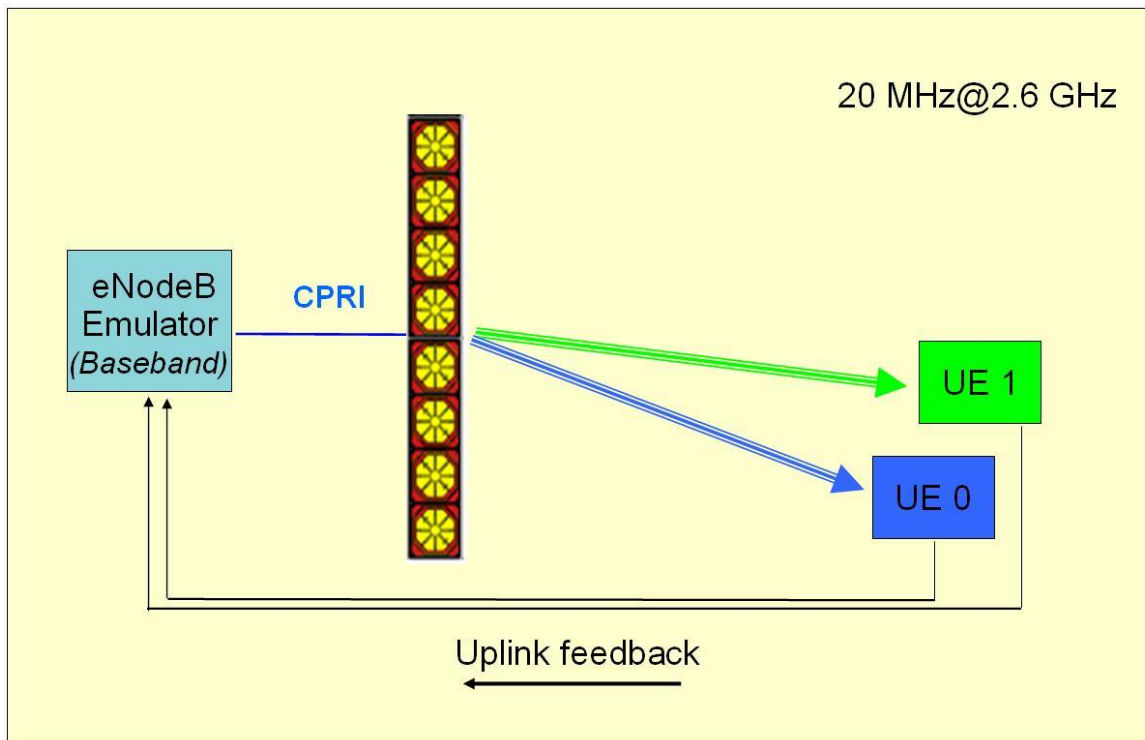


**Figure 1: Principle view of 3D beamforming Set up**

### 3.1.2.2 Lab Trials with 3D Beamforming

The behavior and performance of 3D beamforming with a fully adaptive zero-forcing algorithm has been tested in an indoor lab environment. The antenna array was mounted on a rack, with a height of 1.8 m for the center of the antenna array. Two test UEs (UE 0 and UE 1) are vertically mounted on two stages with a separation of only 20 cm in a distance of 4 m from the antenna array. The test UEs can be moved +/- 80 cm in vertical direction. This means that the minimum distance of the two UEs is 20 cm, if the vertical position is equal.

For a typical arrangement with a vertical separation of only 30 cm for the two test UEs a very good separation of the two beams can be achieved. This result is illustrated in Figure 2, where the received signal power of both UEs is shown. Both test UEs are operating with 20 MHz bandwidth and just to visualize the excellent separation of the wanted and unwanted signal the representation for each UE has been limited to 10 MHz. On the lower 10 MHz part of the spectrum the situation is shown as seen for UE 0 (blue curve), and on the higher 10 MHz part of the spectrum the situation for UE 1 (green curve) is shown.

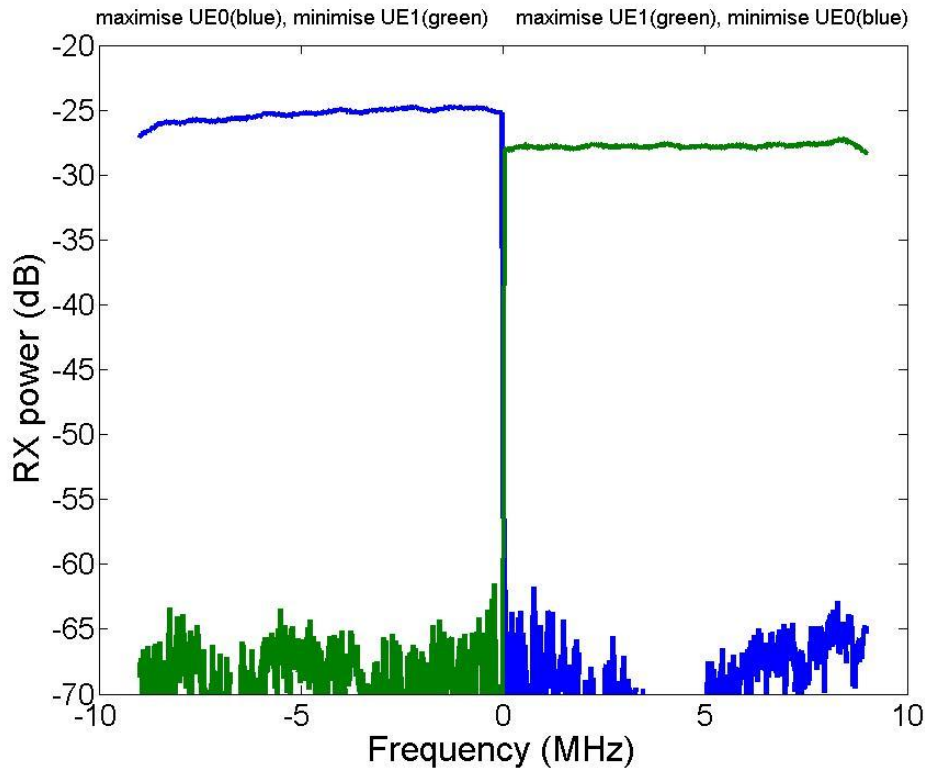


**Figure 2: Received Power for two UEs by using a zero forcing algorithm**

In this test the suppression of the unwanted test UE is more than 35 dB. Similar results can still be achieved when the two UEs are mounted close together with a distance of only 20 cm or even in the case of non-line-of-sight (NLOS) propagation conditions. In each case the adaptive algorithm takes advantage from the reflections from walls and surfaces in the room to achieve excellent performance.

### 3.1.2.3 Field Trials with 3D Beamforming

Proof-of-concept outdoor field trials were conducted for a macro cell environment with high buildings. For these trials the adaptive antenna array was mounted in a height of 7 m at a wall of a building. The beams were steered in direction of a straight street with presumably almost line-of-sight (LOS) propagation conditions, see Figure 3.

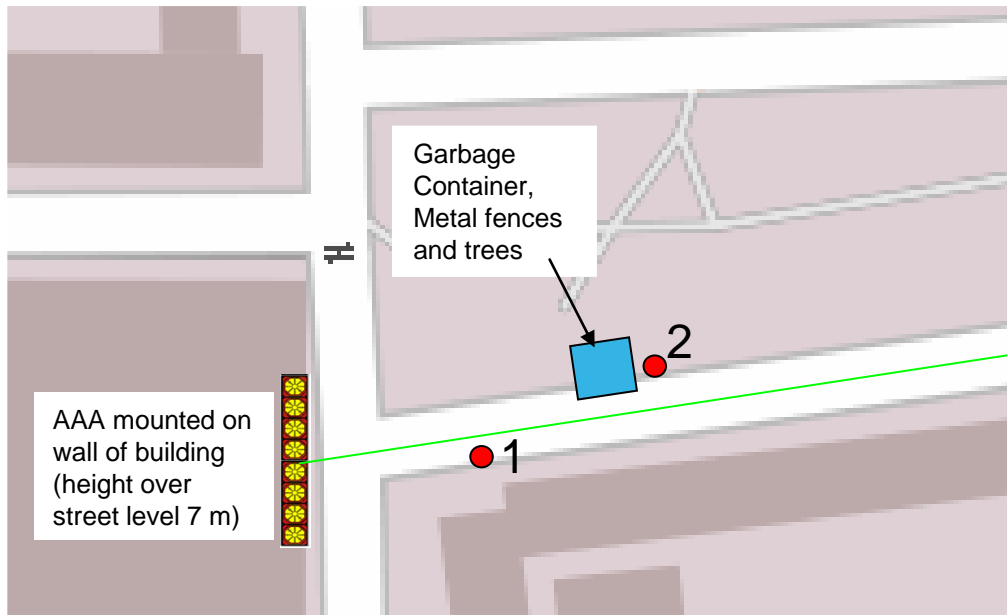


**Figure 3: Overview of field trial scenario (Source: Open Street View)**

The two test UEs were located in a test van and connected with 1 Rx antenna per UE mounted on the roof of the van with a separation of 50 cm.

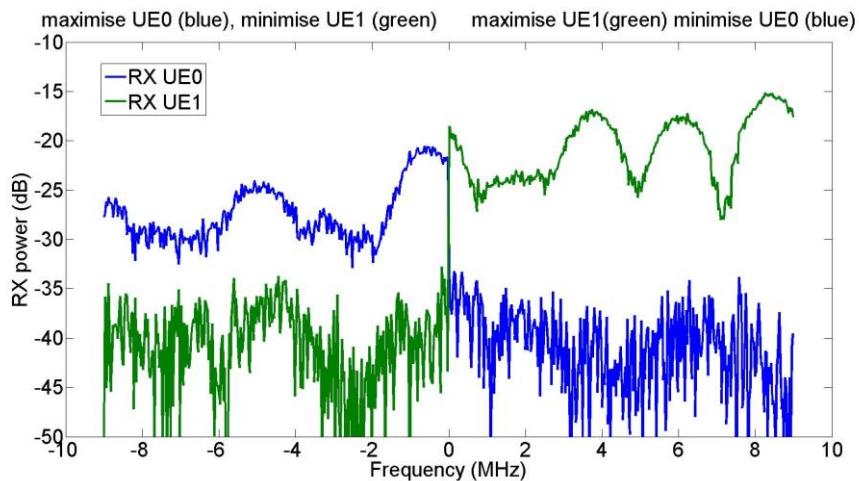


**Figure 4: Separation of the wanted and unwanted signal for LOS condition**

For a test with LOS condition the antennas were adjusted in the driving direction of the test van at position 1 in Figure 5, which was parked in a distance of approximately 20 m from the eNodeB antenna. It could be expected that a strong LOS component in the beams in such a straight direction between eNodeB antenna and van is present. But even for this LOS condition there are additional multipath components due to reflections as visible in the frequency response ripples shown in Figure 4. The signal of the two UEs could be separated reliably. The suppression of the unwanted test UE is depending on the frequency and ranges between 10 and 15 dB as shown in Figure 4.

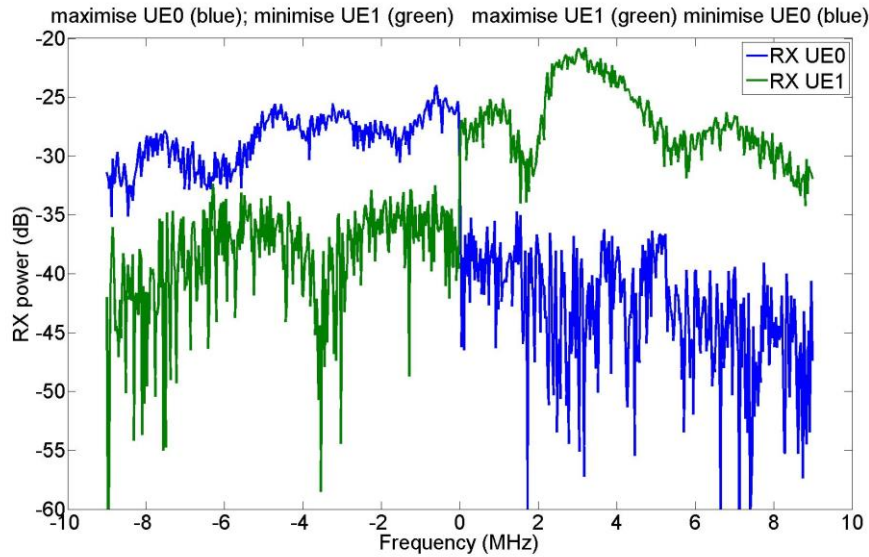


**Figure 5: Separation of the two signals for non line of sight condition**

In a second scenario the test van was parked in a distance of about 30 m from the eNodeB antenna array (position 2 in Figure 3). It is blocked by metal fences, metal garbage container and trees. Thus, there wasn't a strong LOS component present any longer. Again the two receive antennas on the roof of the test van had a separation of 50 cm. As shown in Figure 5, the suppression of the unwanted signal is varying between 0 and 20 dB depending on the frequency. In situations like this, system improvements are still feasible, but would require frequency selective scheduling in addition.

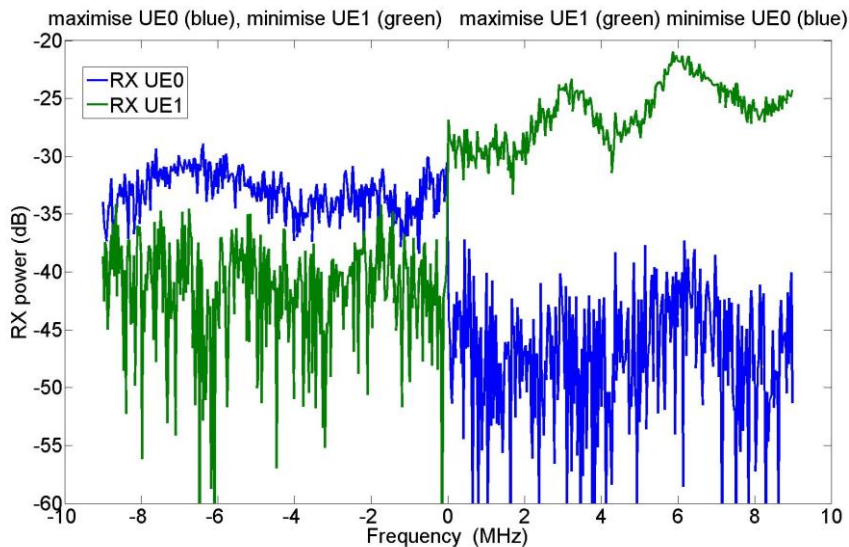


**Figure 6: Separation of the two signals for non line of sight condition for one UE and line of sight to the other**

In a third scenario the test van stayed at the same position (point 2 in Figure 3) as before with the NLOS condition, but with only one antenna on the roof of the van. The antenna of the second test UE was mounted on street level about 5 meters away at a position with a strong LOS component. As can be seen in Figure 6, the suppression of the unwanted signal is about 15 dB for UE 1 with the strong LOS component and below 5 dB for the mobile with NLOS condition. A reason for this asymmetry is that the received signal of the mobile with the LOS component (UE 1) is stronger than the signal of the UE with NLOS condition (UE 0). This

behavior indicates that the adaptive algorithm is working as reliable as before, but due to the different power levels the achieved advantage is smaller.

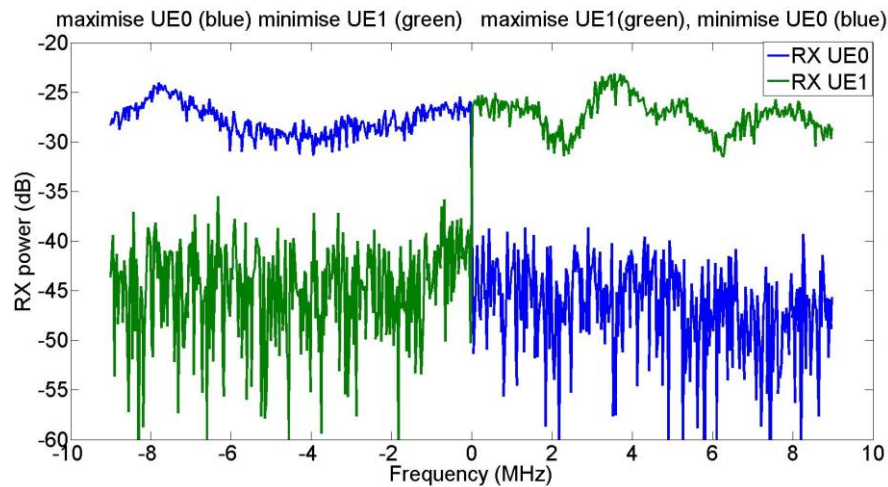


**Figure 7: Separation of the two signals for non line of sight condition for one UE and line of sight to the other with beam reflected from a wall**

Finally, in a fourth scenario, the transmitting antenna array at the eNodeB has been rotated horizontally, so that the boresight direction of the horizontal pattern pointed towards a high building nearby. In this scenario we expected strong reflections in the direction of the two test UEs. The arrangement of the receive antennas at the test UEs was kept as in the third scenario. The modified propagation conditions resulted in an improved performance for both UEs with a suppression of the unwanted signal of about 15 dB as shown in Figure 7.

The above presented trials in a typical outdoor environment show that quite high signal suppression can be achieved for fully adaptive algorithms. The suppression depends on the surrounding like metal fences, reflections from buildings and so on. Additional performance improvements are possible by using frequency selective scheduling. The best potential for signal separation is seen in scenarios with a high amount of reflections.

### 3.1.3 Conclusion

The conducted lab and field trials with adaptive vertical beamforming algorithm have shown significant improvements of the system performance with respect to the capability to separate two signals sharing the same radio resources by taking advantage of reflections from building, walls and other strong reflectors.

## 3.2 Field Trial Evaluation of UE Specific Antenna Downtilt in an LTE Downlink

### 3.2.1 Introduction

The benefits of horizontal beamforming in cellular networks are well understood, and the technology is already used in commercial products. Recently, vertical beamforming (basically a user specific DT) receives a lot of attention as well. However, available channel models do not allow for an accurate simulation of this transmission scheme. The publication [7] investigates the impact of antenna DT in a typical urban area using field trials. Two models are presented and compared with measurement data in order to study their value and limitations for the evaluation of vertical beamforming, which is an important basis for planning and deploying of such schemes in order to increase cellular DL throughput. In this publication [7], vertical beamforming could increase the SIR by about 5-10 dB, for a set of UE locations. Provided that appropriate simulation parameters are chosen, a task that can require a lot of calibration work, a very good match between measurement and a Ray Tracing model can be achieved. Under LOS condition, even when parts of the Fresnel zone are blocked, the impact of DT can even be modeled using a much simpler approach that only considers a simplified antenna pattern [11].

### 3.2.2 Field Trial Setup

The test bed consists of three BS located at different sites in downtown Dresden as depicted in Figure 8. Buildings within the test bed area are mostly 4-5 story apartments of similar height between 15 m and 19 m. In contrast, BS 1 and BS 2 are located on buildings of about three times that height. The Antennas of BS 3 are mounted in 33 m height over ground. Many trees are planted along the streets which are laid out in a checkered pattern. So, whether a UE has NLOS or LOS to the BSs may change quickly within few meters.

Each BS is equipped with a cross-polarized KATHREIN antenna. These antennas provide an electrical mechanism for changing the DT, which is used in addition to a pre-configured mechanical DT of  $5^\circ$ . For the measurements, a modified (OFDM based) LTE system was used, as described in [8][9]. The system enables the estimation of the physical CTF via CSI-RS that are transmitted on orthogonal sub-carriers over a bandwidth of 20MHz. CSI-RS are transmitted twice every ms (in every slot) for each antenna on every sixth sub-carrier. Thus,  $N_p = 200$  pilots are transmitted in every slot. Orthogonality of pilots of all BS in time and frequency is performed via a GPS-based synchronization with Meinberg GPS I70MP reference normals [10].



**Figure 8: BS deployment setup and UE measurement locations.**

For a first set of measurements, the UE test equipment from the company SIGNALION was built into a bicycle rickshaw, as shown in Figure 9. An antenna rotation table was mounted on top of the rack. Two dipole antennas were used at the UE, placed in about 40cm distance. A second set of measurements was conducted using the same UE carried on a bus. In these measurements, the same generally setup was used, including the rotating table which was mounted on the roof top at a height of 2.5m, compared to 1.5m on the rickshaw. In all measurements, a control notebook was used, running specific software to automate the measurements. To guarantee sufficient averaging of small scale fading, at every location, data from five different antenna positions was collected using the rotation table. The angle between the antenna positions was  $72^\circ$ , and each measurement was done for a duration of 30ms. Since pilots are transmitted twice per ms, in total  $N_s = 300$  OFDM Symbols are taken per location.



a) VW T4 measurement bus



b) Bicycle rickshaw



c) Antenna rotation table

**Figure 9: Measurement Equipment**

### 3.2.3 Modeling the Impact of Antenna Downtilts

Models for wireless radio channels can be classified into three categories: deterministic, empirical, and stochastic models. The former are in the focus of this correspondence. The radio channel is affected by the antenna patterns and the physical surroundings. In ARTIST4G, two different simulation models were compared with field trial information. The first, ray tracing, gives a simplified solution of Maxwell's equations for a modeled surrounding that is a very close representation of the actual physical environment. In the second simplified model a generic antenna pattern is assumed that is characterized by few parameters. The impact of the surroundings is *not* considered in this model at all. A detailed description of these models can be found in [7].

### 3.2.4 Results

The results for a subset of the measurement points above are presented in [7]. Therein, it's shown that vertical beamforming could increase SIR by about 5–10 dB. The measurement results were compared to two different models that describe the impact of DT on radio channels. Provided that appropriate simulation parameters are chosen, a task that can require a lot of calibration work, a very good match between measurement and ray tracing model can be achieved. Under LOS condition, even when parts of the Fresnel zone are blocked, the impact of DT can even be modeled using a much simpler approach that only considers the impact of the antenna pattern.

## 3.3 Downlink CoMP without CSI Feedback

### 3.3.1 Introduction

Implementation of CoMP concepts on the available hardware platforms will allow validating the theoretical results obtained by simulations which have been described in D6.2. Benefits of CoMP in terms of coverage and cell edge throughput are investigated by considering real world conditions through lab and field trials. The CEA hardware platform is used for the implementation of DL CoMP Joint Processing without CSI feedback. The distributed MIMO scheme considered here is the double Alamouti (4x2) that combines the robustness of the Alamouti coding [30] with rate doubling ability. Data symbols are separated in two streams, each one using the Alamouti space-time block coding principle on a pair of antennas (a pair of antenna located at each base station).

This particular scheme is being studied in order to assess the improvements in terms of bit rate and robustness, compared to the well-known Alamouti scheme in an interference-limited scenario.

The test of downlink CoMP without CSI feedback has been compared between two scenarios: a scenario with interference and a scenario with cooperation. In the first scenario an eNodeB transmits data to the UE when another eNodeB is interfering. In the second scenario both eNodeB are cooperating to transmit data to the UE. Data bits are split in two streams, each one using the Alamouti space-time block coding principle on a pair of antennas (a pair of antenna located at each eNodeB).

At a first step, we compare in the following the performance of the two scenarios based on simulation results. Then we describe the hardware implementation on a Network-on-Chip (NoC) based hardware platform and the final set-up for lab trial measurements. The goal of such an implementation is firstly to provide feedbacks on the computing complexity and on the power consumption of complex scenarios. Then it will also allow performing measurements in order to

validate the concept of DL CoMP in the real world. Finally, possible System on Chip architecture evolution for next generation LTE-A will be given taking into account the lessons learnt from the hardware implementation.

### 3.3.2 Description of interference and cooperation scenarios

In this study the performance of two scenarios, called “cooperation” and “interference” scenarios, are evaluated. For both scenarios the setup of the simulation is described by Figure 10: a UE is positioned on the segment [eNodeB1 eNodeB2] formed by two adjacent eNodeBs. The distance between eNodeB1 and the UE is called  $d$ .

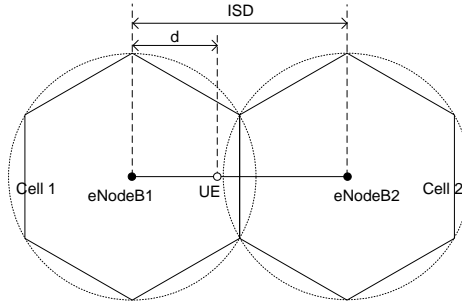


**Figure 10: Context of the study**

In the cooperation scenario, eNodeB1 and eNodeB2 cooperate to transmit data to the UE. The data bits for the UE are split into two streams between the two eNodeBs. Each eNodeB uses the Alamouti space-time block coding on a pair of antennas. The UE is equipped with two receive antennas and performs double Alamouti (4x2) decoding. This scenario is described by Figure 11.

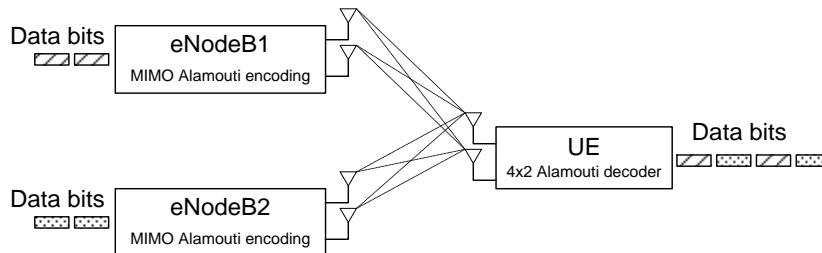


**Figure 11: Cooperation scenario**

In the interference scenario (see Figure 12), eNodeB1 transmits data to the UE while eNodeB2 is interfering. eNodeB1 and eNodeB2 are each equipped with two transmit antennas and perform Alamouti space-time block coding. The UE is equipped with two receive antennas and performs classical Alamouti decoding on each receive antenna followed by an MRC recombination of the signals from the two antennas.

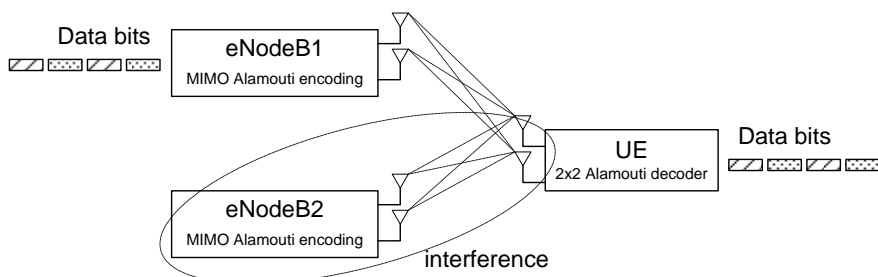


**Figure 12: Interference scenario**

The software simulator used for both scenarios is described by Figure 13. The main parameters of the simulator can be found in Table 1. For each eNodeB, data bits go through the channel coding module. They are then interleaved and mapped into constellation symbols. Those symbols are MIMO encoded using Alamouti scheme. The two resulting streams of symbols are then processed independently.

A more detailed description can be found in D6.2 §3.3.2.2.

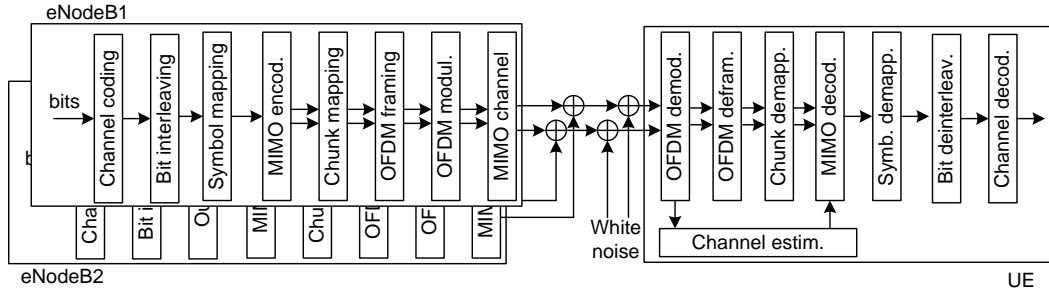


**Figure 13: Software simulator**

**Table 1 Main parameters of the software simulator**

	Mode 1	Mode 3	Mode 5
Nb of OFDM symbols per frame	14		
Nb of data OFDM symbols per frame	10		
FFT size	1024		
Nb of useful carriers	600		
Nb of bits per modulation symbol	2	4	6
Nb of users	50	25	5
Nb of Resource Blocks per user	1	2	10
Equalization	ZF		
Channel coding	Duo-binary turbo codes		
Coding rate	1/2	2/3	3/4
Channel estimation	Frequency filtering + time interpolation		

### 3.3.3 Testbed implementation on hardware platform

The test of downlink CoMP without CSI feedback has been carried out along the project in three implementation steps:

1. Test of 4x2 (double Alamouti) downlink receiver: this first step implements a 4x2 DL receiver.
2. Test of 2x2 downlink: The setup in this intermediate step consists of one UE and one eNodeB implementing a 2x2 downlink scheme and is used as a reference point for performance comparison.
3. Test of virtual double Alamouti: this test consists in implementing a distributed double Alamouti scheme on a test bed composed of two eNodeB and one UE.

In each implementation step, the CEA platform has been used to enable specific measurements in terms of complexity and power consumption related to the new algorithms implemented on the MAGALI ASIC. Processing time and reconfiguration time between modes are also evaluated and delivered as input to WP1-WP2-WP3. These figures of merits are indeed relevant inputs for WP1 since double Alamouti scheme is also studied within WP1 for the uplink scenario (see single cell Double Codeword SU-MIMO/MU-MIMO proposal in Section 4.1.4 of D1.2 [22]).

D6.1 [20] provides the implementation feedback connected to the first step and compares expected results from simulations with measurements made on the demonstrator hardware.

D6.2 [2] describes the simulation set-up and results done as a reference for the hardware implementation step. It also provides some implementation feedback on the 2x2 downlink transmitter related to the second implementation step.

This section describes the final set-up related to the third implementation step and some implementation feedbacks on the 2x2 downlink receiver. It provides the testbed architecture and the application mapping. Hardware implementation complexity will be also discussed.

### 3.3.3.1 Step 1: test of 4x2 (double Alamouti) downlink receiver

Based on the 4x2 (double Alamouti) downlink receiver, the first case study has been already developed and implemented onto the CEA platform. The objective is to map the receiver algorithms on the hardware components of the platform: the last bit-level operations (descrambling and CRC checking) are handled by the FPGA while the main data stream and all highly computational functions are mapped to coarse-grained reconfigurable hardware IPs (MEPHISTO DSP) available in the MAGALI chip. Deliverable D6.1 provides detailed information about the application mapping process and gives the implementation feedback connected to it. It compares expected results from simulations with measurements made on the hardware demonstrator. The comparison analysis enables an early feedback on the implementation scheme to provide some requirements for refinement of step 2 and 3. The implementation complexity analysis made on the hardware demonstrator shows that the 4x2 downlink receiver requires ~55% of MAGALI chip operators which represents ~17mm<sup>2</sup> of 65nm silicon and consumes around 120mW. We've achieved a good trade-off between area and power consumption thanks to the SoC heterogeneous architecture (with mixed HW and SW based operators). The processing time measurements show that, when mapped onto a DSP or onto a dedicated hardware, the performances (processing time) of a standalone algorithm is in line with the expected results given from simulations. We have also assessed the data streaming and re-configuration capability of the operators but, to achieve a product level quality, it requires embedded SW optimization to reach real time processing, an application compiler tool to ease the implementation, debug capabilities and data traffic monitoring. This first step implementation has also improved the MAGALI chip maturity through a full and real application mapping. All encountered hardware bugs have been fixed by software thanks to the reconfigurable hardware.

A first live demo showing the processing of a 4x2 downlink receiver implemented in the MAGALI platform has been made at the FNMS June 2011 in Warsaw.

### 3.3.3.1 Step 2: test of 2x2 downlink

The implementation of the DL CoMP scenario requires three nodes: two base stations and one receiver. To enter progressively into complex system integration, an intermediate implementation step consisting of a 2x2 downlink scheme with two nodes has been set-up. To build the complete 2x2 downlink testbed, a 2x2 transmitter has been developed and implemented onto the CEA platform while the 4x2 receiver has been modified to support the 2x2 Alamouti receiver. Two boards are required to set up the testbed, one for the transmitter and the other one for the receiver.

Deliverable D6.2 provides detailed information about the application mapping process for the 2x2 transmitter and gives the implementation feedback connected to it. It compares expected results from simulations with measurements made on the demonstrator hardware. The comparison analysis enables feedback on the implementation scheme to provide some requirements for refinement of step 3. The implementation complexity analysis made on the hardware demonstrator shows that the 2x2 downlink transmitter requires ~35% of MAGALI chip operators which represents ~11mm<sup>2</sup> of 65nm silicon and consumes less than 80mW. We've achieved a good trade-off between area and power consumption thanks to the SoC heterogeneous architecture (with mixed HW and SW based operators).

The 4x2 (double Alamouti) downlink receiver developed for Step 1 has been modified to support the 2x2 receiver Alamouti scheme. The receiver is the same as the one described in D6.1, except that the MIMO decoder is based on the 2x2 Alamouti scheme. Thus there is only one data stream at the output of the MIMO decoder. The 2x2 receiver implementation has not been optimized in order to gain some time in the test bed development. Only the MIMO decoder micro-code has been adapted for 2x2 Alamouti decoding. The data related to the third and fourth transmit antennas have been ignored in the processing pipeline. For this reason, this is meaningless to provide figures on the implementation complexity since the measured TTI decoding chronogram of the 2x2 receiver is very close to the one given in D6.1 for the 4x2 receiver in figure 20. Nevertheless a complexity comparison of the 2x2 MIMO decoder implementation on MEPHISTO DSP is given below but only in terms of number of operations as shown in Table 2.

**Table 2: Compared number of operations between 2x2 and 4x2 MIMO decoder**

Operation	2x2 MIMO decoding	4x2 MIMO decoding
Instruction RAM accesses	501	5307
In/Out data accesses	720	840
Data accesses	1801	16820
MAC	1390	16590
Total operations	4412	39557

The total number of operations is multiplied by 9 going from the 2x2 to the 4x2 MIMO decoders. It clearly shows the increasing computing requirement for the complex MIMO schemes. As said previously, we can see that no effort has been put on the pipeline optimization of the 2x2 MIMO because the number of In/Out data access doesn't reflect the theory. Indeed, the 4 antenna data streams are still read by the 2x2 MIMO decoder but only 2 streams are computed.

As for the 4x2 receiver, the processing time measurements show that, when mapped onto a DSP or onto a dedicated hardware, the performances (processing time) of a standalone algorithm is in line with the expected results given from simulations. We have also assessed the data streaming and re-configuration capability of the operators. This second step implementation has improved the MAGALI chip maturity through a full and real application mapping. All encountered hardware bugs have been fixed by software thanks to the reconfigurable hardware. The new developed algorithms related to the transmitter and the modified algorithms related to the receiver have been developed in an assembly language with a limited debug capabilities and data traffic monitoring. We would have saved development time with the usage of compilation tools for both the DSP algorithms and the full application mapping.

**3.3.3.2 Step 3: Test of virtual double Alamouti**

The implementation of a distributed double Alamouti scheme on a test bed composed of two BS and one UE is evaluated in the next step. Lab trials with CEA's prototype aim to test and assess the performance of DL CoMP algorithms versus the two scenarios described in Section 3.3.2: interference and cooperation. We will consider the following setup: two base stations and one user equipment, as can be seen in Figure 14. The validation of the implementation and the performance gain assessment will be done with emulated channel conditions (channel emulator in FPGA).

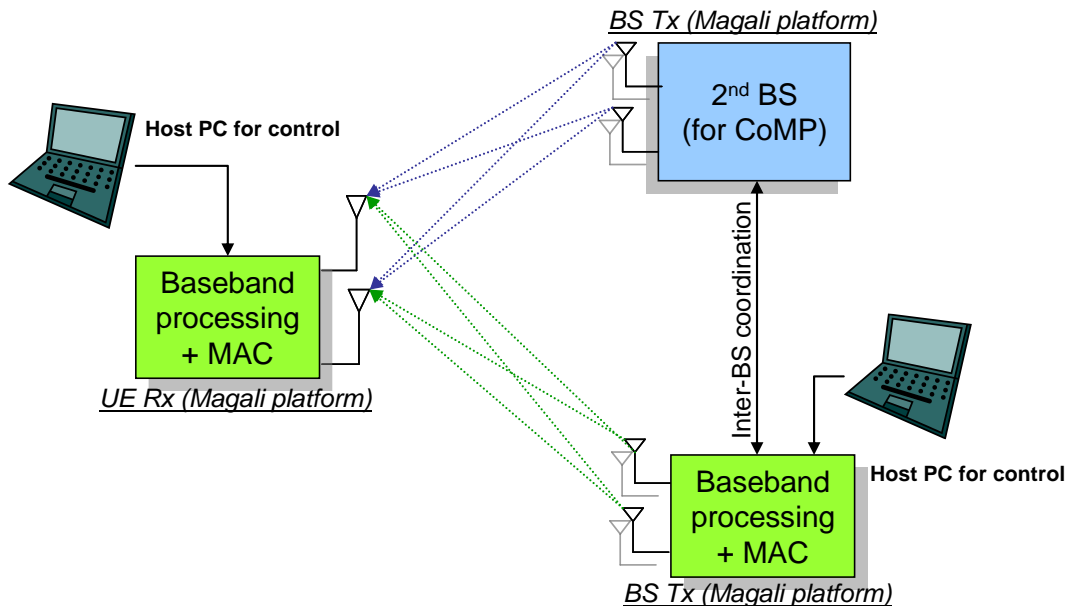


**Figure 14: Typical measurement scenario for investigation of DL CoMP (CEA testbed)**

### 3.3.3.2.1 Testbed architecture and application mapping

The CEA test bed consists of three MAGALI boards (Figure 15). On two of them the 2x2 transmitter is implemented and on the third one the 4x2 receiver is implemented with the last bit-level operations handled by the FPGA and the main data stream and all highly computational functions mapped onto the MAGALI hardware resources. A host PC controls the three boards through an Ethernet link. For each transmit board, the application mapping is described in D6.2. The input data (the modulation of 14 OFDM symbols of 1024) are provided by the host PC, then the modulation scenario is divided into 3 distinctive phases computed onto the MAGALI hardware resources and finally the antenna I/Q data are temporary stored in a MAGALI internal memory. Since the performance measurements are done under emulated channel conditions, the antenna signals are transmitted without any RF board but on a high speed LVDS wired link between the boards. The data interfaces between the boards are the NoC router which means that the full hardware test bed is considered as a single network on which all resources required for the DL CoMP processing are mapped. This implementation simplifies a lot the synchronization between the boards because it is not necessary to add additional control data. Indeed, all processing phases are synchronized thanks to the hardware built-in data flow control implemented in MAGALI chip and FPGA. The two antenna streams of one of the eNodeB (BS2 in Figure 15) are transmitted by the FPGA from the internal MAGALI temporary storage to the second eNodeB FPGA (BS1 in Figure 15). This later merges its own I/Q data with the received BS1 streams. The resulting four I/Q data streams are sent to the receiver board (UE) through the LVDS wired link.

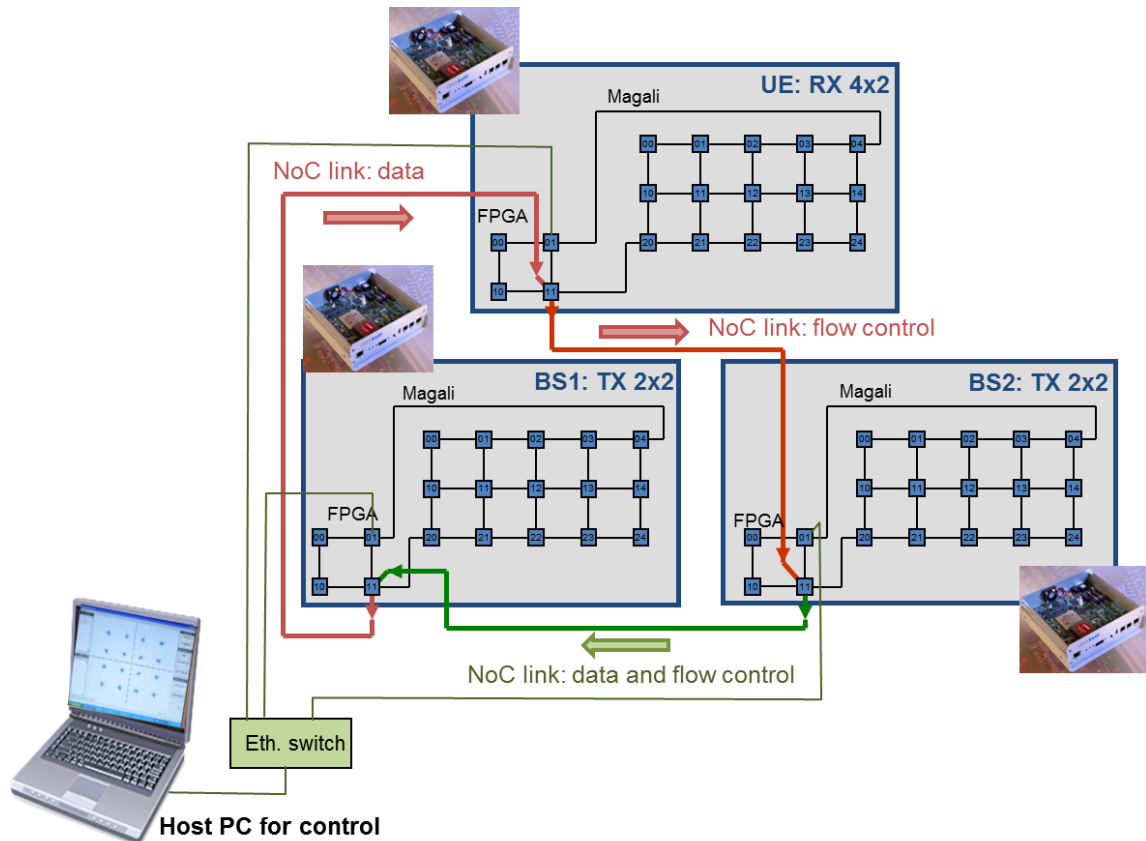


**Figure 15: CEA Downlink CoMP testbed architecture**

The third board emulates the UE on which the 4x2 Alamouti scheme is implemented. In addition, the board contains the channel emulator. As a first step, the FPGA receives the four data streams. The emulated channel between each transmit and each receive antenna is a multipath channel defined by three parameters: the number of paths, the delay and the attenuation of each path. The channel used for the simulations below has two paths. It is described by Table 3.

**Table 3. Channel parameters**

Path number	Delay (samples)	Amplitude
1	0	0.6016
2	3	0.7578

Antennas at each eNodeB are supposed to be uncorrelated. A random phase is then applied to the channel between each transmit antenna and the two receive antennas. The application mapping of the channel emulator is shown on Figure 16. The UE FPGA also provides the possibility to reduce the signal transmit power to emulate the distance between the eNodeB and the UE. The selection between the interference scenario testbed and the cooperation testbed is done via a software switch in the UE FPGA and controlled through the host PC.

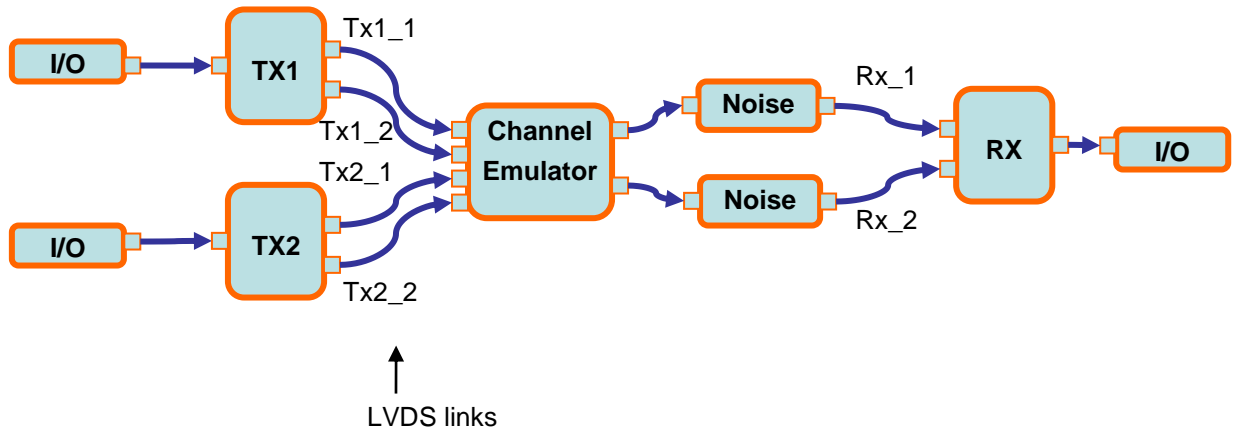


**Figure 16: UE FPGA application mapping**

Finally, the 4x2 RX application mapping is strictly identical as the one described in D6.1. The decoded data are stored on MAGALI internal memory and could be easily dumped from the host PC to be used for performance measurement purpose.

The control of the three MAGALI boards from the host PC has required the development of a new Ethernet IP block implemented on the FPGA of each board.

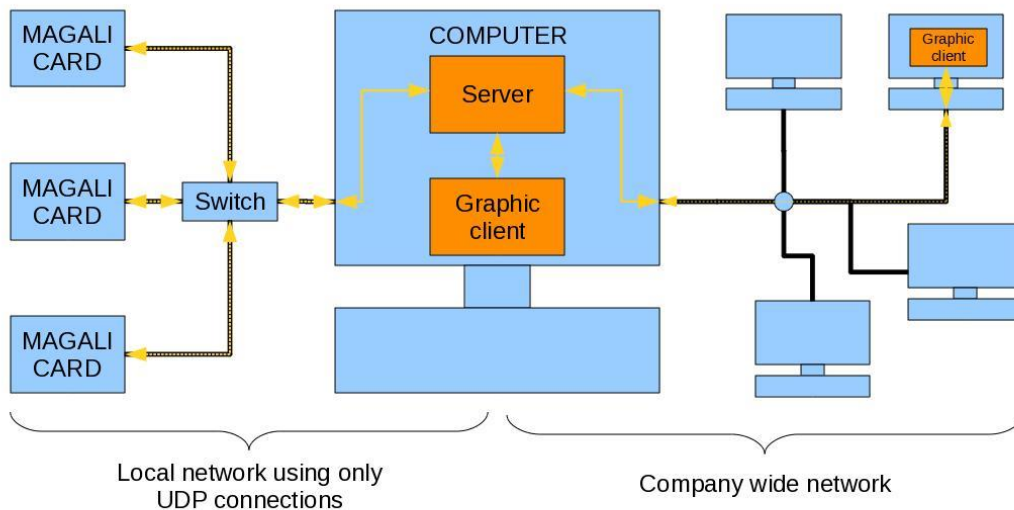


**Figure 17: PC to board communication system**

Until now, the Ethernet connection was only able to manage a point to point connection. Therefore, it was not possible to plug every board on a single network and the configuration

process was very slow. Our recent work on the Ethernet IP within the FPGA allows us to create a real network.

The FPGA contains a full MAC/IP/UDP stack and a dynamic IP attribution system. Every board has to be connected to a switch and a computer also needs to be connected to the same switch (Figure 17). The computer hosts a tiny cross-platform software which handles the network.

The software is a server; it distributes IP addresses as cards are plugged in or off and implement a flow control system with the board allowing any client to communicate in an easy way. In order to communicate with a board, it is possible to either interact directly with the server or to create a client and to connect it to the server.

As the server has been designed to be generic and fast, it is not the most convenient way to interact with a board. It is better to create a client with an interface which suits the specific needs of the user. The client can then communicate with the board through the server. Clients are software which can be run on the same computer as the server or remotely from another computer. As the communication is standard, it can be programmed in any language on top of which one can build graphic user interfaces or convenient shell programs.

This system allows to dynamically configuring all the boards on the network synchronously. Thus, it permits the automation of tests that require varying parameters of multiple boards dynamically.

#### 3.3.3.2.2 Feedback on hardware implementation complexity

The final hardware complexity for the full downlink CoMP based on 4x2 distributed Alamouti transmission scheme represents:

- Three MAGALI boards: two transmitters (eNobeB1 and eNodeB2) and one receiver (UE).
- One host PC.
- Cable connections between boards.

On the transmitter side, the 2x2 TX implementation complexity analysis shows that it requires ~35% of MAGALI chip operators which represents ~11mm<sup>2</sup> of 65nm silicon and consumes less than 80mW. The transmit FPGA implements several processing units involved in data flow control (link adaptation between the MAGALI SoC and the FPGA device), in data processing like the channel coder and in host control with the Ethernet IP block. The TX board FPGA is a Virtex5 FX130t from Xilinx. The TX FPGA application occupies 7930 slices out of the 20480 available which represents 38%.

On the receiver side, the 4x2 RX implementation complexity analysis shows that it requires ~55% of MAGALI chip operators which represents ~17mm<sup>2</sup> of 65nm silicon and consumes around 120mW. The receive FPGA implements the processing units involved in data flow control (link adaptation between the MAGALI SoC and the FPGA device), in data processing like the channel decoder, in host control with the Ethernet IP block and in channel emulation and noise generator. The RX board FPGA is a Virtex5 LX220t from Xilinx. The RX FPGA application occupies 31118 slices out of the 34560 available which represents 90%.

### 3.3.4 Performance assessment – from simulation results to laboratory measurements

#### 3.3.4.1 Simulation description

The configuration of the simulator is described by Figure 18. A two antenna UE is located between two two antenna eNodeBs: eNodeB1 and eNodeB2. The transmit power of each eNodeB can be modulated. The distance between the two eNodeBs is  $ISD = 500$  m. The distance between eNodeB1 and the UE is called  $d$ . The channel between each transmit antenna of each eNodeB and each receive antenna of the UE is a two path channel with delays 0 and 3 samples. The second path has an amplitude slightly larger than the first path.

Two scenarios are considered:

- Interference: the UE receives data from eNodeB1 while eNodeB2 is interfering.
- Cooperation: the two eNodeBs are cooperating to transmit data to the UE.

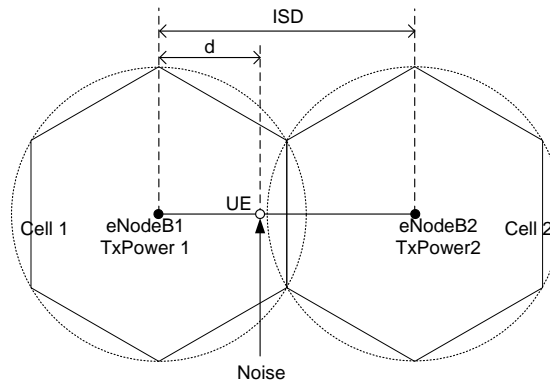


Figure 18: Simulator Configuration

### 3.3.4.1 Methodology

The performances of the two scenarios are measured for different values of the position of the UE. The measurement set-up described hereafter and the selected parameters have been defined in order to be easily reproduced on the hardware platform.

For a distance  $d=250$  m (i.e. a UE located midway between the two eNodeBs) the transmit power TxPower1 and TxPower2 of the two eNodeBs are set to 0 dB. The white noise power is set to -46.76 dB in order to obtain at the UE side an SNR consistent with the SNR that would be seen at the UE side in a transmission with path loss, Noise Factor, cable loss, antennas gains and thermal noise taken into account.

TxPower1 is then increased from 0 to 9 dB while TxPower2 is decreased from 0 to -9 dB, simulating a UE moving closer to eNodeB1. For each couple (TxPower1, TxPower2) the corresponding distance  $d$  is computed thanks to the path loss formula for a NLOS transmission, with  $d$  in meters:

$$\text{PathLoss} = 42.8 \times \log_{10}(d/1000) + 151.10 \text{ dB}$$

### 3.3.4.1 Simulation results

The performances are given in BER (Figure 19) and throughput (Figure 20) for mode 3 (see Table 1). The throughput is given in percentage of the maximum achievable throughput, i.e.  $100 \times (1 - \text{FER})$ . It can be noticed that with no cooperation (blue curves with diamonds) the performance start degrading from a distance  $d=165$  m from eNodeB1 (the throughput falls and the BER raises). With cooperation (red curves with squares) the maximum performance is reached (BER of 0 and 100 % throughput) from a distance  $d=235$  m.

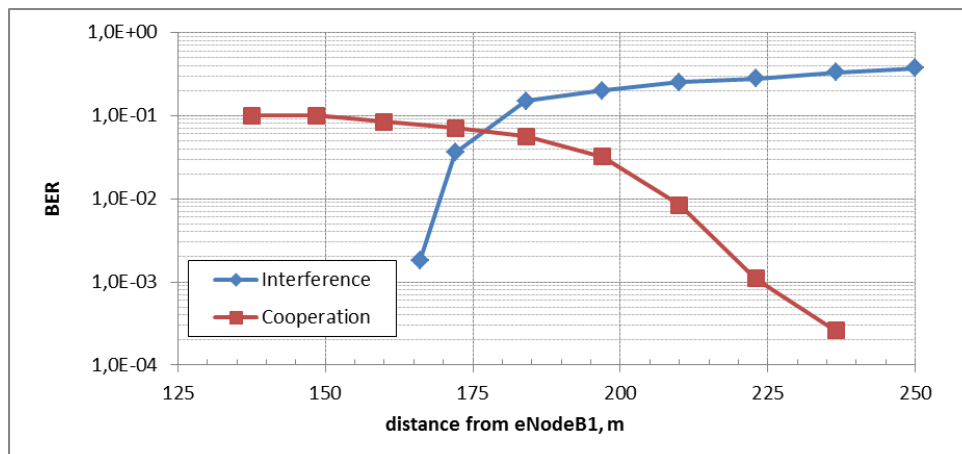
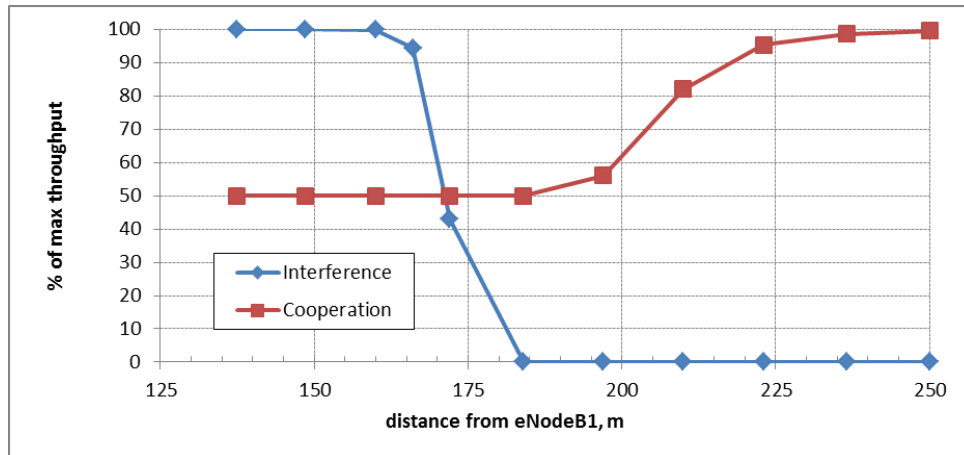


Figure 19: Bit Error Rate as a function of the position of the UE



**Figure 20: Achievable throughput as a function of the position of the UE**

So there is an area ( $165 \text{ m} < d < 235 \text{ m}$ ) where the UE experiences strong interference and in the same time where the cooperating eNodeB2 is too far away to allow efficient cooperation. A solution would be to use a stronger MCS in this area, like mode 1 (QPSK 1/2).

#### 3.3.4.1 Laboratory measurements

The measurement methodology used to assess the performance of the cooperation scenario versus the interference scenario from simulations, has been mapped onto the hardware platform. Figure 14 and Figure 15 are showing the testbed architecture. To emulate the simulation measurement conditions onto the real-time hardware platform, the following hardware set-up has been developed:

- eNodeB1 transmitter mapped onto one MAGALI board (2x2 TX mode 3) ,
- eNodeB2 transmitter mapped onto a second MAGALI board (2x2 TX mode 3) ,
- UE receiver mapped onto a third MAGALI board (2x2 RX for interference scenario and 4x2 RX for cooperation scenario),
- Channel emulator mapped onto the FPGA of the UE MAGALI board,
- The three boards are connected with LVDS links which convey the Network-on-Chip data and control (see figure 15),
- Transmit power (TxPower1 and TxPower2) set in the channel emulator hardware with multipliers/dividers,
- White noise power set in the noise generator block (see figure 16),
- Dynamic configuration and measurement automation mapped onto the host PC.

Prior to the hardware integration, the scenarios are mapped onto a fixed point co-simulation model developed in the context of WP6. This simulation platform which is built from VHDL or SystemC views of each operator consists in a functional model made of the three MAGALI chips, the three FPGA and the NoC links between the components. This model reproduces the hardware architecture showed in Figure 15 and is considered as the golden reference model which is bit-accurate with the hardware.

At the time of writing, the testbed implementation of the proposed advanced innovation is under test and validation. The measurement results presented in this section are coming from our bit-accurate golden model especially for the interference scenario. Several over-night simulations have been run with different transmit power values. The resulting data are dumped to allow BER computation off-line.

Figure 21 presents the performance comparison of the BER for the interference scenario between the algorithm developed in 3.3.2 (blue curve) and the algorithm mapped onto the bit-

accurate functional model. From this first test we can see that the results are aligned and that the degradation between the floating point model and the fixed point bit-accurate platform is very low.

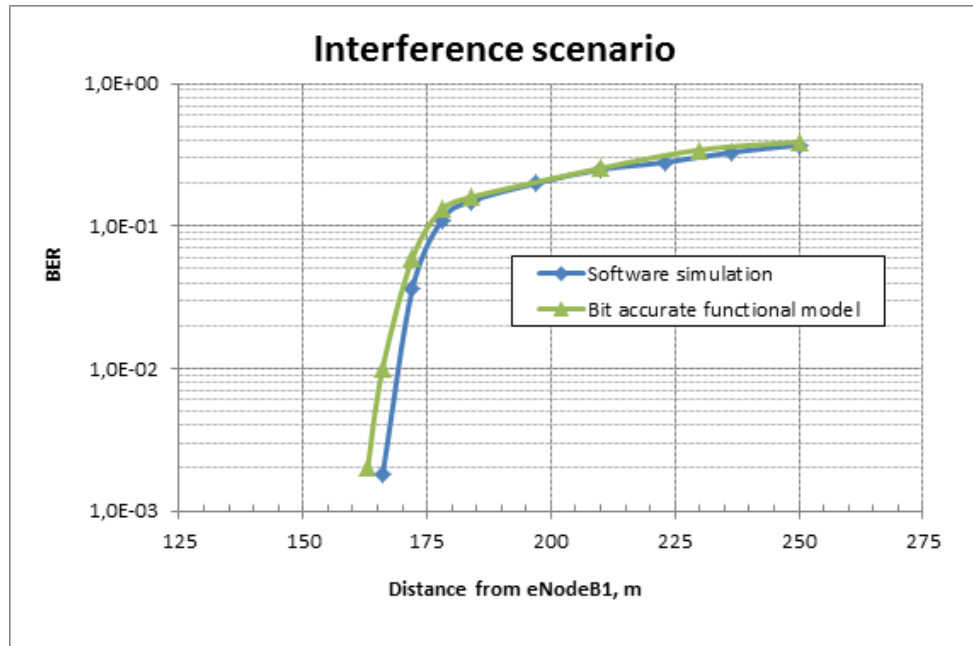


**Figure 21: BER comparison between the software simulation and the hardware mapping**

Since those measurements are obtained from a bit-accurate platform, it assesses the hardware mapping methodology and the parameter set. The mapping onto the real-time hardware will allow wider measurement campaign for both scenarios (interference and cooperation) with various parameters and data sets. The real-time processing of the MAGALI board and the test automation allowed by the host PC will provide an efficient hardware emulator for validating complex cooperation scenarios required to improve the cell-edge throughput performances.

### 3.3.5 Possible System On Chip architecture evolution for next generation LTE-A

Coordinated Multi-Point (CoMP) concepts, such as multi-cell downlink joint transmission schemes, require highly efficient System on Chips (SoC) embedding processing units to tackle with the increasing signal processing algorithmic complexity at the mobile terminal. Such a hardware platform also needs to be flexible for handling a large range of radio access technology with specifications moving fast. In Artist4G project, we've seen the hardware complexity associated with a 4x2 MIMO decoder implemented on a single baseband SoC. Next generation of LTE technology will increase drastically the hardware complexity linked to more complex MIMO schemes and iterative receivers. This will require PHY layer hardware architecture evolution while keeping flexibility and low power consumption especially needed for the UE baseband SoC.

A possible SoC evolution could rely in designing baseband SoCs with more advanced technology nodes. But today, System-on-Chips (SoC) designers are facing several problems that limit the economic benefits of such advanced technology nodes: in addition to the prohibitive cost of masks (which has already exceeded 1 million euro according to the ITRS), wafer fabrication is becoming more and more expensive mainly due to large-sized circuits that reduces manufacturing yield. Moreover, Non Return Engineering (NRE) costs needed for designing such a complex SoC become prohibitive.

A good alternative solution to develop economically competitive products is to reuse masks to address a wide range of systems and to fabricate small-sized circuits to increase yield. To do so, a proposal is to design a modular circuit that could be stacked using 3D integration technologies in order to build systems with processing performance adapted to several

application requirements. 3D integration technology consists in stacking many circuits vertically and interconnecting them using Through-Silicon-Vias (TSVs). This results in smaller circuit footprint and shorter vertical interconnections, which improves system performance and power (Figure 22).

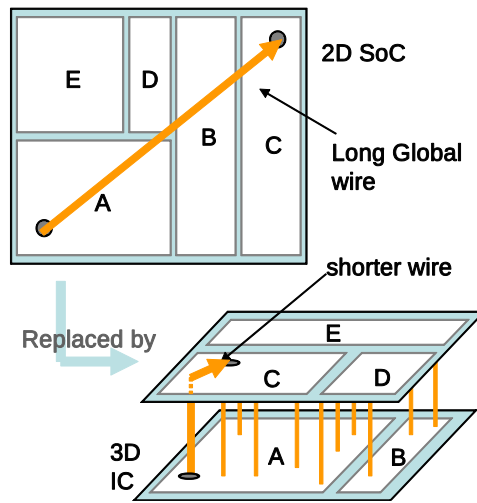


**Figure 22: Interconnection length shortening in 3D ICs**

Scalability and modularity of the performance is a competitive advantage brought by 3D TSV technology. The idea is to use stacking of simple dies for obtaining similar performance than a large die. It will then reduce the fixed costs and open the way to a range of low-end to high-end markets for a single die. One example is given in Multiple Input Multiple Output (MIMO) telecommunication applications: a single chip can be used for a single antenna, and stacking of multiple chips will upgrade the performance and the number of antennas that can be processed in parallel. Figure 23 shows an example of a complex 3D Integrated Circuit computing a complex MIMO mode of transmission using several SISO SoC.

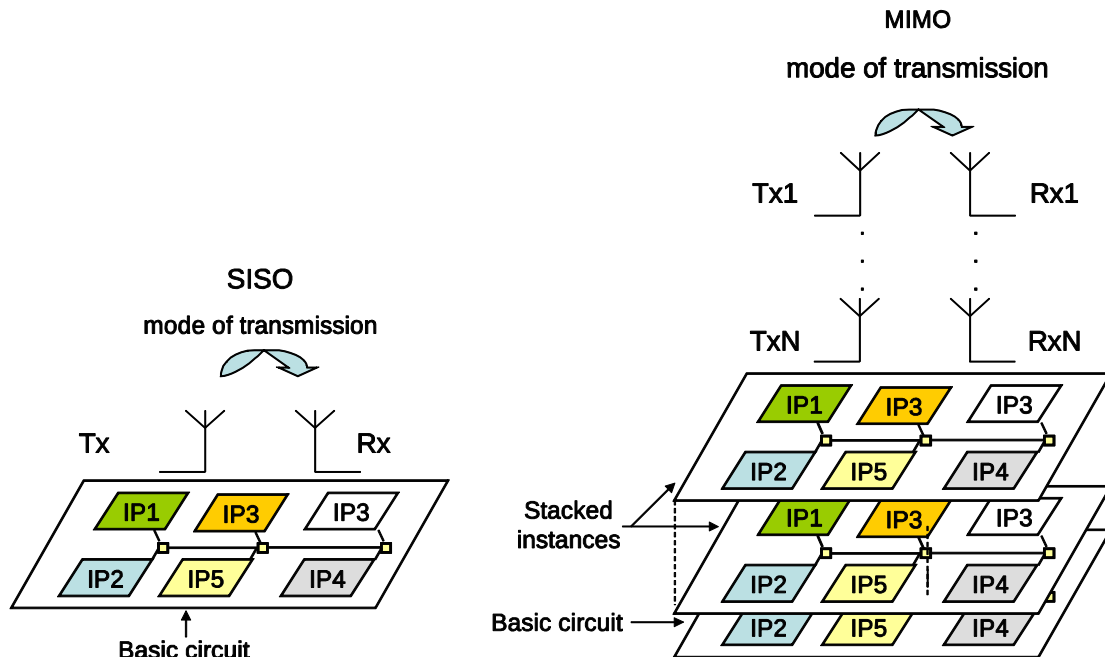


**Figure 23: 3D reconfigurable circuit obtained by stacking multiple instances of a same basic circuit**

In Artist4G we focused on modular architectures for 3GPP LTE telecom applications which have stringent performance requirements. As a first step, with MAGALI SoC, we've proposed a reconfigurable circuit that meets the 4x2 MIMO scheme of transmission in several modes using

two reception antennas. By stacking multiple instances of this same circuit and performing some software reconfigurations, it would be possible to boost overall system performance and address more complex MIMO schemes which includes the processing of more than two antenna streams on the UE receiver side.

For this new generation of architecture based on 3D Integrated Circuits, efficient communication between computing cores in the stacked system is essential. A vertical extension of the existing Network-on-Chip interconnect used in MAGALI, is the fundamental element for dealing with this stacking architecture issue. Scalability, modularity and low power are some of the advantages brought by 3D technology. But inter-die interconnect pitch, which cannot probably go smaller beyond the  $\mu\text{m}$  scale, is far from intra-die via density. The consequence is that several architecture choices have to be done to make the 3D interconnect scheme efficient:

- Reduced 3D topology:

Only few selected NoC links are connected vertically. Such a choice has some consequences on the resulting 3D bandwidth which must be taken into account for the 3D dies partitioning.

- Hierarchical 2D-3D routers for avoiding high-radix routers:

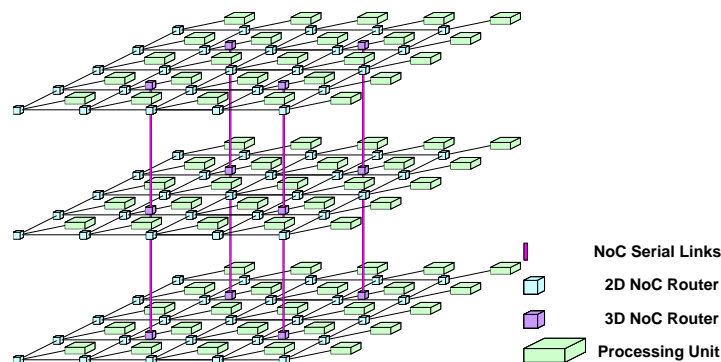


**Figure 24: 3D NoC topology using hierarchical routers and serial links**

Figure 24 shows an example of a 3D NoC architecture corresponding to these choices. The vertical connection is based on some vertical links, while intra tier horizontal communication are using traditional 2D NoC as in MAGALI SoC. The 3D router micro architecture is based on a hierarchical router composed of a router dedicated to intra-tier communication and another router for vertical communication. The vertical links could be serialized to minimize the number of vertical interconnections.

- Asynchronous implementation to increase the throughput in the third dimension:

Delivering clock to each die and dealing with clock synchronization is a critical problem in the design of the 3D integrated circuits mainly due to die-to-die variability which can lead to some supplementary timing margins at design-time. Globally Asynchronous Locally Synchronous (GALS) systems are used for dealing with this issue. NoC offers a structured solution to construct GALS architectures. Since a NoC spans the entire chip, the network can be the globally asynchronous part of the system, while the subsystem modules (IP blocks) are the locally synchronous parts.

For 3D technologies, a structured interconnect such as a 3D NoC using a GALS scheme will benefit from the third dimension and will bring a scalable and modular communication infrastructure which can be easily exploited. This represents a natural architecture evolution for MAGALI chip. The existing NoC could easily be extended to support additional 3D router for vertical connections between dies. Figure 25 is showing a 3D capable architecture for MAGALI SoC. The 2D mesh Network-on-Chip has been extended for adding four 3D routers. Each of them will be capable of transferring data among the vertical dies as depicted in Figure 24.

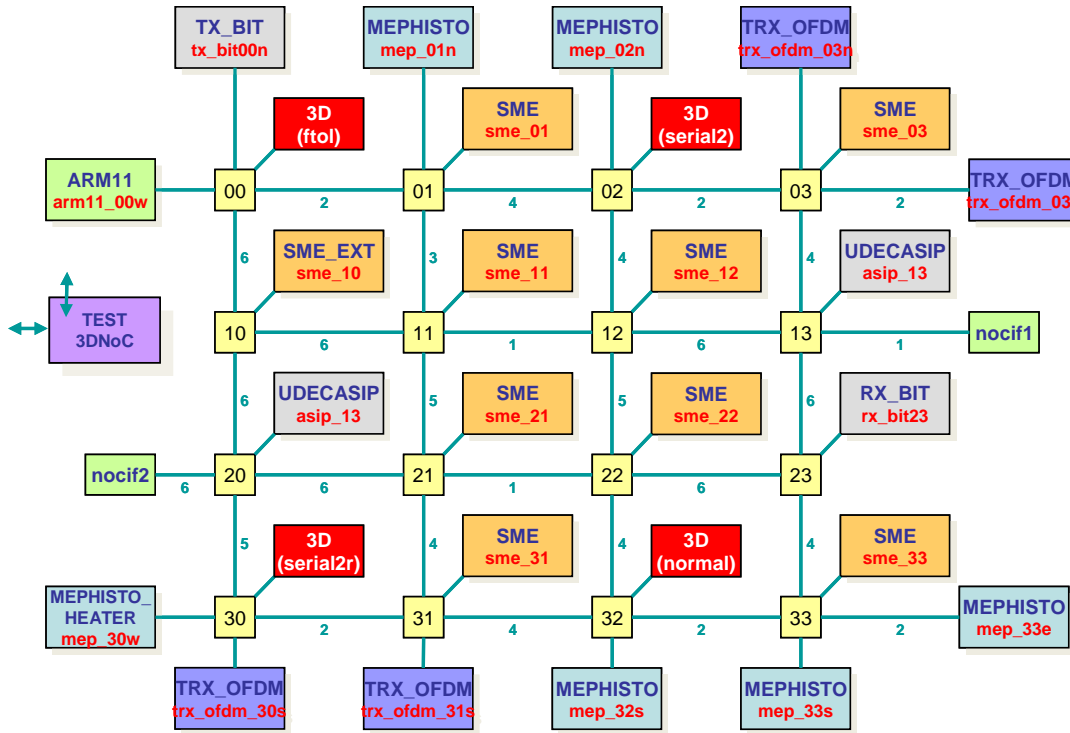


Figure 25: 3D capable MAGALI extended architecture

The complete system should consist of a 3D Integrated circuit made of several 3D MAGALI SoCs as shown in Figure 26.

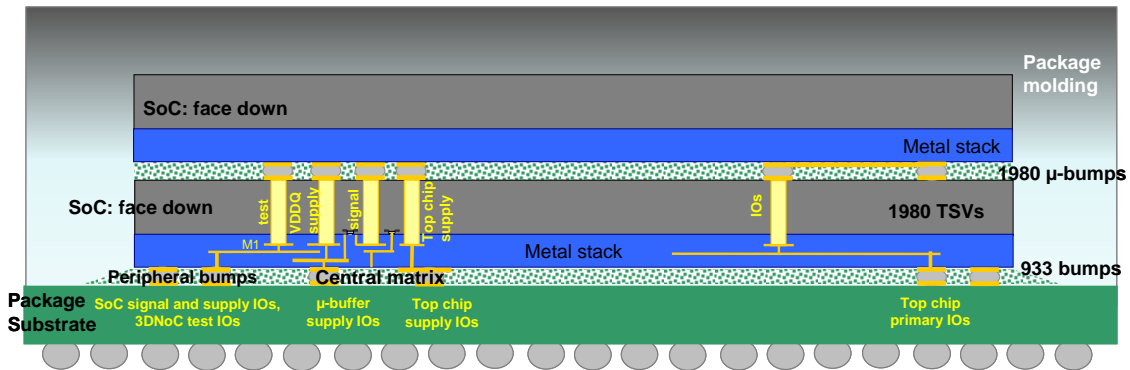


Figure 26: 3D Integrated Circuit with 3D capable MAGALI SoC

This 3D-IC is a 2 layer stack with two identical processor SoCs assemble together with the technological assumptions summarized in Table 4.

Table 4: 3D integration technology assumptions

<b>Assembly</b>	Die to die
<b>Stacking</b>	Face to back
<b>TSV process</b>	Via Middle
<b>TSV density</b>	10μm diameter
<b>TSV xy pitch</b>	50μm x 40 μm
<b>Copper Pillars</b>	25μm diameter

The 3D-IC is packaged with a flip-chip technology to improve the power integrity and consequently allows high performance operating conditions. The second MAGALI is stacked on top of the first one in a Face-to-Back configuration. The interconnect, located in the centre area

of the dies, consists in an array of 2000 micro-bumps whose pitch is in the range of 40 $\mu$ m to 50 $\mu$ m. With such a configuration, TSV are required within the processor SoC. Some of them are dedicated to the top die supply distribution from the package balls. The other TSVs are used for the 3D NoC interconnect signals.

This new chip based on MAGALI and integrating the 3D stacking concepts has been already designed. Its fabrication is scheduled for end of 2012. This new MAGALI version will achieve more than twice the performances at a relatively low cost.

### 3.3.6 Conclusion

In this study we have first shown that when no specific method (cooperation, relaying, interference mitigation...) is used, a UE near the cell edge experiences interference that dramatically damages its performance. We then introduced cooperation between adjacent cells thanks to the Double Alamouti decoder at the UE side. We have shown, from simulations, that this method allows cell edge users to reach good performance.

An important feature of ARTIST4G project is that simulation studies of innovations are accompanied by lab trials. For this purpose, the CEA hardware platform based on MAGALI SoC has been used for the implementation of DL CoMP Joint Processing without CSI feedback. This implementation filled two objectives: the first one was to enable specific measurements in terms of hardware complexity and power consumption related to the new algorithms implemented on the MAGALI ASIC. These figures of merits were indeed relevant inputs for WP1 since double Alamouti scheme was also studied within WP1 for the uplink scenario. The second objective for lab trials was to validate the theoretical results obtained by simulations. Benefits of CoMP in terms of coverage and cell edge throughput were investigated by considering real world conditions through lab trials.

The first objective has been reached thanks to the implementation complexity figures and power consumption figures measured on complex and representative algorithms as the 4x2 downlink receiver. It showed that next generation of LTE technology would increase drastically the hardware complexity linked to more complex MIMO schemes. This will require PHY layer hardware architecture evolution while keeping flexibility and low power consumption especially needed for the UE baseband SoC. Several design technology evolutions have been discussed and CEA chose the 3D-integration technologies which make the stacking of multiple instances of the same baseband chip possible to boost the overall system performance and address more complex MIMO schemes. On the embedded software side, MAGALI has been designed taking into account a programming model common to all the heterogeneous units. Here, the objective is to hide the heterogeneity between components by proposing a common communication model. It will open the door to the development of tools in order to facilitate application mapping on the hardware platform. For ARTIST4G, the tool was not ready and lots of effort has been put on the application mapping. This tool dedicated to communication compilation is now under development and will allow a large gain in time in the development and mapping of new applications on the MAGALI platform.

The second objective for lab trials has been achieved through the hardware implementation of a 4x2 downlink CoMP scenario under emulated channel conditions involving three MAGALI platforms organized around a 57-router Network-on-Chip that connects 87 telecom-oriented processing units. The control from a host PC combined with the flexibility of a reconfigurable hardware allows to dynamically configuring all the boards on the network synchronously. It permits the automation of measurements that require varying parameters of multiple processing operators. The 4x2 downlink CoMP emulator is under its final step of system integration. All PHY processing sub-systems (RX 4x2, TX 2x2 and channel emulator) have been implemented and tested separately. The first measurement results have been obtained with the bit-accurate functional model for the interference scenario and show a good correlation with the floating point software simulations. It assesses the hardware mapping methodology and the parameter set. The real-time processing of the MAGALI board and the test automation allowed by the host PC will provide an efficient hardware emulator for validating complex cooperation scenarios required to improve the cell-edge throughput performances.

### 3.4 Uplink CoMP

CoMP is one of the main concepts that is investigated in ARTIST4G. It has been shown in various previous publications that cooperation among base stations can improve spectral efficiency, particularly at cell edges. Looking at the state of the art, in particular [6] and [12], it's arguable that the problem is well understood in theory. However, the application of CoMP in practical deployments issues multiple challenges, some of which are very difficult to model in simulation studies. Prominent examples are the required synchronization of all cooperating entities in time and frequency [13], multi-cell channel estimation and the effect of channel estimation errors [12], and backhaul-efficient multi-cell signal processing [14]. Even though significant progress has been made, the often isolated examination of certain problems is not sufficient to prove the maturity of ambitious CoMP concepts, and accurate models for system level simulations still need to be found and validated.

The work presented in this section was done in close cooperation with WP2. The theoretical foundations for many signal processing algorithms that are used herein were for example presented in Chapter 2 of D2.1 and Chapter 5 of D2.2. Field trials on different topics of uplink CoMP were done throughout the project. Certainly, even though a wide range of topics was touched in the course of ARTIST4G, there was the need to focus on several aspects that were considered to be of highest interest and also suitable to be investigated by field trial measurements. These topics were:

- System configuration and setup, in particular
  - Number of antennas per BS ([15], D6.2 Section 3.3.4.1)
  - Cooperation cluster size (e.g. [24])
  - BS antenna downtilt ([19], D6.2 Section 3.3.4.3)
  - Number of Tx streams on the same resources (Section 3.4.5 below)
- Signal processing algorithms, in particular
  - Linear and non-linear receiver algorithms (e.g. [15], [28])
  - Signal processing for reduction of backhaul requirements
    - Exchanged of decoded information for distributed successive interference cancellation (D-SIC) (e.g. [15] and Section 2.3 of D2.1)
    - Compression of received BS signals in the time and frequency domain ([26], [25], Section 3.3.4.2 in D6.2, Section 2.3 of D2.1, Section 5.1 of D2.2)
    - Comparisson of intra and inter-site uplink CoMP ([27], Section 3.4.3 below)
  - Investigation of time synchronization, time delay of arrival, and algorithms to mitigate the impact of synchronization errors ([13], [27], Section 3.4.3 below)
- Comparison of field trials with simulation models (Section 3.4.4 below)
- Specific applications scenarios
  - Uplink CoMP for moving relays (Section 3.4.5 below)

This list includes references to available publications that were written based on the field trial results. A first set of results was presented in D6.2, other will be summarized later in this section.

#### 3.4.1 LTE-Advanced Testbed

The LTE-Advanced testbed is depicted in Figure 27. It is located in downtown Dresden, a representative area of a medium-sized European city. It was built in the German government funded project started EASY-C and started operating in April 2008. Since then it was constantly used in various EU projects, particularly ARTIST4G.

The testbed is located in an area with a typical urban building morphology that is characterized by large apartments of 20 – 50 m height, a soccer stadium, a train station, railway tracts and roads with up to 4 lanes. Since it covers surroundings of very different building morphology, various propagation conditions can be tested which are of special interest for evaluation of fourth-generation (4G) systems. This includes interference conditions that are typical in frequency reuse one networks like LTE which is very beneficial for the development of advanced algorithms such as cooperative MIMO.

In total different 19 BSs located on seven sites with up to three-fold sectorization are used for the measurements. Detailed information on the site layout can be found in Table 11. Each BS is equipped with a two element, cross-polarized KATHREIN 80010541/29 antenna which has 58/80° horizontal and 6.1°/7.5° vertical half power beam width. The angle between the boresight of antennas that belong to different BS at one site is  $\geq 120^\circ$ . The basic physical layer procedures are used in close compliance with the 3GPP/LTE standard (see e.g.[17]). This concerns mainly the the control and data processing. However, as a major difference, we use OFDM instead of SC-FDMA in the uplink as well. Time and frequency synchronization of BS, which is required for joint detection, is done through GPS fed reference normals. Other general transmission and testbed parameters are stated in Table 5.

In the course of ARTIST4G, multiple field trials have been done in the testbed using different UE configurations (number of UEs, antenna types, UE locations, etc.), but also using different BS setups which mostly included only a subset of the overall BSs. We will present further information on each particular setup in the following sections. Generally, multiple UEs were moved on a measurement bus or on bicycle rikshaws (see Figure 9) while transmitting on the same time and frequency resources employing one dipole antenna each. In order to achieve robust communication and large throughput at the same time, the transmitter should adapt modulation and coding to the channel conditions. Unfortunately, this is not possible for offline evaluation. To determine achievable transmission rates for each channel, the UEs are configured to use the same modulation and coding scheme (MCS), whereas the MCS is switched in a fast sequence. Thus, within the channel coherence time, different transmission rates can be tested. There is the additional option to switch of particular UEs on a ms basis. This was used in the moving relay field trial in Section 3.4.5 below in order to test the transmission of a different number of transmit streams for the same channel realisation. While this approach leads to reasonable results, and has the particular benefit that different Tx and Rx configurations are compared for the same measurement data resp. channels, the field trial is subject to the following assumptions and limitations:

- HARQ is not considered (but also not necessary because emulated perfect rate adaptation is possible using offline signal processing).
- No background interference has been considered and, thus, no interference floor is visible.
- No power control is used which emphasizes the benefit of SIC because the sum capacity of the multiple access channel is achieved at full transmit power of all streams.

**Table 5: Overview of testbed and transmission parameters**

BS distance	450 - 1200 m
BS antenna height	30 - 55 m
Uplink carrier frequency	2.53 GHz
System bandwidth	20 MHz
Sub-carriers per PRB	12
UE transmit power	max 18 dBm
Quantization resolution	12 bit per real dim.

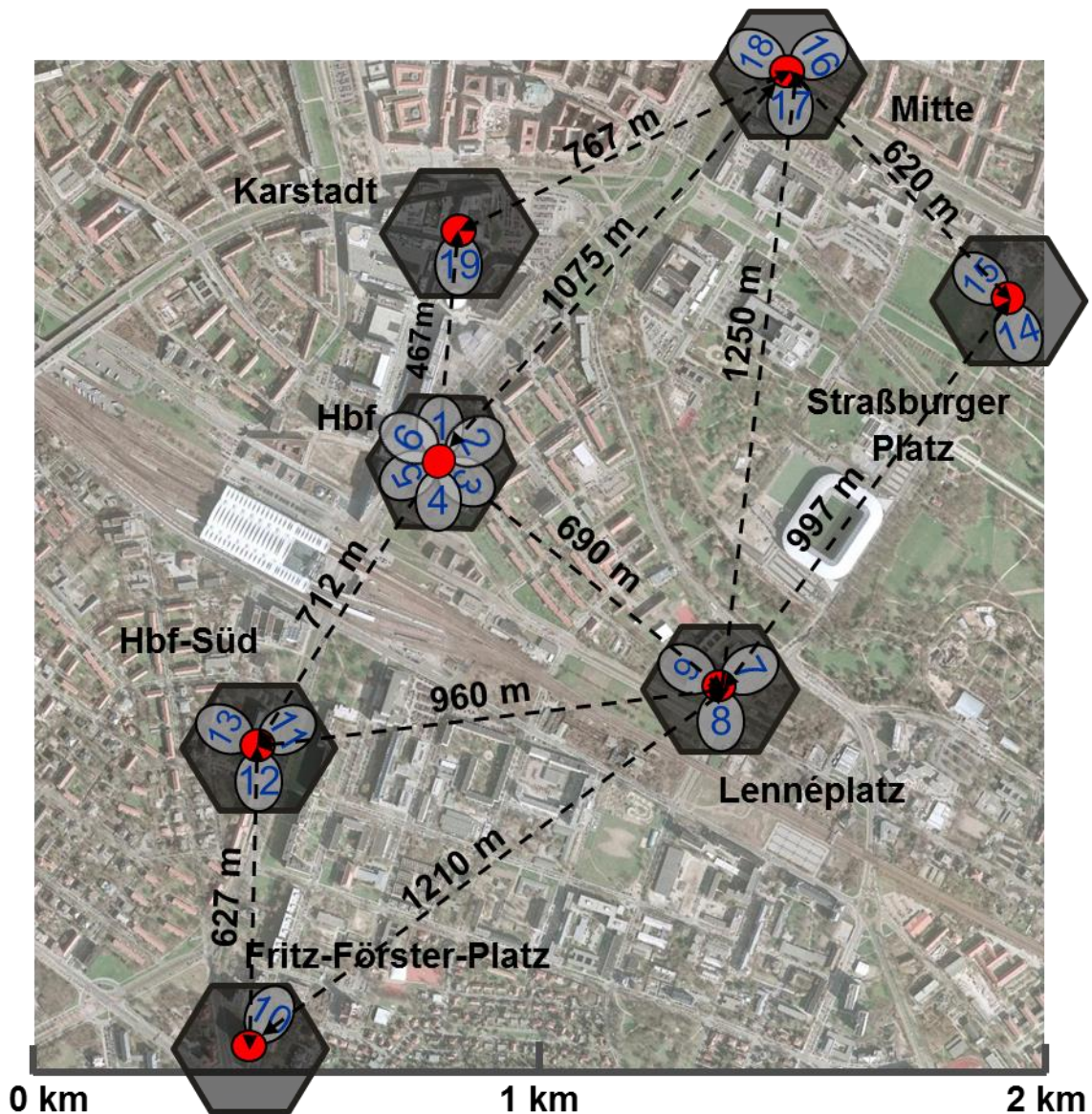


Figure 27: Complete testbed setup

### 3.4.2 Base Station Signal Processing

The general BS offline signal processing includes

- OFDM symbol timing and frequency synchronization
- demapping of reference and data symbols
- channel estimation
- noise variance estimation
- symbol equalization
- QAM symbol demapping and decoding

For a detailed discussion of these steps, we refer the reader to Section 3.4.3 of D6.1 [20]. However, various aspects of the signal processing were extended during the project in order to investigate particular research questions. In particular, we address time domain channel parameters, like symbol timing offset (STO) and time delay of arrival (TDOA), in Section 3.4.3. Whenever additional signal processing is required, it will be discussed in these sections.

### 3.4.3 Comparison of Intra and Inter Site CoMP

#### 3.4.3.1 Introduction

Previous field trial results in [1] show for the uplink that inter-site JD is feasible. However, one major problem that comes up in this case is the requirement of UE timing synchronization in the whole cooperation cluster (e.g. the propagation delays in an LTE system should not exceed the cyclic prefix in order to avoid ISI) which degrades cooperation performance. Furthermore, the use of JD across different sites could require a costly upgrade of the backhaul network, a requirement that could be relaxed when the exchanged receive signals would be compressed, as previous theoretical and field trial publications show [14] [section]. It should be clear that these problems are easier to deal with when only BS at the same site cooperate, referred to as intra-site CoMP. We evaluate in this section by how much the performance is impaired using such a constrained set of cooperation BSs.

The performance of intra-site CoMP certainly depends on the site deployment, mostly the number of BS (or cells) per site and their location on the roof or radio mast and the antenna patterns (beamwidth). In general, intra-site CoMP only covers a subset of cell borders. It is, thus, expected that the performance of CoMP can be improved when cooperation clusters can be formed across sites, so called inter-site CoMP.

In this section, we provide a summary of the comparison of intra and inter-site JD that is based on field measurements in an urban test bed. We not only address potential gains but also various challenges of both schemes. Details especially on the signal processing algorithms used can be found in [27].

#### 3.4.3.2 Receive Signal Processing

Within the described testbed we use an offline data evaluation approach that allows us to apply various receive signal processing algorithms on the same recorded data. The general receiver signal processing steps were described in [15] which includes symbol estimation and decoding. Algorithms for the estimation of significant channel parameters that affects the performance of intra and inter-site cooperation are presented in [27]. These parameters propagation delays  $\tau_d$  and delay spread as well as the channel gains are of particular interest because they are influenced by the different geometries of the transmission links. The algorithms are applicable to the 3GPP/LTE physical layer since they are based on compliant control signaling.

#### 3.4.3.3 Field Trial Results

In this section, we compare the performance of intra and inter-site CoMP in an uplink field trial using the setup of 16 BSs described in Section 3.4.3.7 of D6.1 [20]. The route traversed by the measurement car, traveling at a speed of about 6 km/h, is depicted in Figure 28 of D.6.1. It has a total length of about 17 km and passes through surroundings of very different building morphology. While the UE were continuously transmitting, the received signals of the BS were stored for a duration of 80 ms (80 TTI) every 10 s giving a total set  $\mathcal{L}$  of 885 measurements. In the following we use the index  $l$  to refer to a certain measurement.

The goal of this section is to analyze the properties of intra and inter-site cooperation in a practical setup. While the general receive signal processing steps do not differ between both approaches, different coupling characteristics of the spatial transmission channel (in particular received power or SNR and interference levels and propagation delays) occur due to the different locations of the sites.

In the measured (sum)  $SNR_l^m$  values observed at all BSs with BS (index  $m$ ) and locations (index  $l$ ) are shown. The two largest SNRs measured at any BS for each measurement are depicted in the upper part of the figure. An interesting result is that rather *balanced* SNR values for two different BSs are observed at each location of the UE. Since the joint signal processing is particularly beneficial in balanced coupling scenarios this result indicates that cooperation among base stations could be exploited throughout the measurement route. Furthermore, assuming that cooperation clusters were formed at the BS with the highest  $SNR^m$  (the sum power of the received signals vs. noise) and a cooperation cluster size of  $C = 2$ , the upper row depicts whether this cluster was intra-site (which was the case in about 30 % of the measurements). It should be noted that the BS antenna downtilt has a great impact

on these results. In this field trial, a constant downtilt of  $6^\circ$  was applied at all BS. Field trial results for different downtilts in the same testbed are reported in [19].

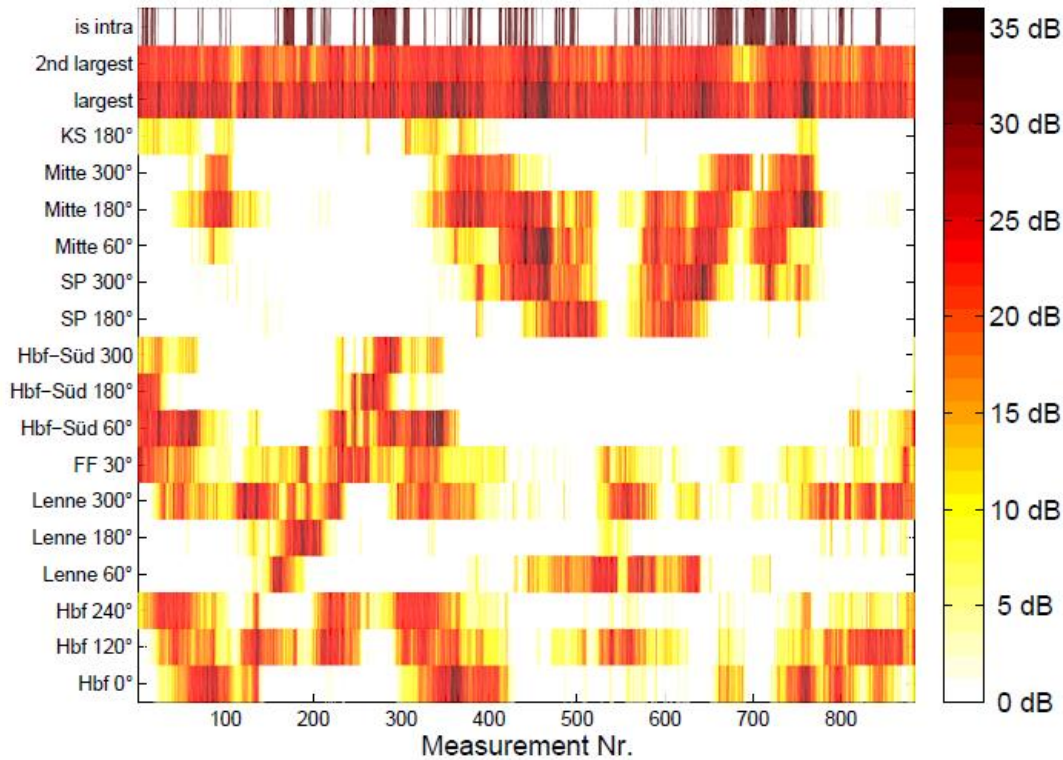


**Figure 28: Sum  $SNR^m$  achieved at all BS of the test bed during the complete field trial**

In the following, we evaluate the per UE  $SNR^{m,k}$  levels that were observed at multiple BS during the field trial in more detail. In particular, we investigate the CDF of the minimum  $SNR_{min,l}^k$  that was simultaneously measured at  $M_C$  BS. This CDF is plotted in Figure 3 for  $M_C = 1..7$ . As one can see, in 50% of the measurement positions an  $SNR^k$  of more than  $\approx 18$ dB is seen at one BS while two BSs individually observe (at least) this SNR only in 20% of the scenarios. This is also an intuitive behavior since the different distances between one UE and several BSs lead to varying pathloss values on the links. We observe from this plot that the  $SNR^k$  measured at the strongest, second strongest, ... BS differs by about 3 dB in this field trial, a value which again depends on the antenna downtilt [19].

In order to investigate this aspect in the context of intra and inter-site cooperation, we concentrated on two different sites, referred to as Hbf and Hbf-Süd (see Figure 27). Site Hbf is located in the center of the testbed and has three sectors which are mounted at different edges of the rooftop. Thus, the UE will typically only have LOS to one (or less) of the antennas. Instead, at site Hbf-Süd, all antennas are mounted on the same radio mast. Further information on the BS at these two sites can be found in Table 5.

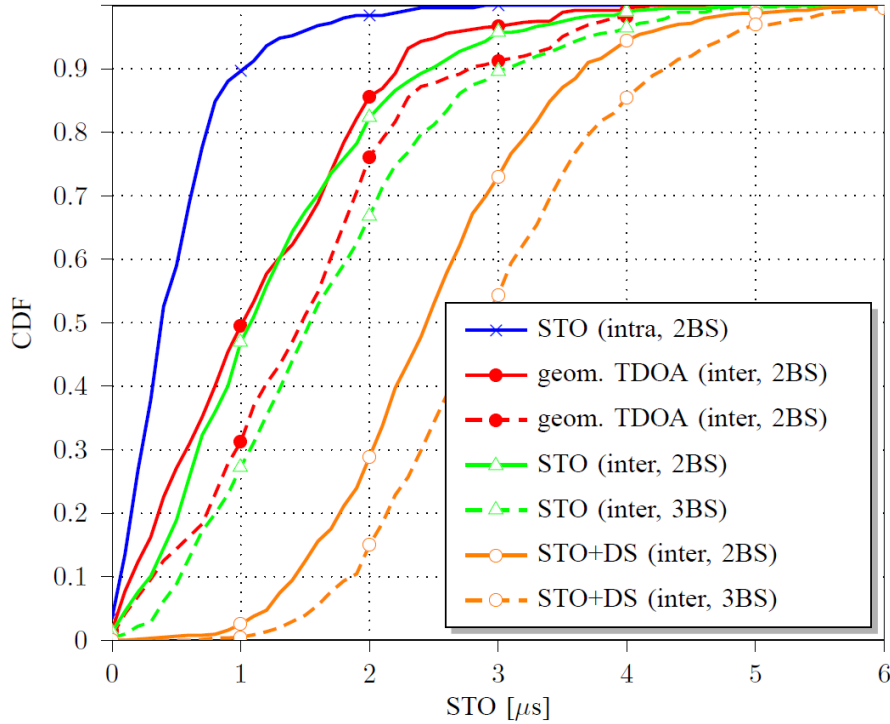


**Figure 29: CDF of measured symbol timing offsets (STOs) as well as STOs + delay spread (DS)**

For each UE, we looked individually at the subsets of those measurements, where it had the best  $SNR^{m,k}$  (SNR of UE  $k$  at BS  $m$ ) at one of the BS at Hbf  $\mathcal{L}_{\text{Hbf},k} = \{l \mid \arg \max_m (SNR_l^{m,k}) \in \{1,2,3\}\}$  (399 UE locations in total). The CDF of this SNR is the blue curve in Figure 30b)<sup>1</sup>. The other solid curves indicate the SNR of the second and third largest SNR that was measured instantaneously at any other BS while the dashed curves indicate the SNR that was measured at the other BS of Hbf. Clearly, we see a great advantage of inter-site CoMP due to the directive antennas which lead to a high separation of intra-site BS and the greater diversity of potential BS in the cooperation cluster. Figure 30c) shows the same result for site Hbf-Süd ( $\mathcal{L}_{\text{Hbf-Süd},k} = \{l \mid \arg \max_m (SNR_l^{m,k}) \in \{8,9,10\}\}$ ), where one of the BS of this site had the highest  $SNR^k$  at 215 UE locations. Interestingly, the results in terms of intra-site CoMP SNR are rather similar even though the deployment at both sites is very different. Thus, it can be expected that the antenna pattern and the sectorization (same at both sites) have a larger influence on the intra-site CoMP performance than the location of these antennas on a rooftop. This aspect should be further evaluated in other field trials. Another interesting aspect is that a cluster size of three does not seem to be very beneficial for intra-site CoMP because the SNR at the strongest BS is much larger than the SNR of the third strongest BS.

<sup>1</sup>We do not distinguish between the UE in this and all following curves, i.e. stacked the values of both UEs in one vector and drew the CDF of this vector.

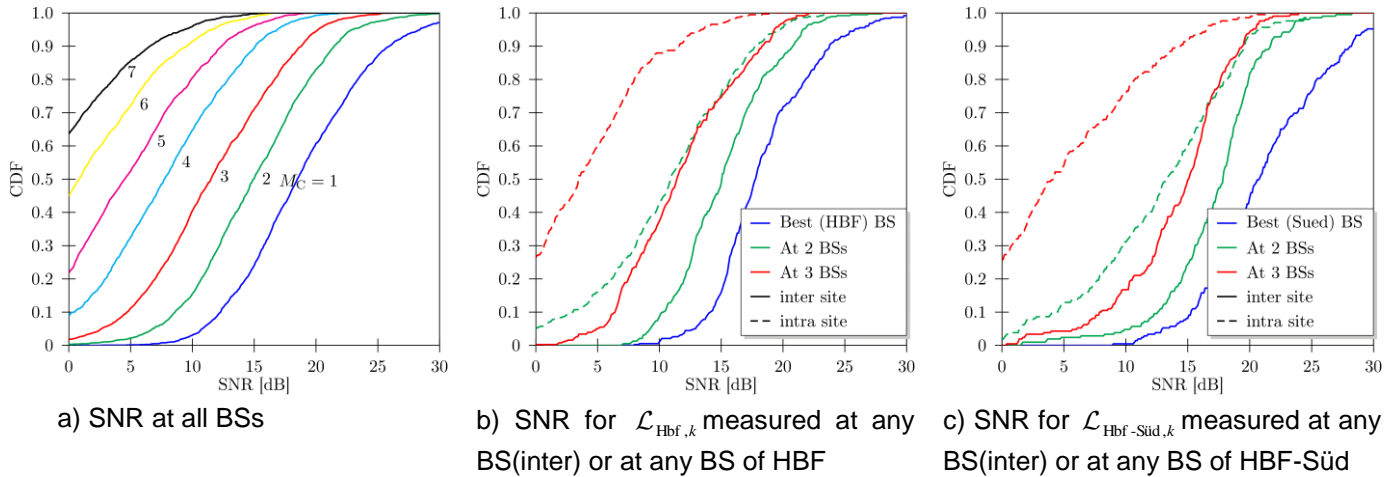


**Figure 30: CDF of SNR that is instantaneously achieved at multiple BSs.**

While the UEs should be able to align their timing to all BS of an intra-site cluster using conventional LTE timing advance, this is not possible if the cooperation cluster are formed across sites. Thus, larger STO are expected for inter-site CoMP. It should be noted that the maximum delay should be within the cyclic prefix of  $4.7\mu\text{s}$  in order to avoid ISI. The CDF of the occurring STO observed in the field trial for cooperation clusters of two or three BS are shown in Figure 29. As a reference, the geometrical TDOA, the difference in propagation time to all BS in the cooperation cluster assuming LOS, is included as well (red curves). As expected, the STOs for intra-site cooperation (blue curve) are much lower than for inter-site cooperation (green curve). Furthermore, the results indicate that during the measurements a large percentage of the STOs are within the CP so that no ISI occurred even for three cooperating BS. The magenta curves show the total channel length including STOs and delay spread for inter-site cooperation. Even in this case ISI can be avoided.

As a final investigation, we were interested in transmission rates, which were determined in the offline evaluation as follows: the UE changed their MCS every 5 ms, looping cyclically through 8 MCSs given with rates between 0.375 (4QAM) and 5.25 (64QAM). For each such loop, the maximum achievable rate (MCS) is determined (averaged over 10 TTI per MCS) --- based on the assumption of a constant channel for at least the duration of one loop --- emulating a perfect rate adaptation. The achieved rate is denoted as  $r_{k,l}$  for UE  $k$  and location  $l$ . The CDF of these rates for different intra and inter-site scenarios is plotted in Fig. 5. In Fig. 5a, we focused at the set of measurements where highest sum received power was observed at any BS of Hbf:  $\mathcal{L}_{\text{Hbf}} = \{l | \arg \max_m (\text{SNR}_l^m) \in \{1,2,3\}\}$ . Only a single antenna per BS was evaluated. Compared to conventional detection of UE at individual BS, the transmission rates could be significantly increased using JD. Compared to this baseline, intra-site CoMP gave certain gains which were increased when inter-site JD was. In particular, we see that an increase of the cluster size from two to three BS was very beneficial in the case of inter-site CoMP while the gains of a larger cluster size was much smaller, but not negligible, for intra-site JD.

The same is basically true for a setup with two antennas per BS. However, in this case the performance gains of JD are smaller in general because spatial separation of UE signals is already possible at a single BS improving the performance of conventional detection. It should be noted, however, that the additional spatial degrees of freedom of JD could be used for spatial multiplexing of a larger number of UE or suppression of outer cluster interference. We plan to investigate both options in future field trial campaigns.

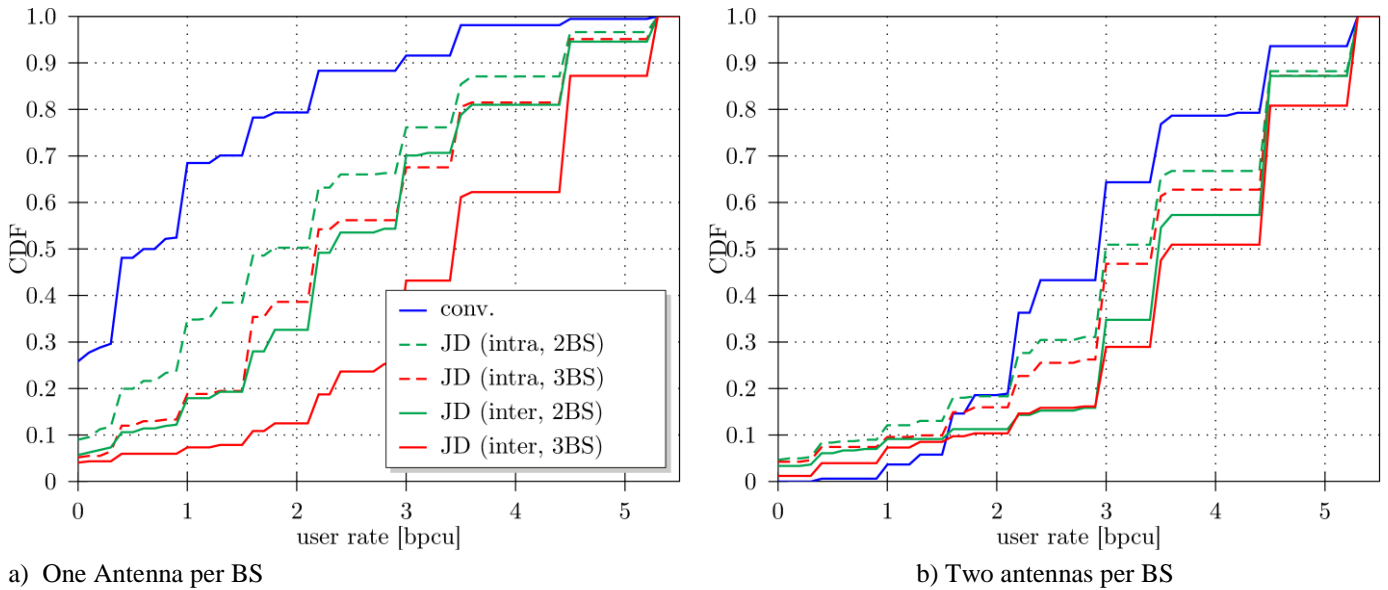


**Figure 31: CDF of UE rates for all measurement locations in  $\mathcal{L}_{\text{Hbf}}$**

### 3.4.4 Field Trial vs. Simulation

In order to provide the opportunity to recapitulate the measured results of the field trials, we compare them to popular simulation models in this section. In this comparison, we use the locations of the BSs and UEs during the field trials to form the basic structure of the underlying cellular network instead of applying a regular grid with uniformly distributed users. For calculating the required large and small scale fading coefficients the channel model described in [31]. All other parameters are used as given in the 3GPP document.

**Table 6: Network Parameters for Simulation Models**

Average building height	10 m
Average BS height	40 m
Average street width	20 m
Variance of shadow fading LOS/NLOS	6 dB / 8 dB
PL model	Suburban Macro
Vertical antenna pattern	6° downtilt, 6° HPBW, 15dB side lobe attenuation
Horizontal antenna pattern	60° HPBW, 40dB frontback ratio

As a basic illustration of the coverage achieved with the network configuration given by the testbed in Figure 32 the achievable maximum link SNRs (of the best BS) over the entire cell area are depicted. We used the same field trial using the setup of 16 BSs described in Section 3.4.3.7 of D6.1 [20]. The boresight directions are indicated by the black arrows. Furthermore, the UE positions of the field trial are indicated by the white crosses. The particular GPS coordinates of the base station and user positions are available by the authors (Contact: Michael Grieger).

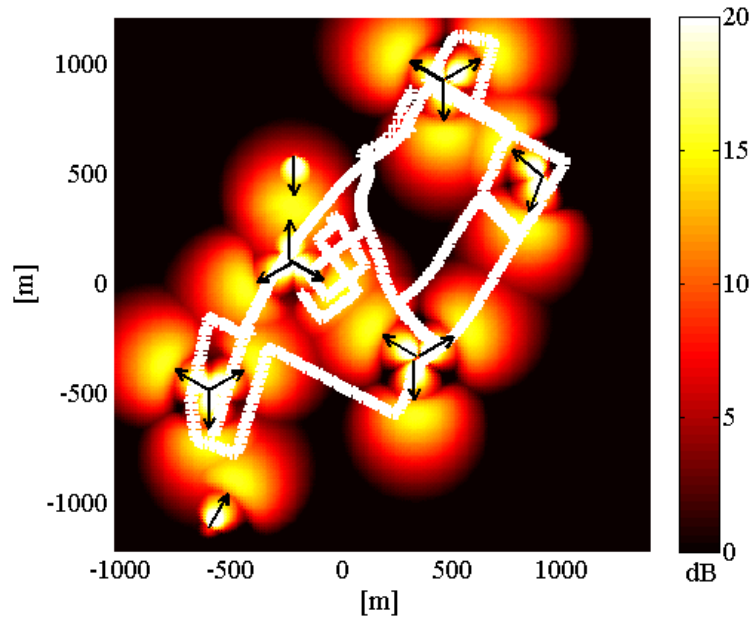


**Figure 32: Simulated Coverage of the Testbed Dresden**

First of all, the occurring link SNRs are compared when using the simulation model with random shadowing and an LOS/NLOS probability. As reference for the measurements the observed link SNR values of Section 3.4.3 are used. On the right-hand side of Figure 33 the simulated link SNRs are shown.

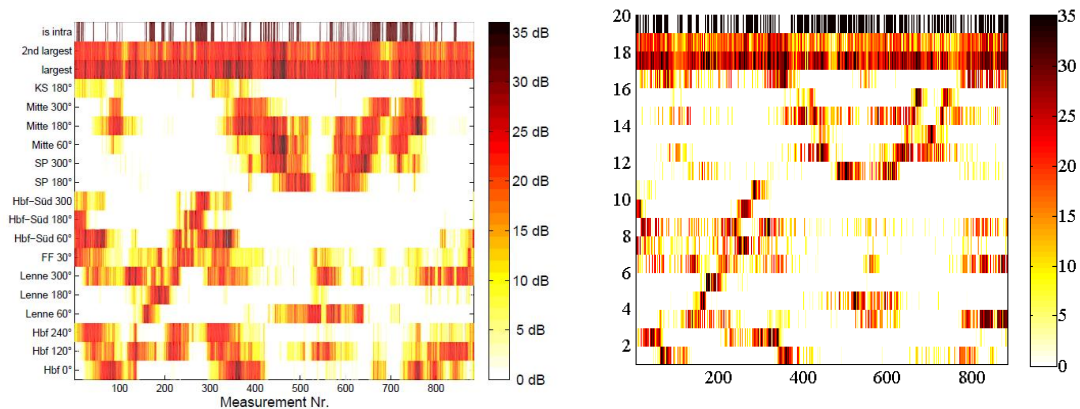


**Figure 33: Comparison of Occurring link SNR over Coverage Area (left – Measurement, right - Simulation)**

As one can observe, with this parameter set a good match of the achieved link SNR values can be achieved compared to the measured ones which are depicted on the left-hand side of the figure. It should be noted that the simulated link SNRs represent only one snapshot of a random experiment but similar SNR distributions can be achieved in every snapshot. Within the simulation also the stronger effect of the random pathloss can be seen. This leads to the behaviour that at neighbouring measurement locations often strong differences of the SNR levels can be observed. In the measurements this effect is visible as well but much less pronounced. The average probability of inter-site cooperation was approximately 65% which is also comparable to the measurements (note that a black marker in the right figure indicates inter-site cooperation, while it indicates intra-site cooperation in the left figure). As the pathloss attenuations mainly depend on the distance between the BSs and the user terminals in Figure 34 the occurring SNR distribution of the simulation and the measurements are compared.

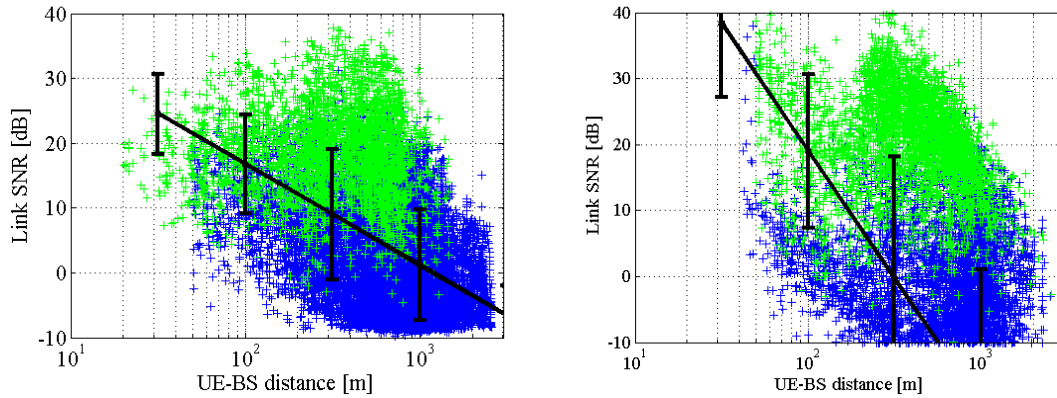


**Figure 34: Distribution of Link SNRs with respect to the Distance between BS and UEs (left – Measurement, right - Simulation)**

An important metric to compare the measurements and the simulation is the slope of the linear regression line as well as the variance of the SNRs distributed around this mean value. While the linear regression is comparable to the pathloss exponent with the variance one can draw conclusions about the observed shadow fading. From the measurements a value average value of 8 dB shadow fading variance can be derived. The average linear slope can be approximated with 1.5. When using these parameters in simulations one can clearly see the similarities between both figures. Particularly a good match between the occurring SNR with the distances can be observed. While the blue points depict the SNRs between all BSs and all UEs the green point represent the SNR values used in the cooperation cluster.

As next, the occurring TDOAs are investigated. Therefore, Figure 29 is used as reference where the curve for the cooperation of only 2 BS is extracted. In Figure 35 the simulated and measured data are compared.

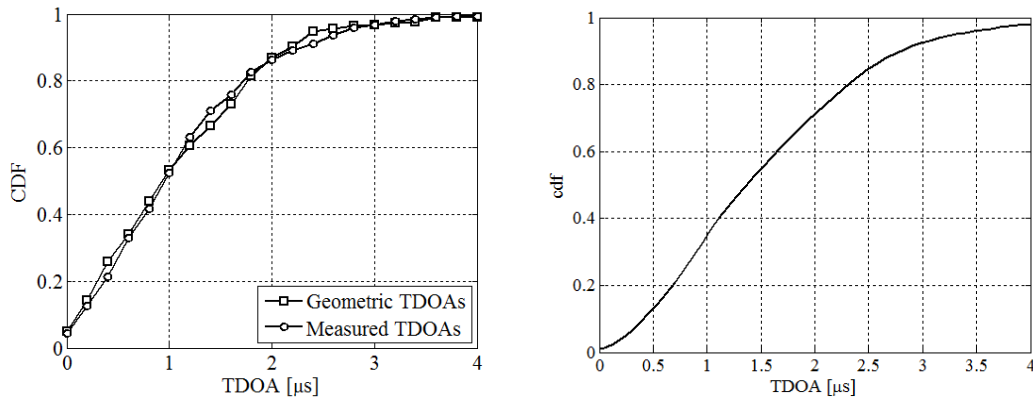


**Figure 35: Distribution of TDOAs in Measurements (left) and Simulation (right)**

On the right- hand side the CDF of the simulated TDOAs are shown which must be compared with curve ‘STO (inter 2BBS) of the left figure. As one can see, again a very good match of both curves is visible. This indicates the often the same BS are grouped into a cooperation cluster which lead to equal TDOAs.

### 3.4.5 Uplink CoMP for Moving Relays

Vehicles such as trams or buses constitute wireless communication hot-spots. In order to improve the connectivity of users on such vehicles, moving relay nodes could be placed inside. This way the users benefit from short distances and quasi-static channels. The access points connect to the cellular network via relay links using antennas mounted outside of the vehicle. These (moving) relay feeder links are the major bottlenecks of the transmission scheme. Thus, improving their performance and reliability is important to the success of the overall concept. Since vehicles provide sufficient space for placing multiple antennas, both measures could be improved using multi-antenna techniques which, potentially, allow for a linear increase of throughput with the number of antennas. However, these performance gains

can only be achieved entirely if the channels between the relay and the associated BS are uncorrelated, and the number of BS antennas is at least as large as the number of relay antennas. Both of these requirements will often not be met in practical systems. The number of antennas per BS is limited and they are placed in close vicinity, leading to correlated channel fading. Furthermore, it should be considered that spectral efficiency of today's cellular systems is often limited by inter-cell interference which was the main motivation to introduce CoMP techniques which were investigated widely in WP1 for the downlink and WP2 for the uplink. In the course of ARTIST4G, we have shown in various field trials (see e.g. the sections above) that uplink joint detection is feasible if certain requirements are fulfilled. In this section, we investigate the performance of uplink CoMP for a (moving) relay feeder, where the moving relay was transmitting up to four parallel data streams. In this, we compare different conventional and cooperative detection schemes. We also compare the performance of linear MMSE detection and the non-linear detection using SIC. However, moving relays are an interesting usecase for downlink MIMO as well. In this case, achieving accurate channel state information (CSI) at the transmitter is a big problem which can, potentially, be solved using a so called "Predictor" antenna concept which was investigated in WP3 and through field trials in WP6. For a summary of these results, we refer to Section 3.5.2 below and to [21].

#### 3.4.5.1 Measurement Setup

The measurement setup is similar than in previously described field trials. A total of 13 BSs was used and the transmitters were carried on a measurement bus. The measurement route is depicted in Figure 36. In total four UEs were involved. Since the transmit (Tx) antennas were mounted as a linear array in  $3\lambda$  mutual spacing, they can be considered as one moving relay transmitter (see Figure). However, we only considered the uplink direction of the feeder link. During the field trial,  $K$  out of maximum four transmit antennas were used at the same time using a set of different MCSs and transmitting on the same resources. Offline signal processing was used at the BSs. A couple of further field trial parameters are given in Table 7.

The field trial setup is suitable to investigate moving relay feeder link performance in a realistic moving relay environment. However, we do not touch problems that arise from mobility of the relay, such as handover and channel estimation/prediction which, in the uplink, are vital for link adaptation. In particular, very good rate adaptation of all schemes is important when SIC is used because errors of a stream early in the decoding order propagate because interference cannot be canceled as expected by the rate adaptation algorithm. The accuracy of rate adaptation depends on the accuracy of channel and interference information. Joint scheduling was investigated extensively in WP2. It has the potential to increase the control of interference. At the same time, it introduces delay because channel information has to be forwarded over the network. This delay, on the other hand, reduces the accuracy of channel information which out-dates quickly for mobile users. In ARTIST4G WP3 and WP6, a predictor antenna concept for developed for channel prediction for vehicles that travel at a constant velocity for the prediction horizon of a couple of ms (See Section 3.5.2 below and Part C of D3.5). The applicability of this concept was the main motivation to place the relay antennas on a line in the direction of travel in a moderate distance of  $3\lambda$ .

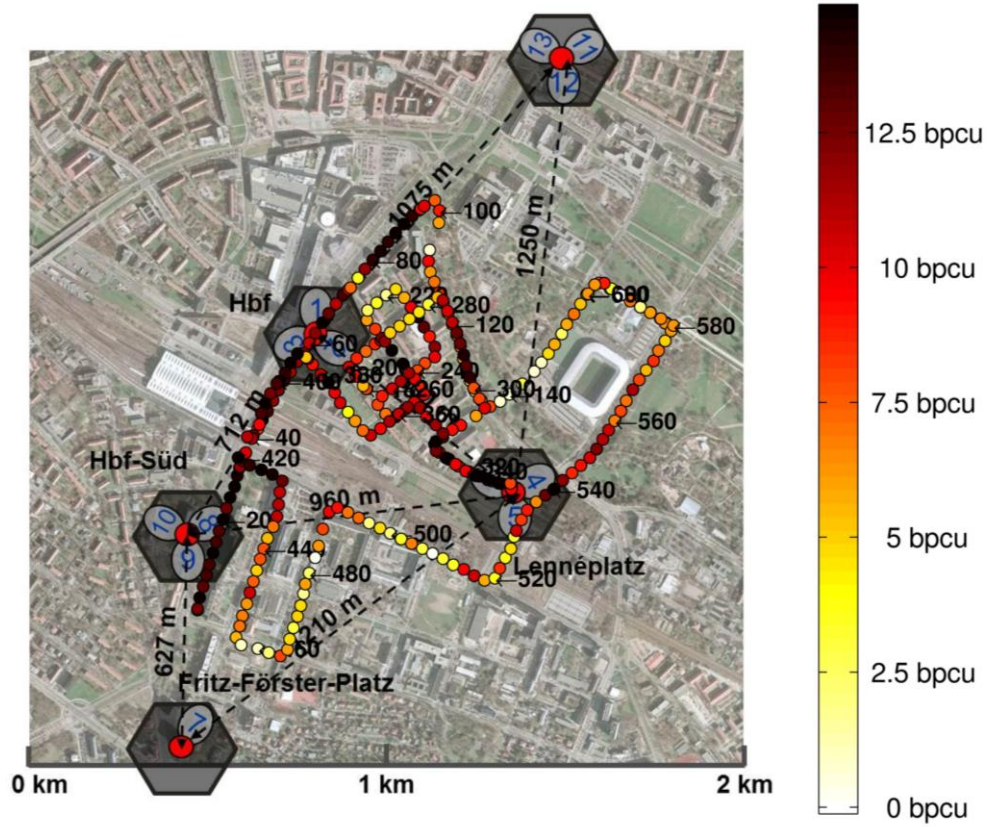


Figure 36: Testbed Deployment and JD+SIC ( $C = 3$ ) sum-rate of  $K = 4$  Tx streams at measurement locations. Map data ©Sandstein Neue Medien GmbH (<http://stadtplan.dresden.de>)

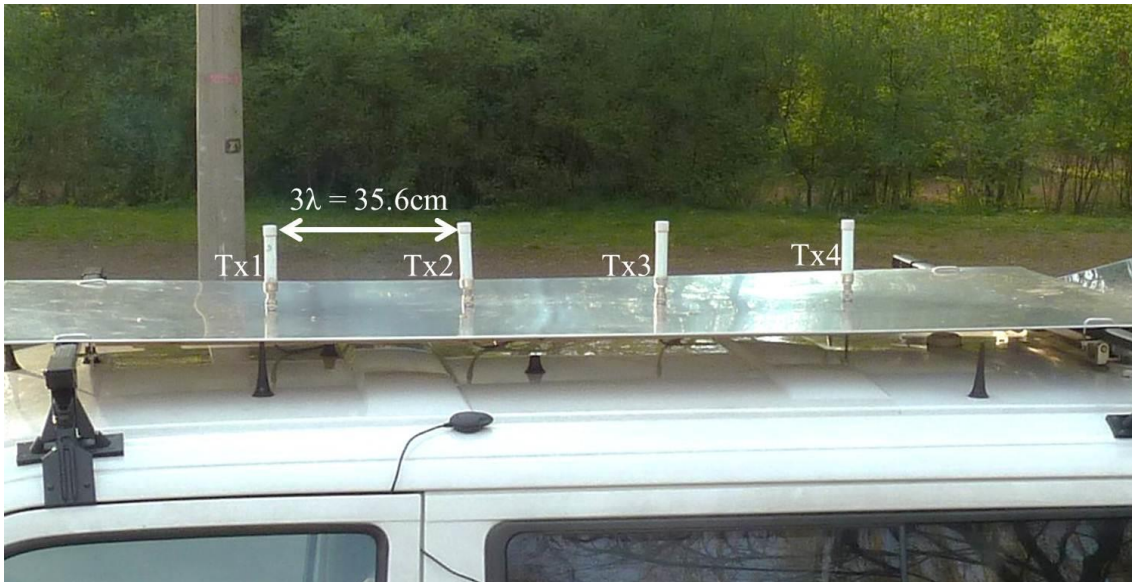


Figure 37: Configuration of moving relay antennas on measurement bus. Metal plate is used to get homogeneous ground plane below the antennas

### 3.4.5.2 Receiver Signal Processing

The basic signal processing steps were listed in Section 3.4.2 above. In the moving relay field trial, a couple of different detections schemes were compared:

- conventional (conv.) linear MMSE detection where different streams are potentially decoded at different BS.
- conv. non-linear detection of all streams at the same BS using SIC
- JD of all streams in a cooperation cluster of  $C$  BS potentially using linear MMSE filters or SIC

**Table 7: Parameters of moving relay field trial**

BS distance	500-1100 m (see Figure 36)
BS antenna height	30 - 55 m
Tx antenna distance	$3\lambda = 35.6$ cm
Tx antenna height	1.8 m
Carrier frequency	2.53 GHz
System bandwidth	20 MHz
Used PRBs	30 (5.4MHz)
Sub-carriers per PRB	12
per antenna data transmit power	8 dBm
Quantization resolution	12 bit per real dim.

#### 3.4.5.3 Results

The route traversed by the measurement car, traveling at a speed of about 6 km/h, is depicted in Figure 36. It passes through surroundings of very different building morphology. Measurements at the BS were taken synchronously every 10 s at a total of 600 measurement locations. The field trial was done in the uplink direction, with a moving relay transmitter and BS receivers. The moving relay was equipped with four antennas that were transmitting independent data streams. In order to test different transmitter configurations, the relay was configured to switch the number of Tx streams ( $K = 1,2,3,4$ ). The Tx streams were transmitted at neighboring antennas, such that the antenna distance for all stream combinations was always  $3\lambda$  (see Figure 37).

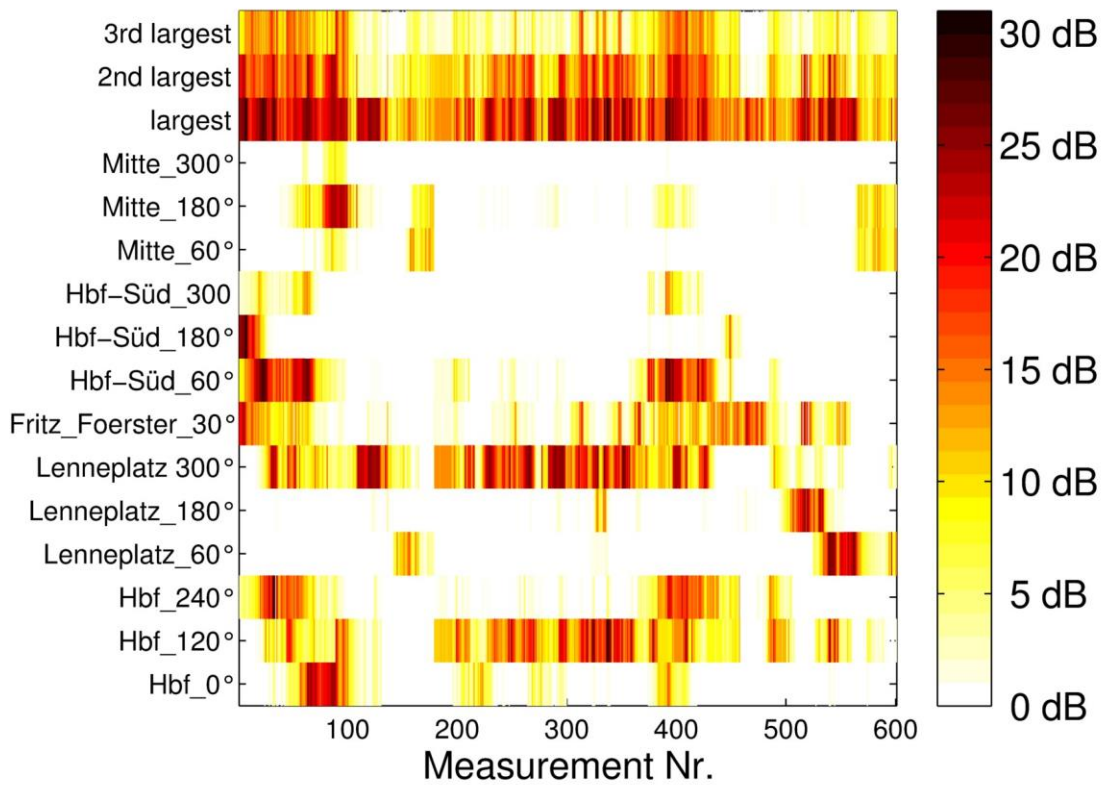


**Figure 38: Average per stream  $SNR_i$  achieved at all BSs of the test bed during the complete field trial**

As a first result, Figure 38 shows the average stream  $SNR_i$  measured at all 13 BS in the testbed. The figure also indicates the three largest  $SNR_i$  that was measured at any BS. We see that typically a good link to the moving relay was often established to multiple BS, while it was only seen by one or two BS at some locations. Good links to multiple BS are problematic in a conventional system with independent BS because the received power at all non-serving cells is interfering with potential other users. In a cooperative system, however, signal propagation across cell boarder is exploited by joint signal processing.

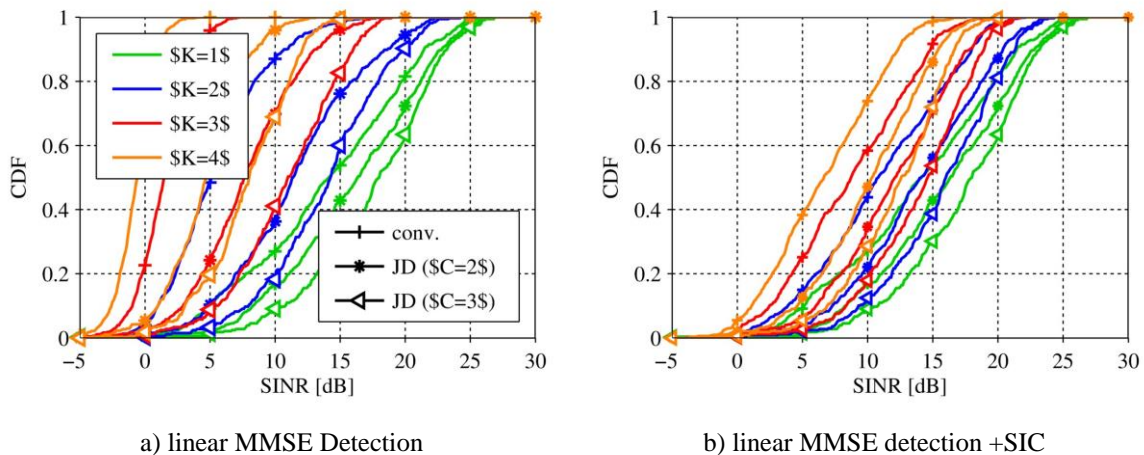


**Figure 39: SINR CDF for different number of Tx streams and receiver schemes.**

At each location the BS with the best SNRs were chosen for detection. In the conventional case one BS was detecting each particular streams while  $C$  strongest BS were forwarding their received signal to a joint decoder in the cooperative case. In order to assess the detection performance, we observe the CDF of SINR values measured after detection for

different transmitter and receiver configurations. Figure 39 a) shows the SINRs that were achieved by linear MMSE detection at a single BS (conv.) or by JD. The green curves are for single stream transmission ( $K = 1$ ). Since there is no inter-stream interference, the SINR values are largest for this transmitter configuration. Compared to conventional detection, JD gives an array gain because of maximum ratio combining of received signals through MMSE filtering. Increasing the number of Tx streams reduces the SINR for all receiver schemes. The decrease is most severely, however, for conventional detection. Even in the case of  $K = 2$  streams, the SINR for conventional detection is strongly reduced because the links between the two Tx and the two Rx antennas (of the BS) are highly correlated. Note that conventional receiver processing (as it is understood herein) includes the option that different streams are decoded at different BS which can be beneficial at the cell edge as a kind of soft handover. SINR values for JD degrade less severely because the MMSE filter makes use of the larger number of Rx streams that are less correlated. Figure 39 b) shows the SINR CDF for the same Tx and Rx configurations with the difference that inter-stream interference was canceled successively. For example, in the case of  $K = 2$  Tx streams, the stream with the highest measured  $SINR_i^*$  was detected first.

After detection we are interested in the throughput that was achieved throughout the field trial which is shown in Figure 40 for linear detection of a different numbers of streams. Looking at the performance of conventional detection first (green curves), we see that mostly (65% of the measurements) the transmission of a single data stream ( $K = 1$ ) achieved the highest rates, measured in bpcu (which is equivalent to bits/s/Hz if overhead is neglected). As listed in Table 8, 3.45 bpcu were achieved on average for this scheme. Switching between different number of transmit streams can be beneficial, e.g. between location 0 and 25, but would only provide small additional gains, mostly under very good channel conditions for which the rate of single stream transmission is limited by the limited choice of MCSs, allowing a maximum rate of 5.2 bpcu. Provided an optimal switching between different numbers of streams would be used (line named opt. Table 8), an average rate of 3.79 bpcu was achieved. Looking at the sum rate CDF in Figure 6 we arrive at the same conclusion. Increasing the number of streams even further is certainly detrimental as two Rx antennas per BS are not sufficient to spatially separate these streams, resulting in very low stream SINRs as already observed in Figure 39. For linear JD of  $C = 2$  BS, the transmission of  $K = 2$  or  $K = 3$  streams was typically the best choice. The average rate of 5.2 bpcu was the same in both cases. For an optimal selection of  $K$  at each location the average rate was 5.96 bpcu. The relative transmit time of each Tx stream number would have been 18%, 35%, 36%, and 10% for  $K = 1, 2, 3, 4$  respectively. For  $C = 3$ , the transmission of  $K = 3$  streams was optimal in 36% of the measurements and achieved the highest average rate of 6.10 bpcu. Optimal switching would have achieved 6.87 bpcu.

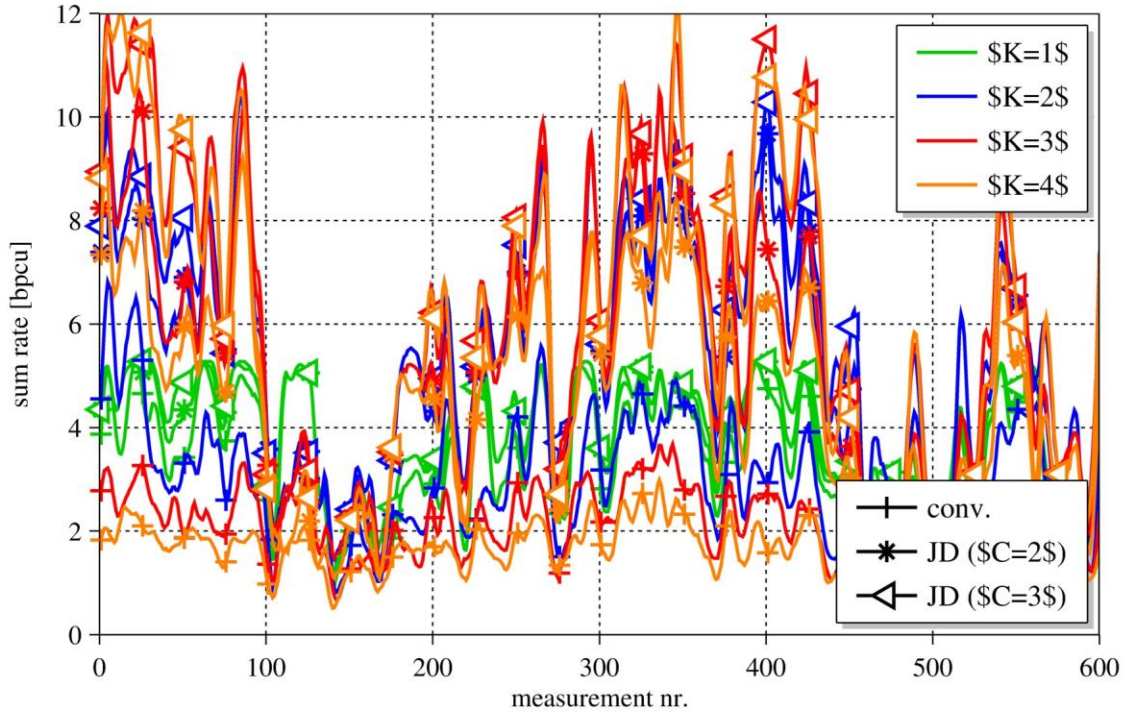


**Figure 40: Achieved rates for linear conventional and joint detection with cooperation cluster sizes  $C = 2$  and  $C = 3$  of  $K = 1, 2, 3, 4$  streams along the measurement route.**

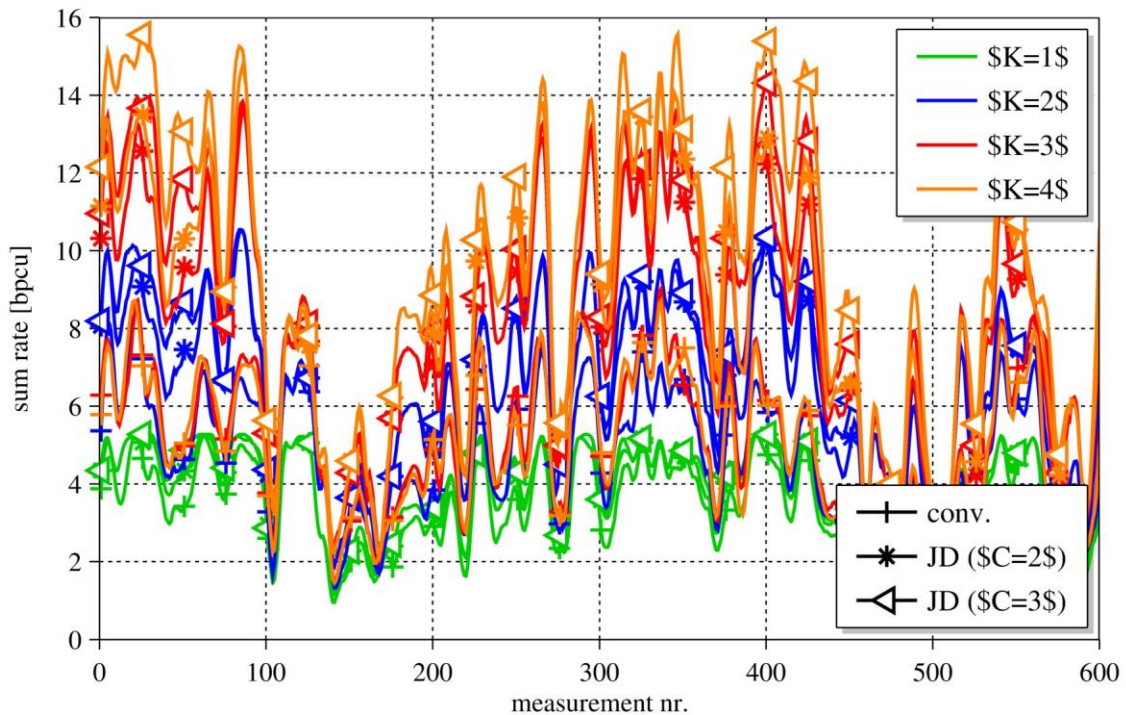


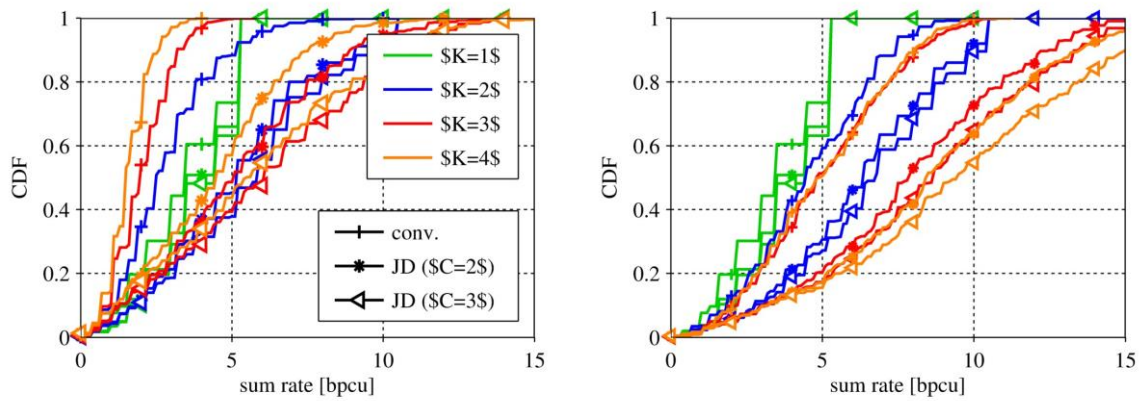
**Figure 41: Achieved rates for MMSE-SIC conventional and joint detection with cooperation cluster sizes  $C = 2$  and  $C = 3$  of  $K = 1, 2, 3, 4$  streams along the measurement route.**

The picture is different for SIC reception as shown in Figure 41 Figure 42 b). Now, the transmission of four streams achieved very large rates for any BS configuration, slightly outperformed by the transmission of three streams only for conv. reception. For cooperation

cluster sizes of  $C = 3$  even stream number adaptation gave only marginal gains while the transmission of four streams was optimal at over 70% of the measurement locations. We can observe in Figure 41 and Figure 36 that very high rates are possible at certain locations which is interesting for deployment of fixed relays as well. Fixed relays can be placed at selected locations where we see sum rates of up to 16 bpcu. This result is also very interesting for the downlink. Even though the results of this paper cannot be directly applied to this case, they indicate strong gains for joint transmission as well. And the use of joint transmission is very interesting for fixed relays due to rather static channel conditions of fixed wireless links which allow accurate precoding at rather low channel feedback rates.

**Table 8: Average sum rates for linear MMSE and MMSE-SIC detection and a different number  $K$  of Tx streams. The line named opt. is for optimal switching between different number of Tx streams**

K	conv. [bpcu]		JD ( $C = 2$ ) [bpcu]		JD ( $C = 3$ ) [bpcu]	
	SIC off / SIC on	SIC off / SIC on	SIC off / SIC on	SIC off / SIC on	SIC off / SIC on	SIC off / SIC on
1	3.45 / 3.45		3.81 / 3.81		3.90 / 3.90	
2	2.92 / 4.65		5.22 / 6.30		5.60 / 6.62	
3	2.09 / 5.10		5.21 / 7.88		6.10 / 8.50	
4	1.62 / 5.00		4.44 / 8.53		5.80 / 9.40	
opt.	3.79 / 5.50		5.96 / 8.73		6.87 / 9.58	



a) linear MMSE Detection

b) linear MMSE detection +SIC

**Figure 42: Rate CDF for different number of Tx streams ( $K = 1, 2, 3, 4$ ).**

## 3.5 Advanced Relays

Heterogeneous networks are gaining more and more interest as one means to cope with the expected data rise in future mobile networks. The upgrade of cellular macro networks by placing relay nodes, as one option, has the benefit of avoiding any wired backhaul network, but has to be paid by lower performance compared to pico stations. In the Artist4G, options were analyzed to get close to the performance of pico stations by using highly effective inband relaying. The focus was on two aspects: the use of CoMP techniques as researched in WP1 and channel prediction for moving relays. The use of CoMP for the uplink of a moving relay was already presented in Section 3.4.5. While the scenario that was measured therein was in some parts specific for a moving relay, the results can be generalized for a fixed relay as well. Using downlink joint transmission CoMP for a fixed relay was analyzed in WP3 as well and some of the assumptions and models that were used in this study were verified using field trial measurements as will be discussed in Section 3.5.1 below.

Downlink MIMO precoding requires accurate channel knowledge at the transmitter which is hard to get for a mobile scenario above pedestrian speeds. However, for vehicles it is possible to obtain such knowledge using a predictor antenna concept which was verified using field test measurements as well. The concept is presented in Section 3.5.2.

### 3.5.1 CoMP on the Fixed Feeder Link

Different deployment options exist for relay enhanced networks and an important issue is the height of the relays, i.e. whether relays will be placed above or below rooftop. Another feature that is considered for LTE-Advanced is Coordinated Multi-Point (CoMP) transmission. Joint transmission on the link between DeNB and relay node (RN) is very attractive to increase the channel rank under line-of-sight (LOS) conditions, which for single cell transmission is limited to two (two polarizations). By coordinating the transmission of multiple base stations the coverage of high data rates, the cell-edge throughput and/or to increase system throughput in both high load and low load scenarios can be increased. CoMP for moving UEs has some main challenges like optimum clustering and user grouping, channel estimation as well as channel state information feedback. For relay networks these challenges are relaxed significantly as the positions of relays are fixed. Thus using CoMP on the relay feeder link is an interesting use case. Using joint transmission on the feeder link is thus expected to be a key technology for a vast increase of cell throughput and spectral efficiency.

The goal is to maximize the performance of the donor eNB (DeNB) to RN links - i.e. of the feeder links - by a specifically adapted joint precoding coordinated multi-point (JP-CoMP) scheme which we refer to as cooperative relaying (CoR). These techniques were researched in WP3, and we refer to D3.5 for detailed explanations of the outcomes of this work. A detailed survey on this topic can also be found in [29] which includes field trial results from the Dresden testbed that are used to investigate the performance of CoMP for the relay feeder link in a cellular environment.

### 3.5.2 Using Predictor Antennas for Moving Relays

D3.5 Part C (Section 2.2.2) presents a channel prediction method for moving relay scenarios where conventional prediction, based on past and present channel measurements is not sufficiently working anymore. The basic idea of the method is using a predictor antenna in order to increase the prediction horizon. The predictor antenna would need to be located some distance directly in front of the antennas used for transmission. Using channel models that are available today it is not possible to model this kind of scenarios and to evaluate which aspects actually limit the prediction performance. The results of these measurements are presented in D3.5 and in [21]. In this section, we give an overview of the measurement setup and describe a wide range of additional measurements that are not included in [21].

#### 3.5.2.1 Measurement Setup

The transmitter and the receiver were implemented using Signalion's HaLo prototyping equipment. A  $B=20$  MHz OFDM signal with  $N_s=2048$  subcarriers was generated and up-converted to 2.68 GHz at the transmitter. Each OFDM symbol was modulated by the same Zadoff-Chu pilot sequence which features constant amplitude in the frequency domain and a low peak-to-average power ratio in the time domain. No prefix was added since the time

domain signal is cyclic and the OFDM symbol duration was therefore  $\frac{N_s}{B} \approx 0.1$  ms. At the receiver, snapshots of the digital base band signal were stored after adjustable amplification (to optimize the dynamic range of an analogue-digital converter), down-conversion, analogue-digital conversion, sample rate conversion, and filtering. All other receiver algorithms such as synchronization, carrier frequency offset compensation, and FFT were applied offline. The channel was then estimated in the frequency domain.

The prototype equipment was subject to hardware impairments that could only be rectified partially. Examples are gain imbalances on different transmit/receiver paths and asynchronous local oscillators that cause effects like carrier frequency offsets, sampling clock offset, and phase noise. Thus, a compound channel (similar to a system used in the real world) including hardware effects, antenna effects, and the wireless channel was measured.

The measurement setup consisted of a single antenna transmitter located on the rooftop of an apartment at a height of about 55 m and a receiver which is connected to two standard vertically polarized dipole receive antennas (KATHREIN 80010431). The receive antennas were placed in line with variable distance  $\Delta s$  on the roof of a measurement bus such that the channel observed at the first (predictor) antenna could be used for predicting the channel of the antenna behind it, as previously described. At the transmitter, the  $+45^\circ$  polarization of a standard cross polarized base station antenna (KATHREIN 80010541 - characterized by  $58^\circ$  horizontal beamwidth and 18 dBi gain) was used. The total transmit power was 36 dBm, and the downtilt was set to  $9^\circ$ .

Measurements were performed at a vehicular velocity of 45-50 km/h in a residential neighborhood surrounded by buildings of height 10–50 m. In the experiments, very low power was received at some subcarriers (including the central subcarrier). These subcarriers were excluded from the investigation which utilized 1784 out of 2048 subcarriers.

Measured data were collected by full-band measurements with a duration of 200 ms. One location was with line-of-sight (LOS) propagation to the base station and one was a non-line of sight (NLOS) location where the base station was blocked by a building. The 200 ms windows correspond to distances of 2.78 m ( $\approx 24$  carrier wavelengths) for mobile speeds of 50 km/h.

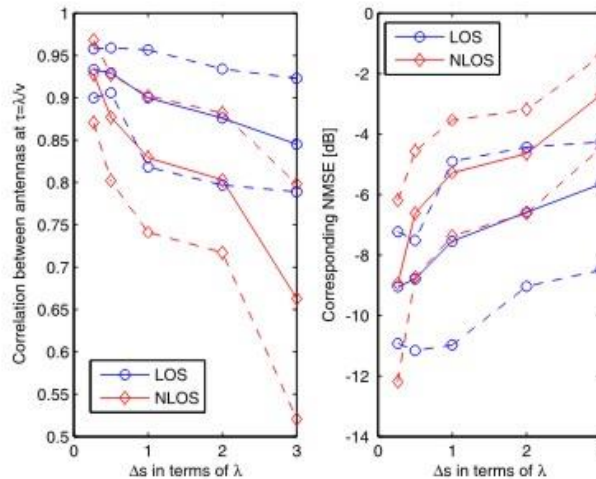


**Figure 43: Measured statistics for the peak correlation magnitude (left) and the corresponding attainable normalized MSE for a LOS and NLOS scenario. Solid: average over all subcarriers as a function of the distance between the antennas. Dashed and dash-dotted lines represent the 95th and 5th percentiles, respectively.**

Distances between the two antennas were set to  $\lambda/4, \lambda/2, \lambda, 2\lambda$  and  $3\lambda$ . Three measurements were performed at each location for each setting of antenna distance. The exact vehicle position differed by a couple of meters between the three repetitions of each case. We refer to [21] for the detailed evaluation of these measurements. As an example, Figure 43 shows correlation and normalized mean square error (NMSE) results for the two measurement locations. While the correlation is still quite high even for  $3\lambda$  antenna distance, it would not be

sufficient for coherent downlink precoding. In order to investigate the reasons for this decorrelation, we thus a couple of further measurement campaigns where we optimized the setup in several steps. In particular, we did the following adjustments

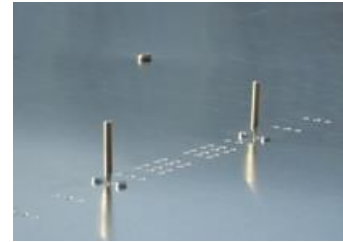
- use of a metal sheet on car roof under the antennas in order to create an optimal (and equal) local environment for all antennas, (Figure 44 a)
- use of so called ghost antennas in front and behind the measurement antennas which were grounded but not used for reception. The idea here was again to create an equivalent environment for both antennas that includes coupling effects (Figure 44 b)
- use of  $\frac{\lambda}{4}$  monopole antennas which have optimized transmit patterns when placed on a large ground plane (as done in the measurements). (Figure 44 c)



a) Metal sheet under car roof



b) Ghost antennas in front and behind the measurement antennas



c) monopole antennas on metal sheet

**Figure 44: Different setups of second measurement campaign**

First results of these measurements are presented in D3.5 Part C as well.

### 3.6 Downlink CoMP

#### 3.6.1 Validation of Tortoise Concept

The Tortoise Concept for downlink and uplink CoMP is an ARTIST4G innovation presented in D1.4 [6]. The accuracy of the simulation results that are presented in this document is limited by the accuracy of the channel models that have been applied. Unfortunately, the 3GPP 3D antenna model does not accurately describe the vertical dimension of a cellular system since it is constantly considered to have LOS characteristics. However, this aspect is crucial for Tortoise CoMP because a cooperation area and wideband beam specific downtilt is used to separate cooperation areas and thus to lower the mutual interference floor between cooperation area centers. A more solid 3D modeling would require the consideration of multiple reflection clusters as considered in the horizontal dimension. In order to validate the assumptions and results of the previous sections, we, thus, used extensive large scale field trials with regard to these most critical aspects.

The testbed setup, consisting of 16 BSs, is depicted in Figure 45. In a first field trial, we were interested in the impact of the downtilt on pathloss and coverage. In order to investigate this

aspect, the same measurement route was traversed twice. For the first trial a

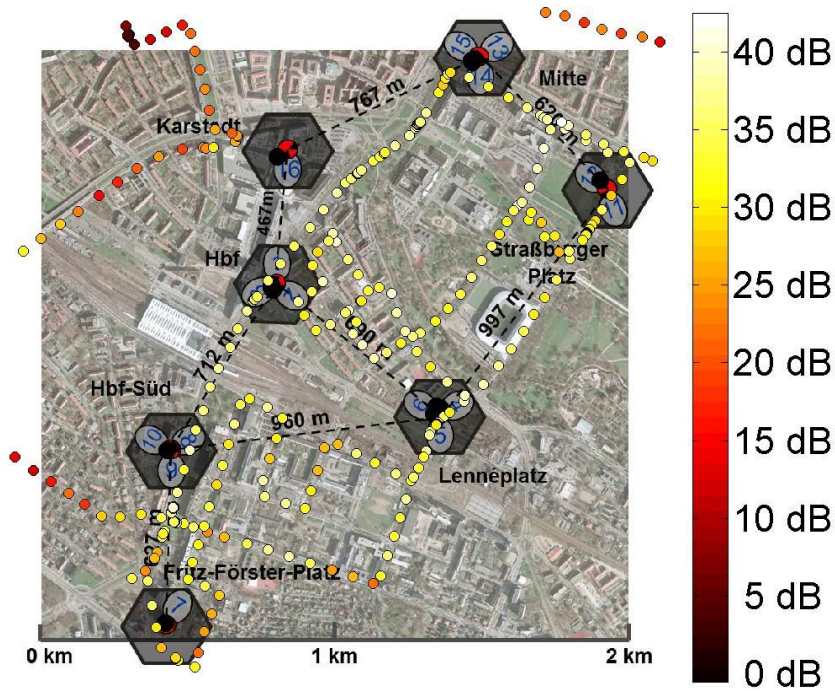


**Figure 45: Field trial setup and measurement locations (colored dots) for the first field trial. The color indicates the SNR to the strongest base station for a downtilt of 6°.**

downtilt of 6° and for the second trial a downtilt of 12° was used. During the trial a single UE transmitted in uplink OFDM pilots with transmit power of 37dBm over a bandwidth of 5.4 MHz at a carrier frequency of 2.6 GHz. The received signal at all base stations was synchronously captured every 10 s and evaluated with respect to the channel transfer function (CTF) estimation and a SNR estimation. For further details on the evaluation procedure, we refer the reader to D6.1 and Section 3.3.1. The measurement locations are marked in Figure 45 as well, using colored dots that indicate the SNR to the strongest base station for each location. In total 479 measurements were taken in each trial. For technical reasons, the measurement locations for both trials are not exactly the same which, however, does not has a crucial effect on the following results since the data is evaluated statistically. In figure 14, we show how the average SNR depends on the distance to the base stations for the two different downtilt settings. In order to evaluate the relationship between SNR and distance to the base station, we determined the distance to all 16 base stations for each measurement location.

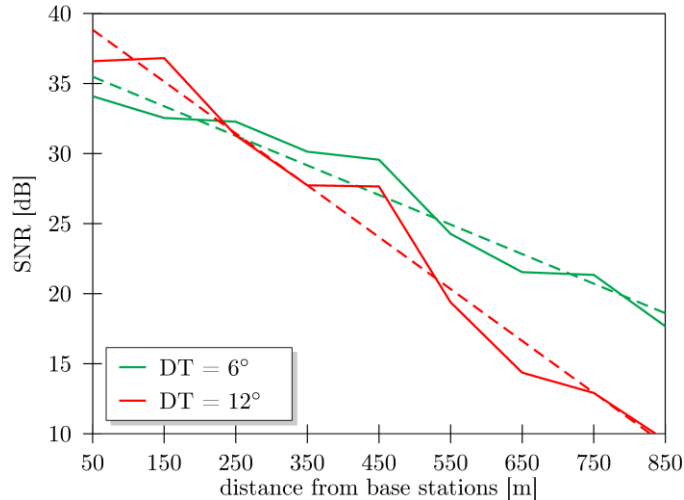


**Figure 46: Average SNR [dB] over distance from base station. Average over results from 16 BSs. The dashed lines show a linear fit.**

Figure 46 shows the average SNR that was measured at different distances to the base stations. However, for each location only the SNR of those base stations was considered which antennas were facing to the measurement location, with a tolerance of 30°. Figure 46 also shows that the SNR in dB decreases linearly with distance with an average SNR degradation of 2.1 dB and 3.7 dB every 100m for a downtilt of 6° and 12° respectively. Note that this observation differs from the typical assumption of an exponentially increasing path-loss. However, one has to consider that we measure combined effects that include limited dynamic range of AD-converters and antenna patterns. The results are useful to validate the results of our system level simulations and they show that an appropriate setting of the downtilts in a cover shift allows for separation of cooperation areas. For that purpose BSs or wideband beams that are facing outside the cooperation areas should apply a larger downtilt in order to decrease the interference to other cooperation areas.

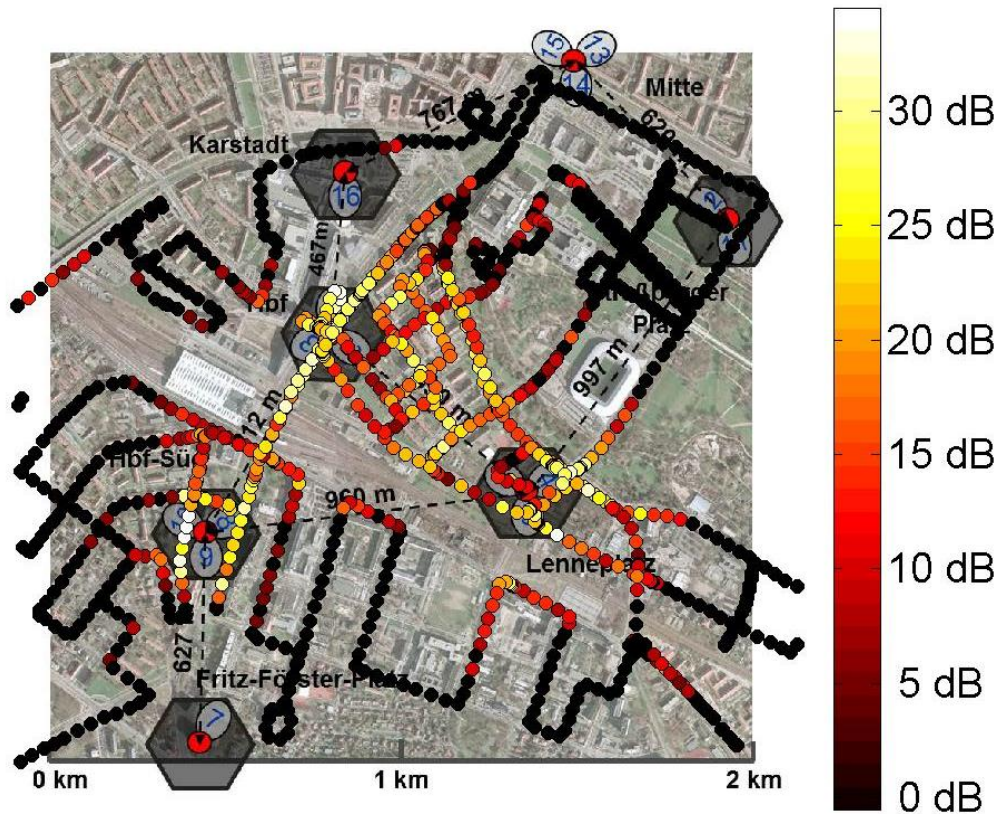
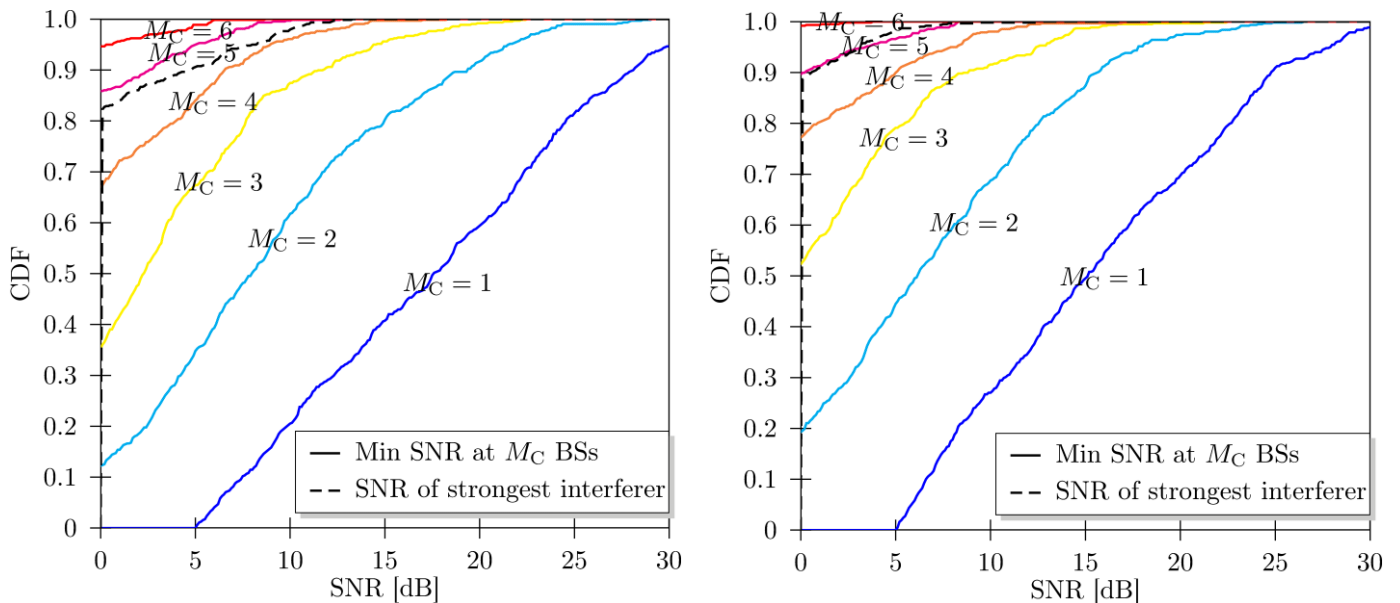


**Figure 47: SNR in a cooperation area including the sites Hbf, Lenneplatz and Hbf-Süd using the tortoise concepts**

As described in D1.4, coverage holes that would occur due to this strong isolation of cooperation areas would be closed by using different cover shift on several layers that are separated by using different resources for each layer. Layer specific cover shifts could be realized by vertical beamforming. Our goal in the field trial that is described in the following was to explore how well different cooperation areas could be separated using these techniques. Since vertical beamforming was not available in the employed field trial system, we concentrated on the separation of a single cooperation area from neighboring base stations. The general field trial setup is the same as shown in Figure 45. The cooperation area of interest was made up of the three sites Hbf-Süd, Hbf, and Lenneplatz. Thus, in order to achieve a good coverage and large cooperation gains inside of the cooperation area a rather low downtilt of 7° was chosen at base station 2, 6, 8 that are facing inward. At all other base stations of the cooperation area a larger downtilt of 17° was chosen in order to minimize the interference to other cooperation areas. The downtilt at all surrounding base stations was 17° as well as those would be interferers from surrounding cooperation clusters that transmit on the same resources. Figure 47 shows the result of a field trial where a single transmitting UE traversed through a

wide area of the testbed. The color of the measurement locations indicates the maximum SNR measured at any base station of the cooperation cluster. A black dot is shown at measurement locations where the SNR to all base station in the cooperation cluster is below 0dB or where a base station that is not part of the cooperation cluster has a higher SNR than all base stations in the cooperation cluster. Compared to the previous trial in Figure 45, the transmit power was reduced to 18 dBm, thus the SNR is clearly lower as it would be achievable in a cellular downlink with macro base stations. An inherent feature of the interference mitigation concept being proposed is joint transmission of base stations in a cooperation cluster.

The statistics for the SNR that is instantaneously achieved at several base stations for all measurement locations in the cooperation area is shown in Figure 48a). For example the blue curve shows the CDF of SNR of the strongest base station at each location. The other solid curves show the CDF of the minimum SNR instantaneously achieved at several base stations. For example at 40% of the measurement locations the SNR was larger than 10 dB at two base stations of the cooperation cluster instantaneously. Considering that the transmit power at a typical base station would be about 30dB higher as that used in this field trial one can conclude that there would be definitely a strong benefit from cooperation. The dashed curves show the SNR CDF of the strongest interfering base station. Thus, a partial feedback (and precoding) scheme might restrict cooperation to no more than four base stations. In order to increase this number, the presented framework incorporates the option for power control as presented in D1.4. Figure 48b) shows the impact of a power setting, where base stations that face out of the cooperation area have a transmit power that is reduced by 6 dB. Since this field trial was done in the uplink, the impact of a reduced transmit power was obtained by a reduction of the measured SNR. While the reduced transmit power has only small effect on the SNR in the cooperation cluster, the strongest interferer is reduced by 6dB resulting in a significant increase of the average SINR.



a) Without power control. We see that typically 4 base stations in the CA have a higher SNR than the first interferer.

b) Same as in figure on the left but with 6dB lower transmit power at BSs that are facing outwards.

**Figure 48: CDF of SNR at the base stations in the cooperation area (CA). The dashed curve shows the CDF of the SNR of the first interferer from outside of the CA.**

## 3.7 Performance Assessment of MIMO Receivers in LTE Systems

### 3.7.1 Introduction

In this contribution we present the performance comparison of different MIMO receivers including the MMSE-IC presented from WP2 [5]. Among the existing algorithms, the maximum a posteriori (MAP) algorithm provides the optimum performance for detection. However, the MAP algorithm has high complexity, which makes it unrealistic for practical cases. Even though some simplified versions have been proposed, e.g. max-log MAP (MLM), they still suffer from high complexity problem. When the *a priori* information is not available or the transmitted symbols are assumed to be uniformly distributed, the MAP algorithm can be approximated by the maximum likelihood (ML) algorithm, which still has considerable complexity. As an alternative, the minimum mean square error (MMSE) linear equalizer has a lower implementation complexity. Even though, the MMSE equalizer has some performance degradation compared to the ML equalizer, it is still widely used in MIMO receivers today because of its lower complexity.

In recent years, with the appearance of “turbo principle”, iterative receivers are becoming more and more popular and promising because of their attractive performance. Different mechanisms have already been proposed and studied. For example, the Iterative MMSE-IC has been proposed and investigated. It can provide excellent performance; however, the equalizer coefficients have to be updated at each iteration, resulting in a very high complexity. Meanwhile, with MIMO transmission, multiple streams can be transmitted in parallel through multiple layers from multiple antennas and, consequently, a superposition of these layers arrives at the receiver antennas. For the purpose of detecting the transmitted symbols, interference cancellation (IC) methods are being investigated. With the IC equalizer, symbols in different streams are detected step-by-step and the estimated interference is removed from the received superimposed signals. The IC equalizer has been integrated with different equalization algorithms resulting in different IC methods. Most popular ones are minimum mean square error (MMSE) equalizer based IC equalizer (MMSE-IC) and zero forcing (ZF) equalizer based IC equalizer (ZF-IC) which have been shown to improve system performances (see, e.g., [5] and references therein). In the sequel, we first give a brief review of the MIMO receivers and present a simplified MMSE-IC equalizer based on LTE receiver structure. Then, we provide performance comparison of these algorithms.

### 3.7.2 Review of the MIMO receivers

#### 3.7.2.1 Simple Equalizers

In this section we will review the conventional equalizers, namely, ML and MMSE. The ML is a powerful detection algorithm for multi-input multi-output (MIMO) transmission, e.g. spatial multiplexing (SM) transmission mode. However, it also has a high complexity especially for higher level modulation schemes such as 64-QAM, and multiple data streams, e.g. two code words transmitted simultaneously through SM transmission mode.

The ML equalizer is defined as

$$\hat{\mathbf{s}} = \min_{\mathbf{s} \in \Xi^L} \|\mathbf{y} - \mathbf{H}\mathbf{s}\|^2, \quad (3.7.1)$$

where  $\hat{\mathbf{s}}$  stands for equalized symbol vector,  $\mathbf{H}$  is channel matrix, and  $\mathbf{y}$  is received symbol vector. The set  $\Xi^L$  represents all possible combinations of symbols from different data streams, where  $L$  is the number of data streams. When the constellation is large, e.g. 64QAM, and multiple data streams are transmitted, the ML equalizer will have an extremely high complexity.

Compared to ML equalizer, the MMSE equalizer has lower complexity and is defined as

$$\hat{\mathbf{s}} = (\mathbf{H}^H \mathbf{H} + \sigma^2 \mathbf{I}_{Q \times Q})^{-1} \mathbf{H}^H \mathbf{y}, \quad (3.7.2)$$

where  $\sigma^2$  represents noise variance. In (3.7.2), the matrix  $\mathbf{I}_{Q \times Q}$  is an identity matrix with the size of  $Q$ , where  $Q$  denotes the number of layers.

### 3.7.2.2 IC Equalizers

#### 3.7.2.2.1 Iterative Equalizers

This section provides an overview of iterative equalizers, which use “soft” information from turbo decoder to improve equalization performance, including MAP and MMSE-IC.

The maximum a posteriori (MAP) algorithm provides the optimum performance for detection by using soft feedback from the turbo decoder to calculate the a posteriori probability (APP) of each symbol on each data stream. This APP calculation leads to a high complexity, which makes it unacceptable in practical cases.

The iterative MMSE equalizer has been proposed in literature [32][33][34][35]. The iterative equalizer uses the “soft” information from turbo decoder to improve equalization performance. In each iteration, the  $k$  th equalized symbol  $\tilde{s}_k$  is calculated as

$$\tilde{s}_k^{(i)} = \mathbf{p}_k^{(i)\text{H}} \mathbf{y} - \mathbf{q}_k^{(i)\text{H}} \hat{s}_k^{(i)}, \quad (3.7.3)$$

where the vector  $\mathbf{p}_k^{(i)}$  and the vector  $\mathbf{q}_k^{(i)}$  are obtained based on the MMSE criterion

$$\mathbf{p}_k^{(i)} = \left( \mathbf{H} \mathbf{V}_k^{(i)} \mathbf{H}^{\text{H}} + \sigma^2 \mathbf{I}_{Q \times Q} \right)^{-1} \mathbf{h}_k, \quad (3.7.4)$$

and

$$\mathbf{q}_k^{(i)} = \mathbf{H}^{\text{H}} \mathbf{p}_k^{(i)}. \quad (3.7.5)$$

In (3.7.4), the matrix  $\mathbf{V}_k^{(i)}$  is calculated as

$$\mathbf{V}_k^{(i)} = \mathbf{e}_k \mathbf{e}_k^{\text{T}} + \sum_{q=0, q \neq k}^{Q-1} v_q^{(i)2} \mathbf{e}_q \mathbf{e}_q^{\text{T}} \quad (3.7.6)$$

and

$$v_q^{(i)2} = \sum_{s \in \Xi} |s|^2 P(\hat{s}_q^{(i)} = s) - |\hat{s}_q^{(i)}|^2, \quad (3.7.7)$$

where  $\Xi$  represents all possible constellation points and the vector  $\mathbf{e}_k$  represents a column with “1” for the  $k$  th element and zeros for all other elements.

#### 3.7.2.2.2 Simplified IC Equalizer (MMSE-MFIC)

Even though the iterative MMSE equalizer provides remarkable performances, its complexity is extremely high due to the matrix inversion for each symbol per iteration. By assuming perfect symbol estimation at each iteration, the vector  $\mathbf{p}_k^{(i)}$  in iterative MMSE equalizer can be simplified as

$$\mathbf{p}_k^{(i)} = \mathbf{h}_k. \quad (3.7.8)$$

With this simplification, no matrix inversion is needed for calculating the equalization vectors. This simplified iterative MMSE equalizer is named as Matched Filter IC MMSE equalizer (MMSE-MFIC) [5].

However, even with the MMSE-MFIC equalizer in (3.7.8), the complexity of receiver is still high, since “soft” information feedback of multiple streams are always needed, which adds huge complexity to receiver. In order to further simplify the MIMO equalizer, a “hard” feedback scheme can be adopted by considering cyclic redundancy check (CRC). In LTE, a CRC is a specifically designed code to detect whether a code block is decoded correctly or not. At transmitter side, based on the information bits and some special algorithm, a CRC code is produced and attached to the information sequence. Then, the information bits and the CRC code are encoded together; a code block (CB) is obtained and transmitted. At receiver side, the code block is decoded by turbo decoder (TDC). The receiver decides whether the code block is correctly decoded based on the decoded information bits and decoded CRC bits. For MIMO transmission with multiple code words, multiple CRCs can be obtained at receiver side, as

shown in Figure 49 with two code words as an example. In this section, we focus on two code word case.

When two different data streams have different CRC values (one is OK and the other one is KO), the data stream with CRC OK will be fed back by TDC to equalizer (EQU) to cancel the interference over the other data stream, i.e.,

$$\begin{cases} \text{if CRC0} = \text{CRC1: no feedback} \\ \text{if CRC0} \neq \text{CRC1: feedback the data layer with CRC} = \text{OK} \end{cases}$$

If one data stream is chosen to be fed back (shown by FB in Figure 49), all “hard” decisions (equal to “0” or “1”) of system bits in the data stream will be fed to “Encoder”, “Rate Match”, “Scramble”, and “Modulation” modules to construct “estimated symbols” ( $\hat{s}_k^{(i)}$ ).

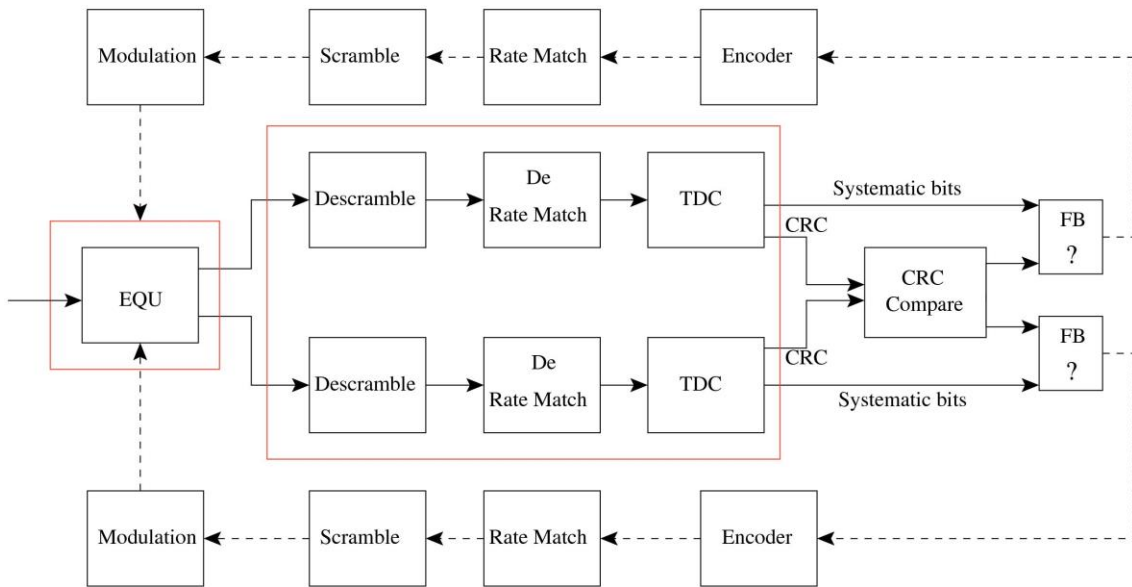


Figure 49: Receiver with IC equalizer.

### 3.7.2.3 Complexity

In this section, complexity comparison of the equalizers discussed in Section 3.7.2.1 and Section 3.7.2.2 are compared. Since the MAP and iterative MMSE equalizers are too complex to be implemented in practical cases, we compare only the MMSE, ML and MMSE-MFIC equalizers in Table 9.

In order to compare complexities of different equalizers, we check the number of real multiplication (RM), real addition (RA), and real division (RD) needed by each equalizer. In Table 9,  $Q$  represents the number of layers in MIMO transmission,  $R$  stands for the number of receive antennas, and  $M$  is the size of modulation constellation. Furthermore, an example is given with  $Q = 2$ ,  $R = 2$ , and  $M = 64$ .

Table 9: Complexities of different equalizers

Operation Equalizers	RM	RA	RD	Eg. (64QAM 2x2)		
				RM	RA	RD
MMSE	$\frac{16}{3}Q^3 + 12Q^2R$	$\frac{8}{3}Q^3 + 12Q^2R - 2Q^2 - 4QR + Q$		139	95	

<b>ML</b>	$18RQM^{Q-1}$	$(16R - 3 + \log_2^M)QM^{Q-1}$		4608	4480	
<b>MMSE-MFIC</b>	$MMSE + 12R + 4$	$MMSE + 12R - 2$	2	167	117	2

From Table 9, we see that the simple MMSE has the lowest complexity and the MMSE-MFIC has a slightly higher complexity, which comes from the second iteration with “hard” feedback. The ML equalizer has a much higher complexity than MMSE and MMSE-MFIC.

### 3.7.3 Simulation Results

In this section, the equalizers described in section 3.7.2 will be compared through some simulation results. All simulations are performed over a clock-driven LTE simulator which is fully compliant to Rel. 9. In order to evaluate the performance of IC equalizer, additional feedback mechanism has been implemented following the architecture described in Figure 49. Relevant simulation parameters are summarized in Table 10.

**Table 10: Simulation Parameters**

Parameter	Value
Uplink Downlink Config.	1
Special Subframe Config.	4
Transmission Mode	Open Loop Spatial Multiplexing
MIMO	2x2
Correlation	LOW: $\rho_A = 0 \quad \rho_B = 0$ HIGH: $\rho_A = 0.9 \quad \rho_B = 0.9$
Band Width	10 MHz
Number of OFDM symbols for PDCCH	2

In Figure 50, performances of all equalizers discussed in section 3.7.2 are plotted. From this figure, we see that the MAP equalizer gives the best performance and the iterative MMSE equalizer can approach the MAP equalizer with more iterations. However, since both of them have extremely high complexities, we will focus on the equalizers which have lower complexity and are more feasible for practical MIMO receiver, i.e., MMSE, ML, and MMSE-MFIC.

In Figure 50, Figure 51, Figure 52, and Figure 53, simulations results show that the ML equalizer always outperforms MMSE equalizer for different MCSs (16QAM and 64QAM) and over different channels (low and high correlation channels). The MMSE-MFIC equalizer slightly improves or does not improve the performances of MMSE equalizer, because both streams often have the same CRC values. According to the feedback criterion described in section 3.7.2.2.2, there is not much feedback to MMSE-MFIC equalizer and the performance keeps the same as that of MMSE, since the MMSE equalizer is always used in the first iteration of MMSE-MFIC.

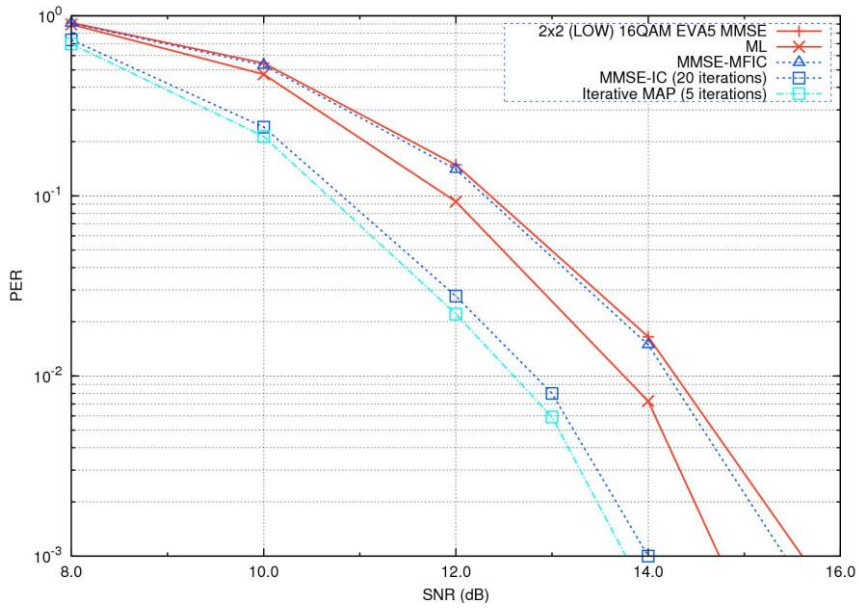


Figure 50: PER performance with 16QAM 1/2 over low correlated channel.

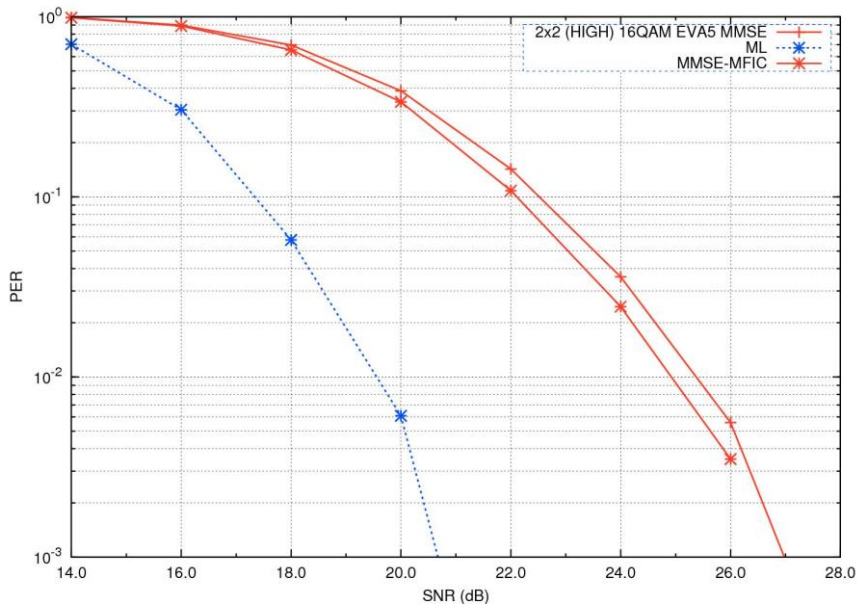


Figure 51: PER performance with 16QAM 1/2 over high correlated channel.

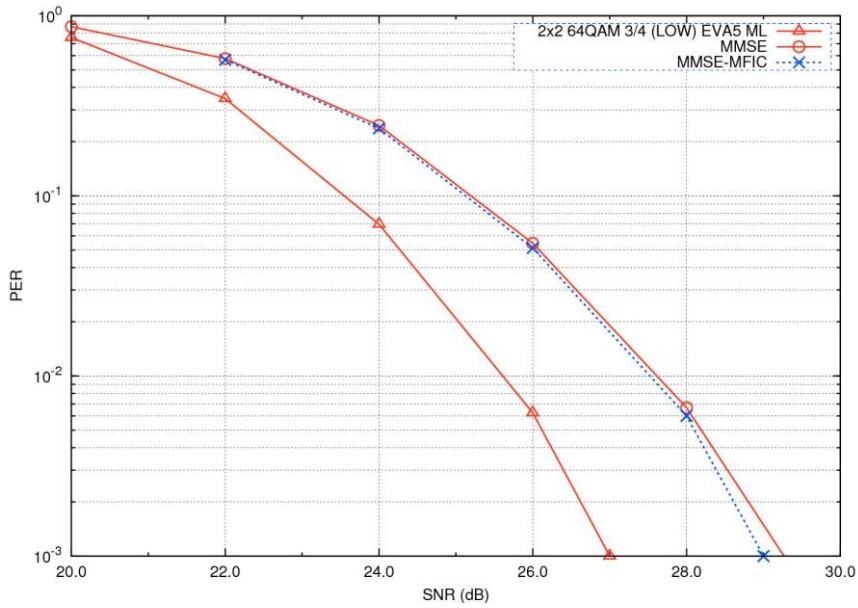


Figure 52: PER performance with 64QAM 3/4 over low correlated channel.

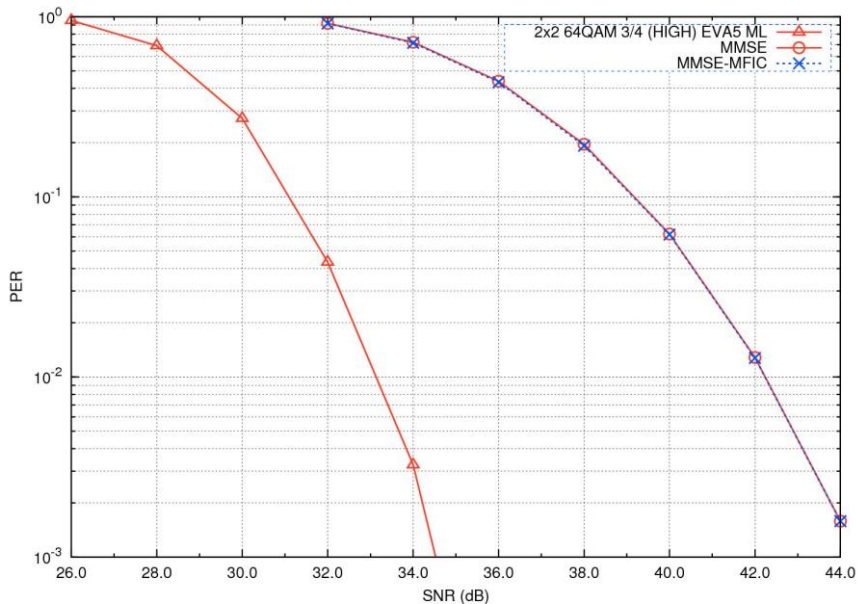
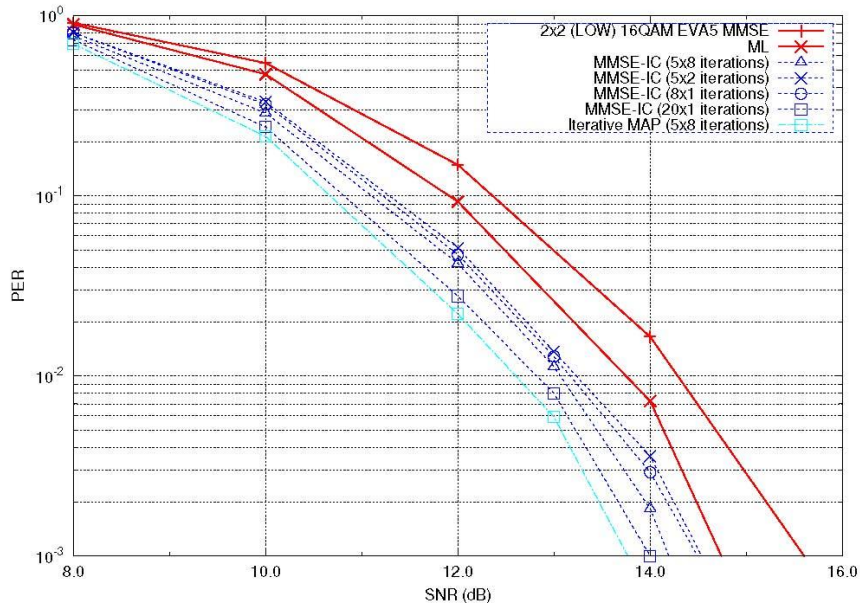


Figure 53: PER performance with 64QAM 3/4 over high correlated channel.

In Figure 54 the performance of MMSE-IC is evaluated with different turbo decoder iteration strategies, Here, different combinations of equalizer iteration and turbo decoder iteration are considered. For example, “5x8 iterations” means that the performance is obtained with 5 equalizer iterations and in each equalizer iteration, 8 turbo decoder iterations are performed. From Figure 54, we see that the “20x1 iterations” gives the best performance, which approaches the performance of MAP equalizer using “5x8 iterations” setting. With other settings in the figure, the MMSE-IC equalizer has some degradation compared to “20x1 iterations” setting. These results tell that the MMSE-IC equalizer can obtain excellent performance with fewer iterations in turbo decoder, leading to a complexity reduction of turbo decoding but will add additional looping complexity. At the end, the total complexity will solely depend on the architecture.



**Figure 54: MMSE-IC equalizer with different iteration settings.**

In Figure 55, Figure 56, Figure 57, and Figure 58, we focus on the transmission of transport blocks with different MCS values. The ML equalizer still outperforms MMSE equalizer with different MCSs on two streams. However, the MMSE-MFIC equalizer improves remarkably the performance compared to that of MMSE equalizer. In Figure 55, Figure 56, and Figure 57, the performance of MMSE-MFIC outperforms that of ML and in Figure 58, it approaches the ML equalizer with 64QAM over high correlation channel. The huge improvement comes from the different MCSs on two streams. Since the two different MCSs have different coding rate, after turbo decoder, the two streams often have different CRC values: one is correctly decoded while the other one is not. According to the feedback criterion described in section 3.7.2.2.2, with these different CRC values, we always have “hard” feedback of one stream to help equalizer improve performance by cancelling the interference on the other stream.

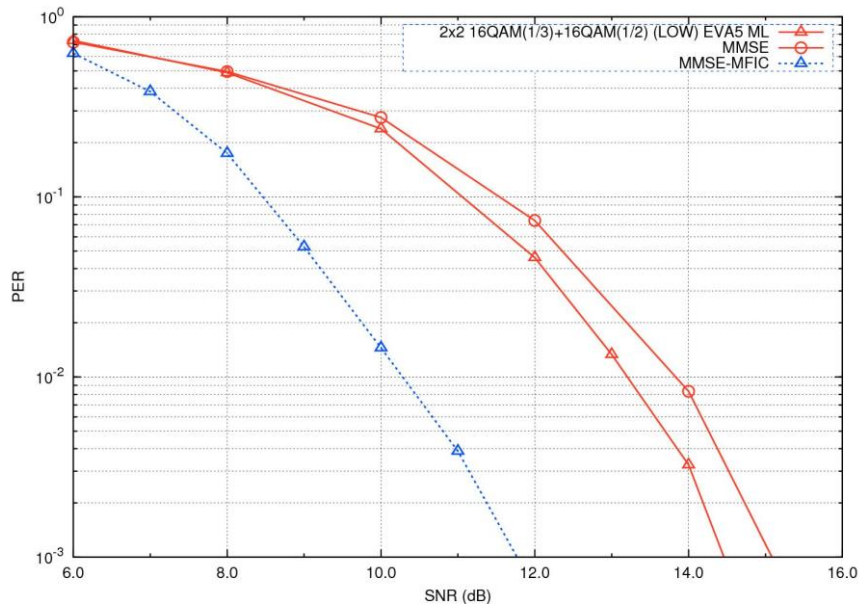


**Figure 55: PER performance with 16QAM 1/3 and 16QAM 1/2 over low correlated channel.**

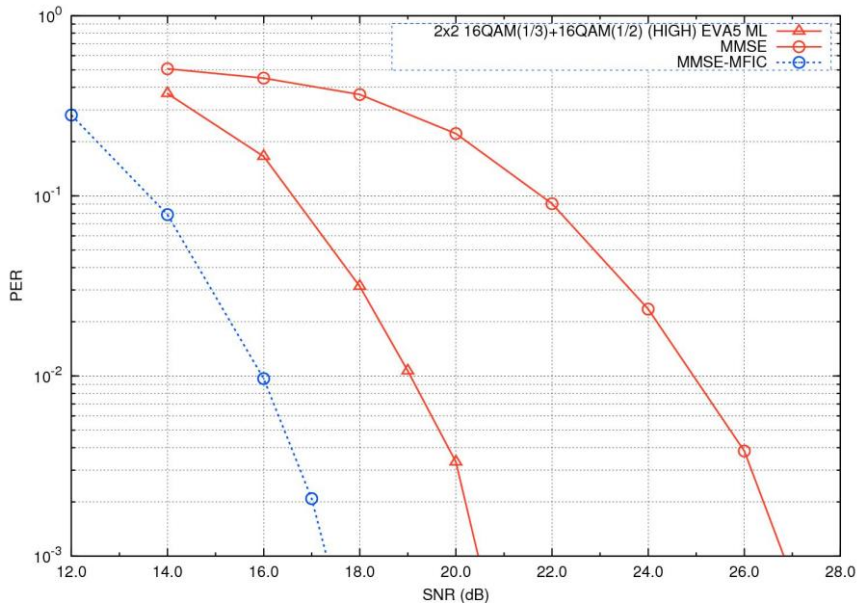


Figure 56: PER performance with 16QAM 1/3 and 16QAM 1/2 over high correlated channel.

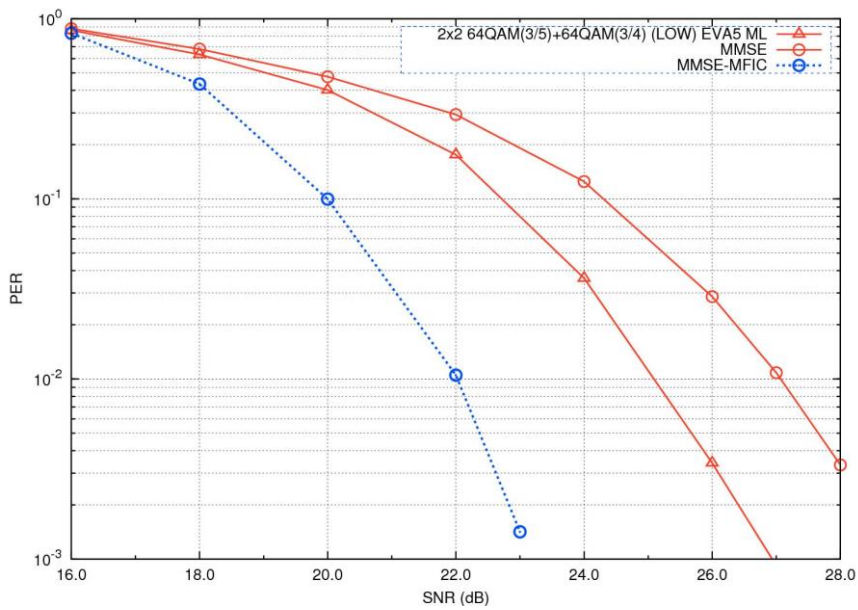
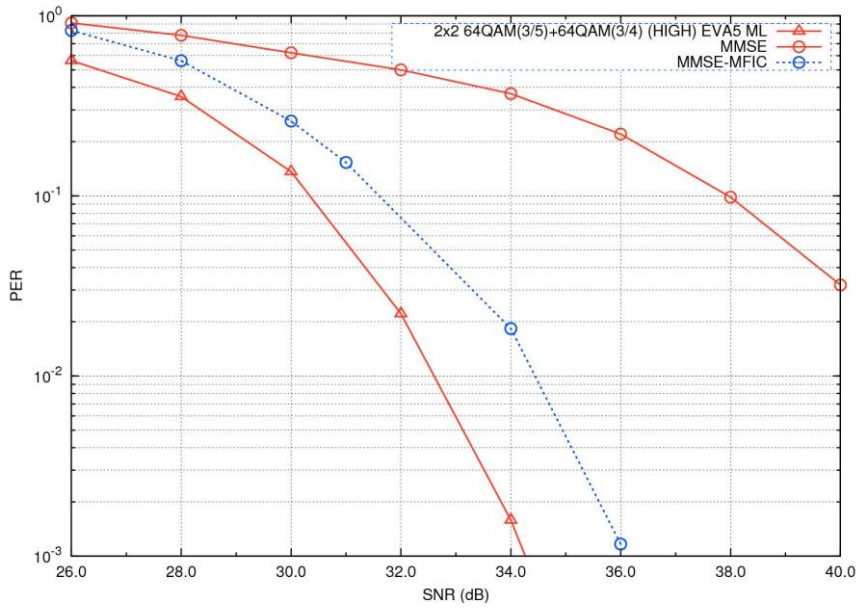


Figure 57: PER performance with 64QAM 3/5 and 64QAM 3/4 over low correlated channel.



**Figure 58: PER performance with 64QAM 3/5 and 64QAM 3/4 over high correlated channel.**

### 3.7.4 Conclusions

In this section, some simple and IC equalizers are reviewed and compared through simulation results. In particular, performances of MMSE and ML are shown as benchmark to evaluate IC equalizers. Simulation results show that the MAP and soft decision based iterative MMSE equalizers provide the best performances, but they have too high complexities to be implemented in practical receivers. Different iteration configurations are also presented for MMSE-IC which show an interesting trade-off between global and turbo decoder iterations. Compared to MAP and iterative MMSE equalizers, the simplified MMSE-MFIC takes advantage of CRC in LTE and has much lower complexity. However, with the same MCS on different streams, the MMSE-MFIC provides only a small improvement. When different MCSs are used on different streams, the MMSE-MFIC improves performance remarkably over both low and high correlated channels.

## Conclusions

In the deliverable, a second set of lab and field trial results on ARTIST4G innovations was presented. We believe that the integrated approach of theoretical, simulative and practical studies was extremely beneficial to achieve the overall project goals. Lab and field trials with 3D beamforming have shown the potential for further significant improvements of the system performance for cellular systems. As predicted by simulation 3D beamforming provides gain in spectral efficiency and cell edge throughput.

For uplink CoMP we have seen in a range of field trial evaluations that the gains promised by theory can also be seen in real systems. One focus was on the evaluation of uplink CoMP in systems with limited backhaul capacity. One option that was evaluated in this respect was the option of intra-site cooperation which we compared with inter-site cooperation of two or more base stations. Furthermore, we looked into uplink CoMP on the moving relay feeder link and showed the great potential of a system that combines these approaches for more fair and reliable communications.

A further focus was the use of field trials to validate simulation results. This was done for CoMP on the relay feeder link and for the Tortoise CoMP concept which is a major component of the overall CoMP framework proposed in WP1.

A downlink CoMP scenario under emulated channel conditions has been implemented on a testbed involving three MAGALI platforms organized around a 57-router Network-on-Chip that connects 87 telecom-oriented processing units. Feedback on this implementation shows the great potentials of the system on chip architecture. It gives some guidelines for the next generation of PHY layer hardware architecture which would require increasing signal processing algorithmic complexity at the mobile terminal while keeping flexibility and low power consumption. The real-time processing of the MAGALI board and the test automation provide an efficient hardware emulator for validating complex cooperation scenarios required to improve the cell-edge throughput performances.

## 4 References

- [1] ARTIST 4G, "D1.4 – Performance assessment of the most promising interference avoidance techniques, Artist 4G technical deliverable, June 2012
- [2] ARTIST4G, "D6.2 - Laboratory and field trial results connected to the first set of innovations, Artist4G technical deliverable, September 2011
- [3] H. Halbauer, S. Saur, J. Koppenborg, C. Hoek; "Interference Avoidance with Dynamic Vertical Beamsteering in Real Deployments", WCNC 2012 Paris
- [4] J. Koppenborg, H. Halbauer, S. Saur, C. Hoek, "3D Beamforming Trials with an Active Antenna Array", WSA 2012 Dresden
- [5] ARTIST4G, "D2.2 – Advanced receiver signal processing techniques: evaluation and characterization", ARTIST4G technical deliverable, 2011
- [6] ARTIST4G D1.4 - Performance assessment of the most promising interference avoidance techniques, Artist4G technical deliverable, 2012
- [7] M. Danneberg, J. Holfeld, M. Grieger and G. Fettweis, "Field Trial Evaluation of UE Specific Antenna Downtilt in an LTE Downlink," ITG Workshop on Smart Antennas (WSA' 12), 2012
- [8] Holfeld, J. and Fischer, E. and Fettweis, G.; "Field Trial Results for CoMP Downlink Transmissions in Cellular Systems," International ITG Workshop on Smart Antennas (WSA '11), 2011
- [9] Holfeld, J. and Riedel, I. and Fettweis, G.; "A CoMP Downlink Transmission System Verified By Cellular Field Trials," 19th European Signal Processing Conference (EUSIPCO 2011), 2011.
- [10] Technical Information Operating Instructions: GPS170LCD-MP. Meinberg Funkhuren GmbH & Co. KG, 2007.
- [11] Gunnarsson, F. and Johansson, M.N. and Furuskar, A. and Lundevall, M. and Simonsson, A. and Tidestav, C. and Blomgren, M.; "Downtilted Base Station Antennas - A Simulation Model Proposal and Impact on HSPA and LTE Performance," Vehicular Technology Conference (VTC 2008-Fall), 2008.
- [12] P. Marsch; G. P. Fettweis, "Coordinated Multi-Point in Mobile Communications: From Theory to Practice", Cambridge University Press, 2011
- [13] Kotzsch, V. and Rave, W. and Fettweis, G.; "Interference Cancellation and Suppression in Asynchronous Cooperating Base Station Systems," Proc. International ITG Workshop on Smart Antennas (WSA), 2012
- [14] Marsch, P. and Fettweis, G.; "Uplink CoMP under a Constrained Backhaul and Imperfect Channel Knowledge," IEEE Transactions on Wireless Communications, vol. 10, no. 6, pp. 1730–1742, Jun. 2011.
- [15] Grieger, M. and Marsch, P. and Fettweis, G.; "Large Scale Field Trial Results on Uplink CoMP with Multi Antenna Base Stations," IEEE Vehicular Technology Conference (VTC '11-Fall), San Francisco, USA, 2011.
- [16] Morelli, M. and Kuo, C.-C.J. and Pun, "M.-O. Synchronization Techniques for Orthogonal Frequency Division Multiple Access (OFDMA): A Tutorial Review," Proceedings of the IEEE, 95(7), 2007.
- [17] 3GPP. Physical Channels and Modulation. 2011. TS 36.211 v10.4.0.
- [18] A. H. Sayed. Adaptive Filters. J. Wiley & Sons, 2008.
- [19] Grieger, Michael and Fettweis, Gerhard.; "Impact of Antenna Downtilt on Cooperative Uplink Detection in a Large Scale Field Trial," IEEE Intern. Workshop on Multicell Cooperation in conjunction with IEEE GLOBECOM 2011, 2011.
- [20] ARTIST4G "D6.1 - First feedback on implementation aspects connected to the selected innovations," ARTIST4G technical deliverable, 2011
- [21] Mikael Sternad, Michael Grieger, Rikke Abildgaard Olesen, Tommy Svensson, Daniel Aronsson and Ana Belen Martinez, "Using "Predictor Antennas" for Long-Range Prediction of Fast Fading for Moving Relays," Workshop on 4G Mobile Radio Access Networks at IEEE WCNC '12, Paris, 2012

- [22] ARTIST4G, "D1.2 - Innovative advanced signal processing algorithms for interference avoidance," ARTIST4G technical deliverable, 2010
- [23] ARTIST4G, "D2.2 - Advanced receiver signal processing techniques: evaluation and characterization," ARTIST4G technical deliverable, 2011
- [24] Patrick Marsch, Michael Grieger, Gerhard Fettweis, "Large Scale Field Trial Results on Different Uplink Coordinated Multi-Point (CoMP) Concepts in an Urban Environment", IEEE WCNC' 11, Cancun, Mexico
- [25] M. Grieger, G. Fettweis, and P. Marsch, "Large Scale Field Trial Results on Time Domain Compression for Uplink Joint Detection," IEEE Personal Indoor Mobile Radio Communications (PIMRC '11 - WACC), Toronto, Canada
- [26] M. Grieger, P. Helbing, P. Marsch, and G. Fettweis, "Field Trial Evaluation of Compression Algorithms for Distributed Antenna Systems," Sarnoff Symposium (Sarnoff'11), 2011.
- [27] M. Grieger, V. Kotzsch, G. Fettweis, "Comparison of Intra and Inter Site Coordinated Joint Detection in a Cellular Field Trial," IEEE Personal Indoor Mobile Radio Communications (PIMRC '12), Sydney, Australia, 2012
- [28] H. Schoeneich, I. Berberana, M. Grieger, R. Visoz, "Interference Control in LTE-Advanced: An ARTIST4G Overview," Future Network Mobile Summit '12, Berlin, Germany, 2012
- [29] W. Zirwas, U. Zeeshan, M. Grieger, "Cooperative Feeder Links for Relay Enhanced Networks," European Wireless Conference (EW '12), Poznan, Poland, 2012
- [30] S. M. Alamouti, "A Simple Transmit Diversity Technique for Wireless Communications", IEEE Journal on Selected Areas in Communications, vol. 16, No.8, October 1998.
- [31] 3GPP. "Further advancements for E-UTRA physical layer aspects. TR 36.814 v9.0.0.", 2010
- [32] L. Glavieux, C. Laot, and J. Labat, "Turbo equalization over a frequency selective channel," in Proc. Int. Symp. Turbo Codes, pp. 96 – 102, Sep. 1997
- [33] X. Wang and H. Vincent Poor, "Iterative (Turbo)soft interference cancellation and decoding for coded CDMA," IEEE Trans. Commun., vol. 47, no. 7, pp. 1046 – 1061, Jul. 1999
- [34] M. Tüchler, R. Koetter, and A. Singer, "Turbo equalization: principles and new results," IEEE Trans. Commun., vol. 50, pp. 754 – 767, May 2002
- [35] C. Laot, R. Bidan, and D. Leroux, "Low-complexity MMSE turbo equalization: a possible solution to EDGE," IEEE Trans. on Wireless Commun., vol. 4, no. 3, pp. 965 – 974, May. 2005

## 5 Appendix

### 5.1 Testbed Information

**Table 11: Implementation plan of BS sites in Dresden LTE-Advanced testbed**

Parameter	Hauptbahnhof					
	HBf 0	HBf 60	HBf 120	HBf 180	HBf 240	HBf 300
Sector						
Longitude	13,73649 °	13,73656 °	13,73656 °	13,73656 °	13,73646 °	13,73646 °
Latitude	51,04202 °	51,04187 °	51,04187 °	51,04187 °	51,04196 °	51,04196 °
Altitude of bottom of building over sealevel	114 m	114 m	114 m	114 m	114 m	114 m
Altitude of middle of antenna over ground	54,5 m	54,5 m	54,5 m	54,5 m	54,5 m	54,5 m
Building height	53,0 m	49,6 m	49,6 m	49,6 m	49,6 m	49,6 m
Antenna height over roof top	1,5 m	4,9 m	4,9 m	4,9 m	4,9 m	4,9 m
Antenna altitude over antennas of Hbf Süd	19,0 m	19,0 m	19,0 m	19,0 m	19,0 m	19,0 m
Distance to roof edge:						
* main direction	0,7 m	3,0 m	3,0 m	3,0 m	9,0 m	9,0 m
* orientation of left/straight/right face	W / N / E	N / E / S	N / E / S	E / S / W	S / W / N	S / W / N
* orthog. to left edge	0,8	10,8 m	11,1 m	13,0 m	30,0 m	6,0 m
* orthog. to edge straight ahead	0,6	9,2 m	3,0 m	32,0 m	6,0 m	6,2 m
* orthog. to right edge	0,6	6,0 m	23,0 m	30,0 m	5,0 m	8,4 m
Shadow width on ground:						
* left edge	28 m	109 m	112 m	132 m	304 m	61 m
* edge straight ahead	21 m	93 m	30 m	324 m	61 m	63 m
* right edge	21 m	61 m	233 m	304 m	51 m	85 m
Antenna type	Kathr.41	Kathr.29	Kathr.41	Kathr.29	Kathr.41	Kathr.29
Antenna direction	0 °	60 °	120 °	180 °	240 °	300 °
Mechanical downtilt	5 °	5 °	5 °	5 °	5 °	5 °
Electrical downtilt range	12 °	10 °	12 °	10 °	12 °	10 °

Parameter	Lennéplatz			Fritz-Fö.-Pl.	Hauptbahnhof Süd		
	LEN 60	LEN 180	LEN 300		SUED 60	SUED 180	SUED 300
Sector	LEN 60	LEN 180	LEN 300	FFP 30	SUED 60	SUED 180	SUED 300
Longitude [°]	13,745	13,7447	13,7448	13,73113 °	-->	13,73118 °	<--
Latitude [°]	51,038	51,0379	51,03808	51,03104 °	-->	51,03667 °	<--
Altitude of bottom of building over sealevel [m]	114 m	114 m	114 m	129 m	117 m	117 m	117 m
Altitude of middle of antenna over ground [m]	50,1 m	50,1 m	50,1 m	55,0 m	32,5 m	32,5 m	32,5 m
Building height [m]	48,5 m	48,5 m	48,5 m	49,3 m	28,0 m	28,0 m	28,0 m
Antenna height over roof top [m]	1,6 m	1,6 m	1,6 m	6,0 m	4,5 m	4,5 m	4,5 m
Antenna altitude over antennas of Hbf Süd [m]	164,1 m	164,1 m	164,1 m	184,0 m	149,5 m	149,5 m	149,5 m
Distance to roof edge:							
* main direction [m]	1	1,25	1	30,0 m	11,0 m	39,0 m	3,0 m
* orientation of left/straight/right face	N / E / S	E / S / W	S / W / N	W / N / E	N / E / S	E / S / W	S / W / N
* orthog. to left edge [m]	0,95 m	17,4 m	27,6 m	6,8 m	74,0 m	7,0 m	39,0 m
* orthog. to edge straight ahead [m]	0,4 m	1,25 m m	0,95 m	29,5 m	7,0 m	39,0 m	2,5 m
* orthog. to right edge [m]	27,6 m	1,5	0,4 m	12,8 m	39,0 m	3,0 m	74,0 m
Shadow width on ground:							
* left edge [m]	28 m	527 m	836 m	56 m	460 m	44 m	243 m
* edge straight ahead [m]	12 m	37 m	28 m	560m / 240m	44 m	243 m	16 m
* right edge [m]	836 m	45 m	12,1 m	105 m	243 m	19 m	460 m
Antenna type	Kathr.41	Kathr.41	Kathr.29	Kathr.41	Kathr.29	Kathr.41	Kathr.41
Antenna direction	60	180	300	30 °	60 °	180 °	300 °
Mechanical downtilt	5 °	5 °	5 °	5 °	5 °	5 °	5 °
Electrical downtilt range	12 °	12 °	10 °	12 °	10 °	12 °	12 °

Parameter	Straßburger		Mitte (Pirnaischer Platz)			Karstadt
	STR 180	STR 300	MIT 60	MIT 180	MIT 300	KAR 180
Sector	STR 180	STR 300	MIT 60	MIT 180	MIT 300	KAR 180
Longitude	13,75309 °	<--	13,74678 °	13,74664 °	13,7466 °	13,73677 °
Latitude	51,04544 °	<--	51,04939 °	51,04928 °	51,04933 °	51,04621 °
Altitude of bottom of building over sealevel	113 m	113 m	113 m	113 m	113 m	114 m
Altitude of middle of antenna over ground	53 m	53 m	51,3 m	51,3 m	51,3 m	29,3 m
Building height	48,4 m	48,4 m	49,5 m	49,5 m	49,5 m	27,8 m
Antenna height over roof top	4,6 m	4,6 m	1,8 m	1,8 m	1,8 m	1,5 m
Antenna altitude over antennas of Hbf Süd	166 m	166 m	164,3 m	164,3 m	164,3 m	<b>0 m</b>
Distance to roof edge:						
* main direction	13 m	9 m	8 m	7,5 m	4 m	2,5 m
* orientation of left/straight/right face	N / E / S	S / W / N	N / E / S	E / S / W	S / W	ESE / S / W
* orthog. to left edge	13 m	20,9 m	18 m	6,5 m	10 m	18 m
* orthog. to edge straight ahead	11,5 m	8 m	5 m	7 m	4 m	2,5 m
* orthog. to right edge	20,9 m	13 m	19 m	8 m	28 m	1,2 m
Shadow width on ground:						
* left edge	136,7 m	219,9 m	495 m	178,75 m	275 m	333,6 m
* edge straight ahead	121 m	84,1 m	137,5 m	192,5 m	110 m	46,3 m
* right edge	219,9 m	136,7 m	522,5 m	220 m	770 m	22,24 m
Antenna type	Kathr.41	Kathr.41	Kathr.41	Kathr.41	Kathr.41	Kathr.29
Antenna direction	160 °	310 °	60 °	180 °	300 °	180 °
Mechanical downtilt	0 °	0 °	5 °	5 °	5 °	5 °
Electrical downtilt range	12 °	12 °	12 °	12 °	12 °	10 °

## 6 Abbreviation

ADC	Analogue to Digital Converter
ARQ	Automatic Repeat Request
ASIC	Application Specific Integrated Circuit
AWGN	Additive White Gaussian Noise
BER	Bit Error Rate
BLER	Block Error Rate
BS	Base Station
CFO	Carrier Frequency Offset
CoMP	Coordinated Multi Point
CPU	Central Processing Unit
CRC	Cyclic Redundancy Check
CSI	Channel State Information
DAC	Digital to Analogue Converter
DeNodeB	Donor LTE Base Station
DL	Downlink
D-SIC	Distributed Successive Interference Cancellation
DSP	Digital Signal Processor
eNodeB	LTE Base Station
FDD	Frequency Division Duplex
FFT	Fast Fourier Transform
FPGA	Field-Programmable Gate Array
GUI	Graphical User Interface
HARQ	Hybrid Automatic Repeat Request
iFFT	inverse Fast Fourier Transform
JD	Joint Detection
JT	Joint Transmission
L1 / L2	Layer 1 / Layer 2

LTE	Long Term Evolution
LVDS	Low-Voltage Differential Signaling
MAC	Media Access Control
MAC	Multiply ACcumulate
MCS	Modulation and Coding Scheme
MER	Modulation Error Rate
MIMO	Multiple Input Multiple Output
MISO	Multiple Input Single Output
NoC	Network On Chip
OFDM	Orthogonal Frequency Division Multiplexing
PER	Packet Error Rate
PRB	Physical Resource Block
QAM	Quadrature Amplitude Modulation
RAM	Random Access Memory
RISC	Reduced Instruction Set Computer
RN	Relay Node
RRH	Remote Radio Head
RSSI	Receive Signal Strength
Rx	Receiver
SIC	Successive Interference Cancellation
SINR	Signal-to-Interference-and-Noise Ratio
SME	Smart Memory Engine
SDRAM	Synchronous Dynamic Random Access Memory
SOC	System On Chip
SRAM	Static Random Access Memory
TB	Transport Block
TBS	Transport Block Size
TDD	Time Division Duplex
TTI	Transmit Time Interval

Tx	Transceiver
UE	LTE Terminal
UL	Uplink
VLIW	Very Long Instruction Word